

Department of Precision and Microsystems Engineering

Stiffness compensation for piezoelectric energy harvesting

Improving the efficiency at low-frequency vibrations

Erik van de Wetering

Report no : 2021.010
Coach : T.W.A. Blad
Supervisor : R.A.J. van Ostayen
Specialisation : MSD
Type of report : MSc Thesis
Date : 11 January 2021



STIFFNESS COMPENSATION FOR PIEZOELECTRIC ENERGY HARVESTING

IMPROVING THE EFFICIENCY AT LOW-FREQUENCY VIBRATIONS

STIFFNESS COMPENSATION FOR PIEZOELECTRIC ENERGY HARVESTING

IMPROVING THE EFFICIENCY AT LOW-FREQUENCY VIBRATIONS

MSc Thesis

In partial fulfillment of the requirements for the degree of
Master of Science in Mechanical Engineering.
To be defended on Tuesday January 26th, 2021 at 9:30

by

Erik VAN DE WETERING

Report number: 2021.010

Mentor: T.W.A. Blad

This thesis was approved by the following committee:

Dr. ir. R.A.J. van Ostayen	chairman MSD, PME, 3ME, TU Delft
Dr. A. Hunt	MNE, PME, 3ME, TU Delft
Ir. T.W.A. Blad	MSD, PME, 3ME, TU Delft
Dr. ir. H. Polinder	TEL, MTT, 3ME, TU Delft

Keywords: Vibration energy harvesting, stiffness compensation, static balancing,
zero stiffness, piezoelectricity

Printed by: Repro van de Kamp

Front & Back: E. van de Wetering

Copyright © 2021 by E. van de Wetering

This thesis is confidential and cannot be made public until February 1, 2022

An electronic version of this thesis is available at

<http://repository.tudelft.nl/>.

PREFACE

I have always been fascinated by mechanics and electronics. My interest into mechanics had steadily grown over time, resulting into the enrollment for mechanical engineering. However, I never really turned my back to electronics. Courses like mechatronics, the electronics minor and especially my bachelor's project on energy harvesting made it clear that both of these worlds can be intertwined and that you can combine the best of these two physical domains into one project. During my bachelor's project it became apparent that mechanical engineering meeting up with electronics can result in complex yet interesting problems. No wonder I had to do my master's thesis on a similar subject, this time on the problem that arises when efficient operation is required at low frequencies. Although much work is to be done before vibration energy harvesters will see practical implementation to whatever the world sees fit, I believe that continued effort to expand knowledge about mechanisms, transducers and electronics will ensure that vibration energy harvesters will do their part in creating a more sustainable world.

*Erik van de Wetering
Delft, January 2021*

CONTENTS

Preface	v
1 Introduction	1
1.1 Relevance of energy harvesters	2
1.2 The mechanics of an energy harvester	2
1.3 Low frequency energy harvesting	3
1.4 Piezoelectric energy harvesting	7
1.5 Problem statement	7
1.6 Thesis outline	9
2 Literature review	11
3 Design process	23
3.1 Concept generation	24
3.2 Endstops	30
3.3 Early designs	31
3.4 Design for final prototype	31
3.5 Final prototype	33
4 Model	35
4.1 Mechanics of a piezoelectric element	36
4.2 Modelling approach	36
4.3 Mode of operation	38
4.4 Beam equation	38
4.5 Modal analysis	40
4.6 Circuit equation	42
4.7 Mechanical damping	44
4.8 Negative stiffness	45
4.9 Endstops	46
4.10 Inclusion of force-displacement data	49
4.11 Complete form of equations of motion	52
5 Research paper 1	53
6 Research paper 2	63
7 Reflection, conclusions and recommendations	75
7.1 Project overview	76
7.2 Learning process	76
7.3 Unsuccessful attempts	77
7.4 Conclusions	78

7.5	On the performance decrease of the model	79
7.6	Recommendations	80
7.7	Future research recommendations	81
	Acknowledgements	83
	Appendices	84
A	Prototypes	87
A.1	Testing of static balancing through magnets	87
A.2	Balanced energy harvester mk.1	88
A.3	Balanced energy harvester mk.2	88
B	Miscellaneous measurements	91
B.1	Balanced harvester Mk.1	91
B.2	Measurements at fixed load and varied speed.	92
B.3	Further application of hysteresis mapping	93
C	Data of piezoelectric beam	95
D	Figure of merit	97
E	Comsol models of piezoelectric beam and endstop stiffness	101
E.1	Piezoelectric model	101
E.2	Endstop stiffness	103
F	References	105
	References	105

1

INTRODUCTION

The first chapter provides an introduction into low frequency vibration energy harvesting and the challenges to be found when an energy harvester is miniaturized at these conditions. The use of electromagnetic damping will be discussed and what problems this introduces. From the miniaturization problems involved, it will be deduced why energy harvesters utilising piezoelectric transduction may provide a good alternative, especially statically balanced piezos. The problem statement will be formed followed by an outline of the remainder of this thesis.

1.1. RELEVANCE OF ENERGY HARVESTERS

Before diving into various aspects of energy harvesters, their usefulness is to be discussed first. The transition to renewable energy sources on a large scale has received great attention and is widely known: think of wind turbines, solar panels, tidal energy and solar power towers. Another, less recognized class of energy input is through ambient vibrations. Here, the scale is totally different. Think for instance of a mechanical watch, scavenging energy from wrist motion.

In systems, processes often need to be monitored, through the use of all sorts of sensors. Think of TPMS (Tyre Pressure Monitoring System) sensors to monitor the tyre pressure in cars or systems to monitor the state of train railways [1]. Sensors may be used to predict fatigue of components, accurately predicting the required moment of their replacement. This provides a better alternative to periodical checks and maintenance, where components may be replaced prematurely, or too late. Medical applications are also present, as in pacemakers, where the state of the heart is monitored and corrected through electric pulses.

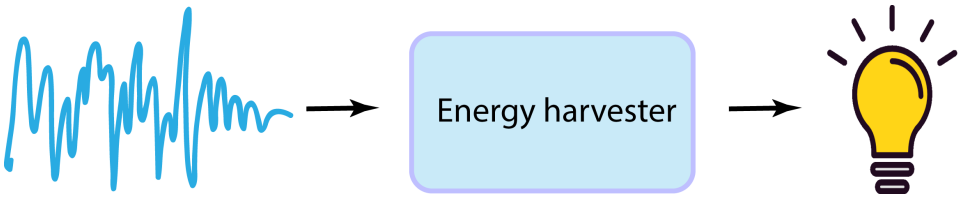


Figure 1.1: **The principle of vibration energy harvesting:** mechanical vibrations are fed into an energy harvester that transduces it into useful electric power.

All these applications have at least one thing in common: they need batteries in order to work. The lifetime of these may vary depending on how much power the sensor draws and how frequently it transmits data. Inevitably, those sensors need replacement when their batteries are depleted. As these sensors are often placed at locations that are hazardous or hard to reach (think of pacemakers), in combination with the cost of industrial-grade batteries to ensure reliability, it can become quite a costly operation to replace such a device. All of this gives rise to the need of an energy harvester being capable of scavenging energy from ambient vibrations found at its corresponding application. This principle is shown in figure 1.1. Power in mechanical vibrations is transduced to electrical power that can be used to power all sorts of small devices.

1.2. THE MECHANICS OF AN ENERGY HARVESTER

To discuss the challenges found in low frequency vibration energy harvesting, first the basic mechanics of a vibration energy harvester (VEH) are briefly discussed. A basic linear single degree of freedom (SDoF) VEH can be described by a mass-spring-damper system. A schematic diagram of such a system can be found in figure 1.2, which is valid for VEHs utilising electromagnetic transduction.

In this figure, the VEH body is denoted by the blue frame. In this frame, there is a proof mass M , affected by inertial forces, which is suspended by some spring or frame with

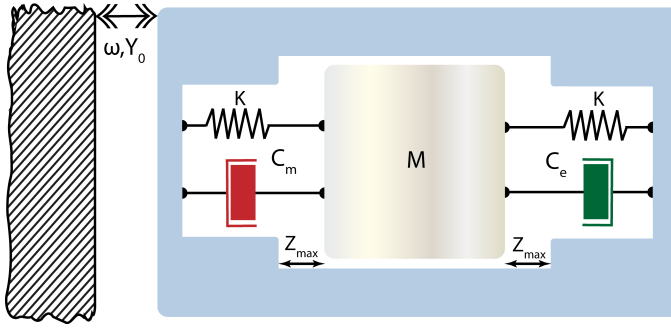


Figure 1.2: Schematic overview of a single degree-of-freedom energy harvester.

a stiffness K . There is an inherent mechanical viscous damping C_m and an electrical damping C_e , which is associated with the amount of energy loss to the electrical domain. When the VEH is excited sinusoidally at steady state, its input power is a function of the input displacement Y_0 and the radial frequency ω . The length L_z of the VEH is associated with the dimension along which the proof mass moves and Z_{max} is the maximum amplitude the proof mass can have before hitting the endstops. This parameter sets the displacement limit of the proof mass.

1.3. LOW FREQUENCY ENERGY HARVESTING

To make VEHs a viable alternative to electrochemical sources such as batteries, two main important things need to be presented. First, the size of the harvester is important. In the case of a pacemaker, its size will be one of the main determining parameters to decide whether it is implantable or not. Considering harvester size, its length L_z is even more important. Many VEHs are used as a resonator: the operational frequency is at or near its resonance frequency, resulting into the proof mass motion being an amplification of the input motion. This is beneficial for the output power, as a large proof mass motion can be achieved with little input motion. Depending on the level of damping (electrical, preferably), resonance may greatly amplify the input amplitude provided to the VEH. At large frequencies, this is usually not really a problem as input amplitudes tend to be really small. At low frequency however, the problem becomes very real. For a sinusoidal input motion, the displacement increases quadratically with a decreasing frequency while keeping the input acceleration constant:

$$|Y_0| = \frac{a}{\omega^2} \quad (1.1)$$

This means that if a VEH operating at low frequency is operated in resonant mode, the amplitude will either be very large or the proof mass hits the endstops if the motion is limited. In the first case the harvester is barely implementable as small devices are desired, in the latter case the efficiency is reduced through losses in the endstop collisions.

1.3.1. MOTION RATIO

To find out to what extent an energy harvester can be used as a resonator, the motion ratio λ can be used, which was introduced in [2]. This dimensionless parameter is defined as follows:

$$\lambda = \frac{L_z}{2Y_0} \quad (1.2)$$

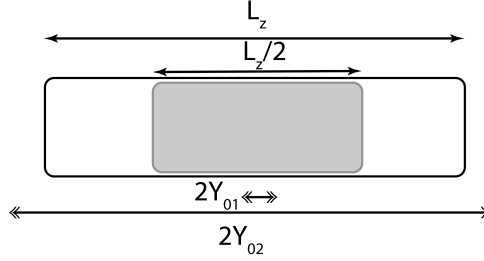


Figure 1.3: Schematic diagram of an optimal harvester configuration.

Figure 1.3 can quickly explain this parameter. Here, a harvester is shown with a grey proof mass of half the harvester length, which has been shown to be the optimal length when it comes to power generation [3]. It can be seen that $2Y_{01}$ is smaller than the internal displacement limit. Therefore, resonant amplification is possible by designing an appropriate Q -factor >1 . This Q -factor is the ratio between the maximum proof mass amplitude and the input motion Y_0 . One can easily identify that for the case of figure 1.3 a damping ratio $\zeta = 1/2Q$ equal to $1/\lambda$ results in a proof mass motion where the end-stop of the VEH is exactly hit. Furthermore, it can be seen that $2Y_{02}$ is larger than the length of the VEH. It must be noted that the required damping level necessary to prevent endstop hits will then quickly become large, i.e. the damping ratio approaches 1 or even surpasses 1. These large amounts of damping can hardly be provided through electrical damping due to poor scaling when coils are downsized [4]. The lower the motion ratio, the larger the damping needed to remain within the displacement limits. As such, resonant amplification at motion ratios just above 1 becomes very challenging and even impossible below 1, resulting in a nonresonant device.

1.3.2. EFFICIENCY AND FIGURE OF MERIT

Next to size, the efficiency is very important: a sufficient level of power needs to be extracted from ambient vibrations in order to power the appliance connected to it. The most straightforward way to define efficiency is by the ratio of output to input power:

$$\eta = \frac{P_{out}}{P_{in}} \quad (1.3)$$

Although this metric defines the fraction of energy that can be extracted from the environment, there is a catch. The required input power is depending on a lot of variables, which are partly geometrical and physical, but dynamic as well. A system at resonance requires less input power than one that just starts moving from rest. Furthermore, input

power is often not even measured, be it the case that it is even measurable. As a result, this metric loses practicality. In addition, there are way more specifications of interest that may be linked to efficiency performance. One may wonder at what conditions this performance was found. At what frequency had the VEH been excited? How large was the input acceleration? The efficiency doesn't tell. Another specification of interest is the size of the VEH. Large proof mass amplitudes correlate positively with larger power output [5]. Therefore, power density becomes of interest: it is desired to generate as much power from an as small as possible volume, maximizing power density. When taking these specification into account as well, it becomes possible to benchmark and more accurately compare different VEHs on their performance.

A metric that takes these findings into consideration is the generator figure of merit FoM_g . This metric was introduced by [2] and is a modified version of the volume figure of merit FoM_v by [3], [6]. It is defined as follows:

$$FoM_g = \frac{P_{avg}}{\frac{1}{16} Y_0 \rho_{pm} V L_z \omega^3} \quad (1.4)$$

Here P_{avg} , Y_0 , ρ_{pm} , V , L_z , ω are the average RMS output power, input amplitude, proof mass density, VEH volume, length and input radial frequency, respectively. The idea behind this metric is as follows. The peak power of an energy harvester is taken and is compared to a reference output power in the denominator. This reference output power corresponds to a hypothetical cubic energy harvester with equal volume, mass and length, under the exact same excitation conditions. As such, it can be estimated how close the performance of the VEH under scrutiny is to its corresponding theoretical maximum [3],[6]. In appendix D, it can be found how this metric can be derived.

Looking at eqn. 1.4, one can quickly identify how variables affect the overall performance. A small volume and length have a positive effect as power density increases. Enlarging the input amplitude lowers the efficiency, as more power is put into the system. From this, it can be seen that a VEH with small length may be most promising.

In the work of [2], it was made clear that VEHs found in literature can attain a decent FoM_g more easily at an increased motion ratio. When it comes to small devices and large input motions or low frequencies, FoM_g tends to be quite poor. Designing and manufacturing a small length VEH that performs efficiently at large input motions and low frequency conditions can therefore be said to be challenge.

1.3.3. TWO-OUT-OF-THREE

In the previous section, three notable keywords may be found: low frequency, small harvester length and efficiency. These keyword have an interesting relation to each other, as they pose a dilemma in designing an energy harvester composed of three of them. If one is to design a harvester that operates on low frequency and is efficient too, it is likely to have a large length. This is needed for the resonant amplification. Figure 1.4a shows an example of this in the form of a Duffing oscillator, a type that tends to be relatively long [7]. Next, when making a small-sized, efficient harvester it will not match with operation at low frequency as the natural frequency rises with miniaturization. An example of this is shown in figure 1.4b in the form of a 0.15 cm³ cantilever implementation [8].

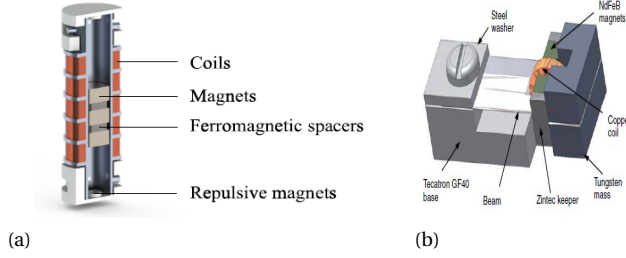


Figure 1.4: Examples of harvesters failing to meet all three criteria [7], [8].

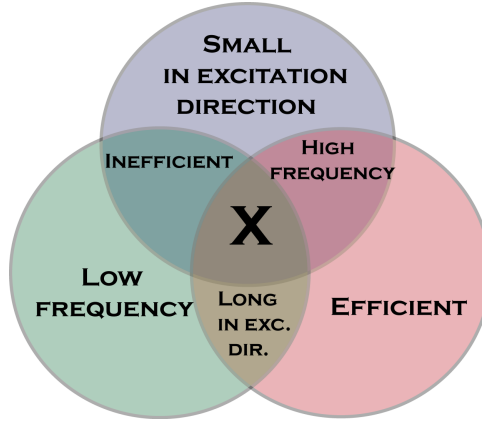


Figure 1.5: Venn diagram representation of the problem of low frequency energy harvesting. Combining two juxtaposed characteristics will result in the contrary of the characteristic that is left over. Combining all three is infeasible up till now.

Last, when designing a small-sized harvester at low input frequency, its efficiency will be presumably low. For this combination, it is hard to find a prototype in literature. Many works in literature tend to be the longest in the excitation direction and there is a good reason to do so. This can be explained by an analysis carried out in [6] and is closely related to figure 1.3. Assuming that the proof mass moves over the entire displacement limit, it has been shown that the maximum power that can be theoretically extracted over one cycle is equal to:

$$P_{max} = \frac{1}{2\pi} L_z M \omega^2 Y_0 \quad (1.5)$$

Writing the proof mass M as ρV , one can quickly identify that V also depends on a factor times L_z , resulting in a power that relates quadratically to L_z and linearly to the other dimensions. Therefore, it is way more beneficial to have an energy harvester that is long in the excitation direction than in other directions. However, it is not always desired to have the longest dimension in the excitation direction.

From these three examples it has become evident that low frequency, small length in the excitation direction and high efficiency do not coexist easily. This phenomenon

is schematically summarized in figure 1.5. It shows that when two characteristics are picked, it results in the opposite of the one that is left over. Producing a VEH that has all three of them is a challenge.

1.4. PIEZOELECTRIC ENERGY HARVESTING

Electromagnetic transduction has been most prevalent in the discussion until now. Coils and magnets leave a relatively large geometrical footprint in the excitation direction, making it hard to solve the problem introduced in figure 1.5. However, there are other transduction methods, such as piezoelectricity. In a piezoelectric material, an electric charge is built up after the material is deformed through an applied strain field. As a result of that, a potential difference is generated across the piezoelectric material. When the electrodes are connected and the circuit is closed, a current is able to flow, thus being able to generate electric output power. Figure 1.6 schematically shows how a bimorph piezoelectric beam is built up. The basis of the beam is formed by a substrate layer. On both sides, piezoceramic material is deposited, forming a bimorph configuration. The electrodes can be found on the top and bottom sides of the piezoceramic layers, in the same manner as in a capacitor. The blue arrows denote the polarization directions of the piezoceramic layers and indicate that they must be connected in series. As piezoelectric beams claim little space in the bending direction, they are good candidates for forming a VEH that is small in the excitation direction.

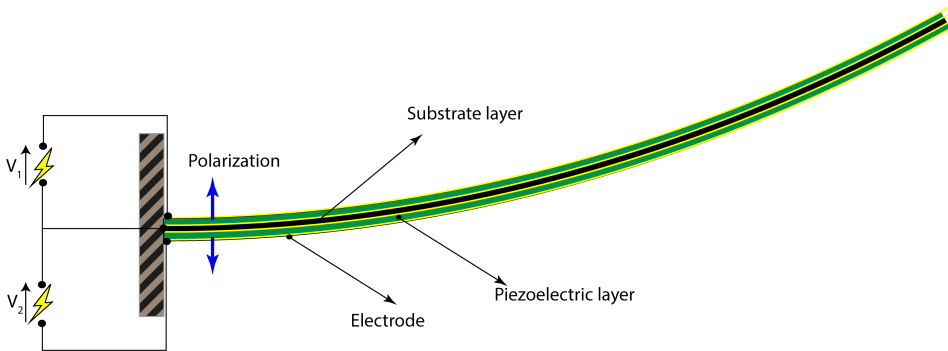


Figure 1.6: Schematic view of a piezoelectric cantilever generating a voltage across its layers.

1.5. PROBLEM STATEMENT

Piezoelectric beams are generally very stiff, resulting in high resonance frequencies. Figure 1.7a shows the interaction of the proof mass with the forces acting on it: the excitation force is distributed over an inertial, spring and damper force. At resonance, the inertial and spring forces cancel each other. The energy from the excitation now goes directly to the damper and therefore also to the output. The input motion is amplified by the Q -factor and therefore, a larger Q -factor relates to a larger proof mass amplitude and output power. In figure 1.7b, the frequency response of a piezoelectric beam is shown,

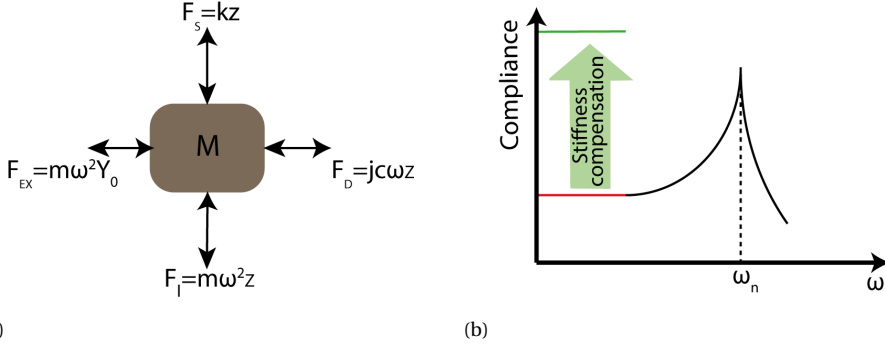


Figure 1.7: a) Forces interacting on a proof mass. b) Frequency response function showing resonance operation. Red line denotes the stiffness line.

confined to the first mode. In red, it shows the region at low frequency compared to the natural frequency, called the spring line. In this region the stiffness of the beam dominates the response; the stiffness prevents the piezo from being deformed by inertial forces at low frequencies. Therefore, the compliance is very low. Nevertheless, this problem of the stiffness forming an impediment to the compliance at low frequencies can be solved by artificially compensating that stiffness. This can be done by introducing elements that provide a negative stiffness, i.e. the force increases with displacement but now it acts in the direction of the displacement. By careful design of the negative stiffness, the applied force needed to deform the beam approaches zero. The system is now statically balanced or neutrally stable; the beam will not return to its undeformed configuration and its stored potential energy remains nearly the same over a certain range of motion.

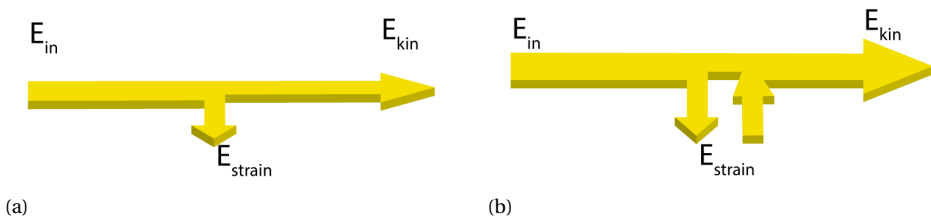


Figure 1.8: Schematic diagram showing the distribution of energy in a) normal positive stiffness system b) system with negative stiffness included.

The principle of operation for static balancing is schematically shown in figure 1.8. When no static balancing is applied, part of the energy that is applied to the system will be used for deforming the beam, leaving less energy that can be converted to kinetic energy of the beam motion. A large part of the input energy is lost to reversible strain energy, which is due to the large amount of stiffness in the piezo. When the stiffness of the piezo is

compensated by adding negative stiffness, the energy that is normally put into reversible strain, is now provided by the potential energy in the negative stiffness mechanism. As such, the energy input to the system should mainly go to the kinetic energy of the piezo. By bringing down the total amount of stiffness, large amplitude oscillations are made possible at a low frequency. This concept is shown in figure 1.7b by the green line. The compliance at the region normally demarcated as the stiffness line will now be much larger as will be its kinetic energy.

It is hypothesized that applying static balancing or stiffness compensation allows for relatively large amplitude oscillations at low frequency and should therefore provide a competitive figure of merit. As piezoelectric elements can be produced into a small scale, combination of this with the former hypothesis and excitation at low frequency may provide a solution to the problem discussed in section 1.3.3. It is not clear yet whether a real statically balanced state can be achieved in a piezoelectric beam, therefore, the term 'stiffness compensated' is preferred. The research objectives and questions are therefore:

Research objective: *Design, model and experimentally validate a stiffness compensated piezoelectric energy harvester for low-frequency, large-amplitude excitation.*

Research question: *How does a stiffness compensated piezoelectric beam behave?*

Research question: *To what extent can a stiffness compensated piezoelectric vibration energy harvester form a solution to the low efficiency at low motion ratios?*

1.6. THESIS OUTLINE

In this thesis, the main focus is on designing a piezoelectric energy harvester that is stiffness compensated and experimentally validated. The remainder of this thesis will go through this in several steps. The **second chapter** presents the literature review paper 'On the use of damping in low frequency vibration energy harvesting'. In this paper the damping performance of VEHs is discussed with a strong focus on electromagnetic transduction. An overview is presented that discusses various optimal load impedances for several motion input types such as harmonic or random excitation. Data from harmonically excited VEHs was analysed based on damping performance to assess what levels of damping are used in practice. An intuitive approach to selecting the suitable level of electrical damping was proposed, deviant from what is usually found in literature. The main conclusion was that damping ought to be used as a design parameter and not as a given optimality when designing a VEH including motion constraints. The findings in the paper have given rise to the research objective in this thesis. The **third chapter** focusses on the design process. Here, the problem is broken into subproblems and through a structural design methodology, the best concept is chosen and further analysed. In the **fourth chapter** the modelling approach is discussed and developed. A distributed parameter model based on modal analysis is used and further developed to model the dynamics and output voltage of the VEH. In the **fifth chapter** the first research paper is presented. Force-displacement measurements are carried out to assess the mechanical behaviour of the balanced piezo. This is done by using a custom force-

displacement setup. The **sixth chapter** presents the second research paper, which is about the performance of the energy harvester. Here, the focus lies on the performance of the model. The model is validated by experimental testing of the VEH on a linear air bearing stage. Furthermore, the performance is benchmarked in terms of the motion ratio and figure of merit. In the **seventh chapter** the results and entire process are discussed and conclusions are drawn. Also some recommendations for future research are mentioned. The **Appendices** present early prototypes, some miscellaneous force-displacement measurements, derivations of figures of merit, data of the piezo that was used and briefly discusses some FEM models.

2

LITERATURE REVIEW

In this literature review paper the use of damping in low frequency energy harvesting is investigated. Optimal electrical damping levels with respect to mechanical damping are investigated and a list of optimal load resistances for various types of input motions is compiled. Damping performance of works from literature has been analysed and it has been observed that in many cases, the electrical damping is matched to the mechanical damping. This is mainly due to this being a proven optimality in a specific case and through an intuitive method, the paper demonstrates that matched damping is only conditionally optimal and stresses that damping should be considered as a design parameter, not as a given optimality.

On the use of damping in low frequency vibration energy harvesting

E. van de Wetering and T.W.A. Blad

2

Abstract— In the tremendous collection of vibration energy harvesters found, it is often seen that only a few strategies for damping are adopted in designs, while applying different types of input excitations. In this research, an overview is presented to signify that different types of input motion also require different loads and therewith different damping levels. Works from literature operating on harmonic excitation are analysed based on their motion ratio and damping performance and an intuitive strategy to choose damping levels in a single degree of freedom energy harvester meeting dimensional constraints is presented. It is found that if the attainable electrical and mechanical damping levels are known, maximizing the former and minimizing the latter may provide a larger output power whilst maintaining the same amplitude. Therefore, damping may rather be considered as a design parameter as opposed to a given optimality when dimensional constraints have to be satisfied.

Keywords: Vibration energy harvesting, low-frequency, damping, optimal load

1. Introduction

Real-time monitoring of processes by use of wireless sensors is a promising way to efficiently predict and track the behaviour of systems [1]. A good example is the tyre pressure monitoring system (TPMS) in vehicles warning the driver when the tyre pressure has exceeded a lower threshold. The main drawback of the technology is the cost of replacing the sensor when the batteries are depleted. Industry demands high reliability batteries, which are more expensive. Furthermore, sensors are often located at locations hard to reach. This introduces high costs for replacing them.

A way to circumvent this problem is by using vibration energy harvesting extracting electrical energy from ubiquitous mechanical vibrations in the ambient. Much work has been done in this field already, mostly on resonator types [2] and human motion [3]. Also nonresonant devices have been developed such as frequency up-converters [4].

A metric to characterize to which extent the vibration energy harvester (VEH) is used as a resonator is the motion ratio $\lambda = \frac{L_z}{2Y_0}$ [5]. This metric describes the ratio between the VEH length dimension L_z along which the proof mass moves

and two times the input amplitude Y_0 , see Fig 1. A large motion ratio thus means that the VEH is a resonator and a motion ratio of e.g. smaller than one indicates that resonance cannot occur.

In their analysis, it is seen that most VEHs produced until now are in the motion ratio range of about 3 to 100. Maximum efficiency, defined as the generator figure of merit, tends to increase slightly with the motion ratio, whereas the normalized half-power bandwidth decreases. This is due the inverse relation between Q -factor and bandwidth [6]. Problems are then likely to arise since many real-life vibration sources tend to be rather random in nature instead of being narrowly centered around a certain frequency [7]. A high Q -factor resonator will then fail to effectively harvest power, as it needs to build up its amplitude over several cycles. When for instance a phase shift in the input occurs, the built up amplitude will be lost.

A few methods have been developed to get around this obstacle. Multimodal VEHs extract energy from multiple frequencies, effectively widening their bandwidth. Frequency upconverting has proven to greatly increase bandwidth performance [4]. Others have tried to develop a VEH with a tunable resonance frequency [8], yet this method rather fails to be united with the 'install and for-

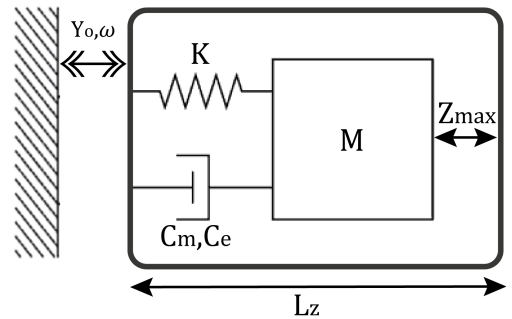


Fig. 1: Generic model of a single degree of freedom energy harvester. Y_0 , ω , K , C_m , C_e , M and L_z are the input amplitude, frequency, stiffness, mechanical and electrical damping, mass and length in excitation direction.

get' vision behind VEHs. The most fundamental method is tuning an intrinsic property of the VEH: the damping. The peak power and the bandwidth have an inverse relation which depends on the damping introduced into the system. By lowering the Q -factor the peak lowers and the response flattens, widening the bandwidth as a result.

That last solution, damping, is actually a grey area. Some authors state that it is best to match the electrical damping (ζ_e) to the mechanical damping (ζ_m) [2]. Others invoke the maximum power transfer theorem to obtain the best performance: here the load resistance is matched to the resistance of the transducer [9]. An excellent analysis on the performance limits was shown in [10], where regions for the desired damping level were determined as a function of input- and proof mass amplitude. In [11], it was found that in order to keep the proof mass within the constraints, the electrical damping had to be designed much larger than the mechanical damping. On the other hand, there might be cases where the electrical damping is desired to be lower, e.g. in a piezoelectric cantilever to allow more strain [12]. Thus it can be seen that a variety of work is already done considering damping optimality.

However, it is far from clear what optimal load or damping level is best suited in what type of harvester and their corresponding types of operation. This gives rise to the pitfall that designers take certain optimalities for granted, while it is actually not the most suitable for their design. When the operational frequency becomes low or input amplitude becomes large (low motion ratio), it is seen that the figure of merit efficiency is typically low [5], and poor design of damping or load could be a reason for this.

In this paper a classification is presented which provides an overview of what solutions to optimal performance are known from literature for different input motions, considering damping and load impedances. Providing such an overview is crucial to understand what assumptions are made to find a certain optimality or to find out what type of VEH operation an optimality actually belongs to. This suggests that in theory, for every type of input signal an optimal load could be found, and an optimal load could be found working best for all types of inputs within a certain application. Furthermore, VEHs found in literature are analysed and evaluated based on their motion ratios, damping and load characteristics, to find the general trends in their use.

In section ii, common methods to model the electromechanical coupling and its relation to

motion constraints are discussed. The limitations of these constraints give rise to a classification for optimal loads for different types of input motion. In section iii, it is shown what is done in practice in literature considering motion ratios and damping performance, of which the results are discussed in section iv. Conclusions are made in section v.

2. Method

A. Coupling methods

As pointed out in [13], three methods for the electromagnetic coupling can be distinguished. These are the uncoupled, velocity coupling and magnetic field interaction approach.

In the uncoupled case the dynamics on the mechanical and electrical domain are, as it suggests, uncoupled. A good example can be found in [9], where extensive work was spent on the nonlinear spring forces yet the coupling seemed to be subordinated. While the total damping (mechanical and electrical) was included in the equations of motion (EoM), it was assessed experimentally by a log decrement. Although convenient, this method forces the design process to become iterative. Furthermore, the effect of backward coupling from the electric circuit is absent in the EoM.

In the velocity coupling method, the mechanical and electrical domains are coupled through a force proportional to the relative proof mass velocity [13]. The electrical damping coefficient can then be found as [14]:

$$C_E = \frac{(NBL)^2}{R_c + R_L} \quad (1)$$

Here N, B, L are the coil turns, average radial flux density at the coil and coil length, respectively. R_c and R_L are the coil and load resistances. This method has been used by various authors [2], [15], [16]. For simple cylindrical magnets, B can be found analytically [2]. However, care must be taken when the design of the proof mass becomes more intricate, e.g. when making a stack of poled magnets as in [11]. In this case the flux linkage derivative will be nonlinear and a function of proof mass displacement. The same goes if the coil is short compared to the proof mass length. The magnet may then move entirely out of the control volume of the coil, ending up with very low flux linkage. When the magnet then enters the control volume, a large flux derivative and thus a large damping force is to be expected. When the magnet then remains in the control volume, a much lower damping is found since the flux derivative is now way lower.

Magnetic field interaction coupling is mainly based on FEM evaluation, which is the resort when analytical methods fail to work. Analytical formulations exist to find the force between the proof mass and endstop magnet (Duffing oscillator), as well as to find the induced voltage by Faraday's law [17]. However, this only works for rather simple geometrical implementations and complex designs will require FEM evaluation.

When using the field-field interaction approach, the magnetic flux linkage to the coil is evaluated as function of the proof mass position. Consequently the instantaneous electromagnetic damping coefficient and force interaction can be found and linked to the EoM. A comprehensive treatment about this approach can be found in [18]. As [19] pointed out, care must be taken since results only converge asymptotically to the physically true value. This can introduce large errors when not taken care of.

B. Motion constraints

From a practical point of view, the coupling or damping in the VEH is inherently related to some motion constraint; there is likely to be an endstop to limit the motion of the proof mass. It is therefore sensible to consider the damping level with respect to the motion constraint. In [10], such an analysis was done and operating regions for harmonic motion were found in terms of Q_m , Q_e , Z_{max} and Y_o , which are the mechanical and electrical Q -factors, the proof mass displacement limit and the input amplitude, respectively. In [10], four regions of operation were found by making use of the combination of Q -factors $Q_T^{-1} = Q_e^{-1} + Q_m^{-1}$:

- $\frac{Z_{max}}{Y_o} < \min(Q_{T,achievable})$: Here harmonic motion is not possible since the proofmass hits the endstops and ζ_e should be maximized.
- $\frac{Z_{max}}{Y_o} = \frac{Q_m}{2}$: Here the proof mass exactly hits the endstops if $\zeta_e = \zeta_m$. Slightly increasing ζ_e ensures harmonic operation.
- $\frac{Z_{max}}{Y_o} > \frac{Q_m}{2}$: Now the proof mass moves within the bounds and $\zeta_e = \zeta_m$ should be applied.
- $Q_e > Q_m$: The electrical damping cannot be made larger than or equal to the mechanical. Then ζ_e should be maximized.

Although this method is quite transparent, it has some practical limitations as well. First, it is based on the assumption that the input motion is harmonic. This introduces a restriction to the validity of using it. Next to that, when the excitation frequency becomes low, the result becomes impractical. Since the amplitude inversely scales with the square of the frequency, it becomes large at low frequencies, i.e. larger than the input amplitude

to allow resonant operation [4]. This implies that either a large VEH is required, or that the proof mass hits the endstops and thus energy is lost. The former option is hard to reconcile with the goal of energy harvesting and the latter is less efficient, yet implementable. As the application is limited to harmonic excitation, the need arises for a scheme that assesses the optimal damping or load for a VEH while taking the type of input motion into account.

C. Classification

In this section a classification in the form of optimal loads is presented for various types of input signals. The demarcation criteria for distinguishing between input signal types are out of the scope of this paper; they are also partly dependent on the judgement of the designer. The optimality conditions found in literature will be presented per class and it will be mentioned when literature is falling short. It should be noted that the optimality conditions found are valid for the condition where the power is dissipated in a resistor. When the circuit becomes more intricate by e.g. adding a rectifier, the relation between the velocity and electromagnetic damping is guaranteed to become nonlinear [20]. While it is certainly not the most realistic case to directly dissipate in a resistor, it provides the most transparent way to understand the dynamics. Fig. 2 presents an overview of all optimal impedances that will follow.

1) **Linear dynamics**: First the optimal loads of electromagnetic (EM) and piezoelectric (PE) energy harvesters comprising linear dynamics will be discussed.

a) **EM-harmonic**: Harmonic input means that the input consists of a sine function, or a combination of sines. This type of input signal is most commonly found in the literature, for it is the most convenient in practical testing. Sinusoidal frequency sweeps can be applied easily, thus forming the most straightforward method to benchmark a VEH. However, in the real world this type of signal is not quite often represented, introducing a mismatch between benchmarking results and real world applicability [7]. As a consequence, the optimality conditions for harmonic excitation are the most studied in literature as well. The class can be dichotomized into the resonant and nonresonant state, respectively. In [21], [22], the optimal load has been derived for general operational frequencies. This was done by translating the mechanical dynamics to the electrical domain through a two-port transformation. The optimal load is a complex

impedance and is dependent on the frequency of operation, i.e. the load ought to be tuned when the frequency of operation changes:

$$R_L = R_c + \frac{\theta^2 c_m \omega^2}{(k - m\omega^2)^2 + c_m^2 \omega^2} \quad (2a)$$

$$\chi_L = -\frac{\theta^2 \omega (k - m\omega^2)}{(k - m\omega^2)^2 + c_m^2 \omega^2} - \omega L_c \quad (2b)$$

Here R_L , χ_L , R_c , θ , c_m , k , m , L_c are the load resistance and reactance, coil resistance, coupling coefficient, mechanical damping coefficient, stiffness, proof mass and the coil inductance, respectively. Filling in the resonance conditions in the results of (2), the optimal load conditions are found when the system operates at resonance:

$$R_L = R_c + \frac{\theta^2}{c_m} \quad (3a)$$

$$\chi_L = -\omega L_c \quad (3b)$$

The optimal load impedance simplifies to the coil resistance and the electrical equivalent of the mechanical damping. The imaginary part of the optimal load impedance simplifies to the effect of the coil inductance. When the coil inductance is negligible with respect to the real part, it can be omitted. This result agrees to the findings in [23].

Note that when proof mass magnet stacks are used, the magnetic flux linkage derivative may turn out to be more fluctuating. Consequently, the output voltage signal may have frequency content that is a multiple of the excitation frequency, which may render the inductance on par with the resistance. Then it may turn out that the inductance should not be neglected [13].

b) EM-white Gaussian noise: White Gaussian noise (WGN) excitation comes closer to vibrations encountered in the real world. Mostly, a certain frequency band is selected over which the power is evenly spread, making it band-limited WGN. Considering the optimality in WGN excitation, there is fewer literature to be found, although a few authors have published an optimal load condition. In [20], the general power efficiency¹ of a VEH has been derived. It has also been found that generally, the load to ensure maximum power efficiency deviates from the load to maximize output power, which is a common phenomenon in batteries [14], [24]. However, as the input power remains nearly constant for white noise excitation, a single load can be found in this case that satisfies both maximum power transfer and efficiency [25]. The optimal load can then be found in [20] as:

$$R_L = \sqrt{R_c^2 + R_c \frac{\theta^2}{c_m}} \quad (4)$$

c) EM-shock loading: When it comes to shock loading or combinations of shock and harmonic, it is seen that there's not much to find in literature considering optimality. If human motion is considered as shock motion (e.g. from heel strikes), practical implementations can be found, often in the form of a Duffing oscillator [3], [11], [26]. Interestingly, the load resistance in these papers has a wide spread when compared to their coil

¹Power efficiency here means $\frac{P_{out}}{P_{in}}$. While it must be noted that P_{in} cannot be known in a lot of cases, the expression for the load that maximizes this efficiency can actually be found through the ratio of electrical to total damping [20].

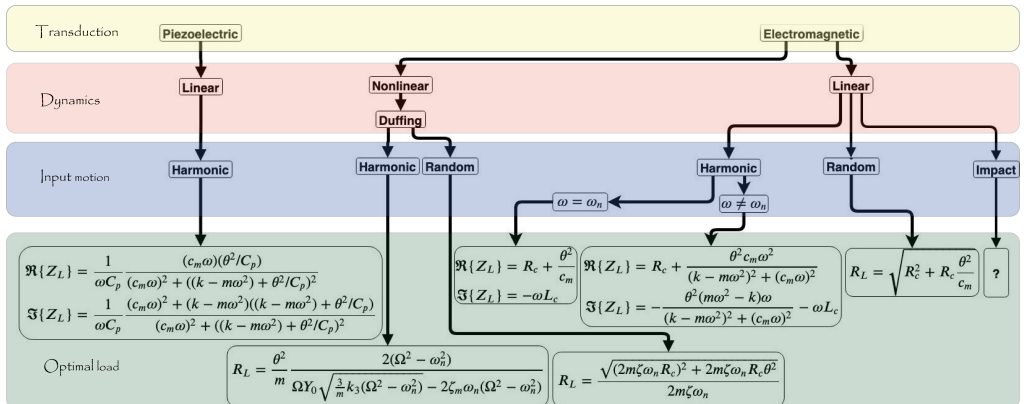


Fig. 2: Chart overview of the optimal resistance R_L and reactance χ_L for electromagnetic and piezoelectric VEHs for different types of input motions. The results are valid for linear circuits. Parameters m , c_m (ζ_m), k , k_3 , $\omega(\Omega)$, ω_n , C_p , θ , R_c , L_c denote mass, mechanical damping, stiffness, cubic stiffness, operational frequency, natural frequency, capacitance, coupling, coil resistance and coil inductance, respectively.

resistances. Nevertheless, the load resistance was experimentally confirmed to be the optimal in all cases.

To the author's best knowledge, there isn't really a guideline to be found which maps out the optimal damping or load resistance when it comes to shock load inputs. However, intuitively, optimalities may be found. If shock loads do somewhat intermittently appear, the total damping may be designed as such that there's a slow ringdown to the next shock load. This ensures that the proof mass continues oscillating as much as possible until the next impact. On the other hand, when shocks do appear frequently in a timespan, the damping can be maximized to extract as much energy as possible inbetween the shock loads.

d) **PE-harmonic**: Next to the electromagnetic transducer optimalities, the optimality for piezoelectric transduction is briefly investigated. The focus is on harmonic excitation. In [27], an extensive analysis is shown considering the optimal load for harmonically excited piezoelectric VEHs. The authors have also shown that the theoretical maximum power level can only be obtained when a certain level of electromechanical coupling is maintained. From [27], the following general load optimality can be found:

$$R_L = \frac{1}{\omega C_p} \frac{(c_m \omega)(\theta^2 / C_p)}{(c_m \omega)^2 + ((k - m\omega^2) + \theta^2 / C_p)^2} \quad (5a)$$

$$\chi_L = \frac{1}{\omega C_p} \frac{(c_m \omega)^2 + (k - m\omega^2)((k - m\omega^2) + \theta^2 / C_p)}{(c_m \omega)^2 + ((k - m\omega^2) + \theta^2 / C_p)^2} \quad (5b)$$

In (5), C_p and c_m are the capacitance and mechanical damping, respectively.

2) **Nonlinear dynamics**: Next to the VEHs including linear dynamics, nonlinear dynamics can be exploited as well and these cases require different types of optimal loads. Two cases will be discussed for electromagnetic VEHs in the form of Duffing oscillators.

a) **Nonlinear EM-harmonic**: When stiffening nonlinearities (Duffing) are included in the dynamics, the optimality becomes more complicated for harmonic input. In a linear system, the (electrical) damping only influences the Q -factor, and if the damping ratio becomes large it will influence the resonance frequency as well. However, in a nonlinear system the damping has a much stronger influence on the resonance frequency, better known as the jump down frequency. A low damping ratio will bend the frequency response and displace the jump down frequency [28].

In [29], the optimum resistive load for a monostable stiffening VEH is derived. Here, the load adjusts the frequency response as such that the jump down frequency coincides with the operational frequency while maximizing the power transfer. This can be interpreted as first having the undamped response, upon which an excitation frequency is selected. Then the jump down frequency is shifted downwards over the backbone curve to match that excitation frequency, whilst transferring the maximum power to the load. The load to accomplish this is given as:

$$R_L = \frac{\theta^2}{m \Omega Y_o \sqrt{\frac{3}{m} k_3 (\Omega^2 - \omega_n^2) - 2\zeta_m \omega_n (\Omega^2 - \omega_n^2)}} \quad (6)$$

In (6), Ω , ω_n and k_3 are the excitation frequency, natural frequency and cubic stiffness, respectively. In deriving this optimal load, a few assumptions have been made in [29]. The resistance and inductance of the coil were considered to be negligible compared to the load resistance. However, inclusion of the coil resistance can be realized by some scaling. Furthermore, it is assumed that the losses in the mechanical and electrical parts are equal.

b) **Nonlinear EM-random**: Next to harmonic inputs to Duffing oscillators, they are also often subjected to random excitation. In [30], the optimal load resistance for a VEH subjected to broadband white noise was derived and experimentally verified:

$$R_L = \frac{\sqrt{(2m\zeta_m \omega_n R_c)^2 + 2m\zeta_m R_c \theta^2}}{2m\zeta_m \omega_n} \quad (7)$$

3. Results

After having found the optimalities for various types of VEH operation, an analysis is done to assess what is actually done in practice in the literature. This includes information about the motion ratios, damping levels and resistances. As the motion ratio is of major concern, the results are based on data from harmonically excited VEHs; the motion ratio is not defined for VEHs loaded with shock or random excitations. Fig. 3 presents the ratios of the damping to the resistances to find the relation between those parameters. Fig. 4 shows the total damping in VEHs as function of λ . The datapoints have been classified into frequency up converter (FupC, low frequency impulses exciting a high frequency oscillator), gradual endstop (stiffening, Duffing), hardstop and no stop. Fig. 5 elaborates on the damping and shows the ratio between the electrical and mechanical

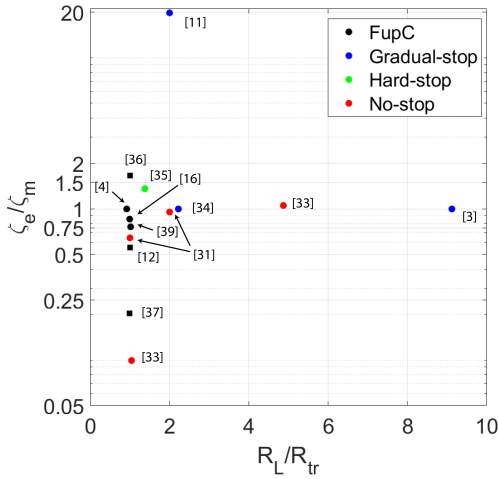


Fig. 3: Ratio of electrical damping ζ_e to mechanical damping ζ_m as function of ratio of load R_L to transducer resistance R_{tr} . Dots denote electromechanical transduction, squares piezoelectric.

damping as function of λ . In all these figures, dots are used for electromagnetic harvesters and squares for the piezoelectric ones. Note that some of the data points belong to the same VEH, yet under different testing conditions.

4. Discussion

A. Discussion of coupling

Considering the modelling of electromechanical coupling in electromagnetic VEHs, it is often seen that the transduction is assumed to be linear viscous, whereas this is not always physically correct (e.g. when using a poled magnet stack). In practice however, it may turn out that merging the coupling in to a single constant, may capture the dynamics quite well as the dynamics may average out. An example of this can be found in [31], where the flux linkage derivative is sinusoidal over the motion range, and the RMS value is taken as coupling coefficient. That means that an exponentially decaying impulse response may be found, implying that linear viscous damping is present, whereas the physics behind the electrical damping are actually more involved.

The displacement dependence of the coupling also has a consequence for the optimal load, as these often depend on the coupling coefficients. Here, however, it will be rather a necessity to capture the coupling into a single, average number. If the coupling were captured into a function of displacement, then the optimal load would also be a function of (proof mass) displacement, which

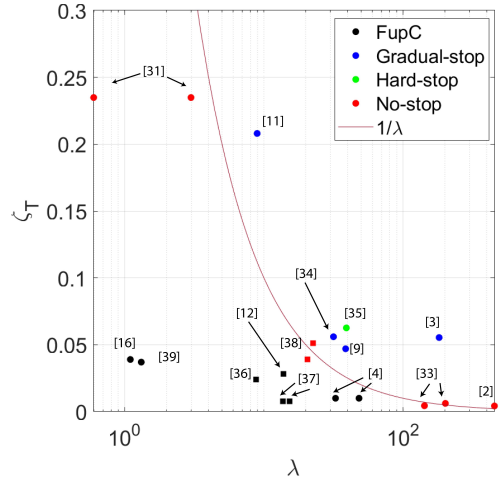


Fig. 4: Total damping ζ_T in the VEH as function of motion ratio λ . Dots denote electromagnetic transduction, squares piezoelectric. The $1/\lambda$ curve denotes the optimal total damping to prevent hitting endstops, idealized as in taking the proof mass volume to half of the volume of the VEH.

renders the optimization impracticable.

B. Discussion of analysed data

In Fig. 3 the ratios of damping to resistance are shown. Here, a noticeable trend is to be seen: either matched damping or resistance matching is used, with a few points deviating from this. Furthermore, it is seen that mostly FupC harvesters and VEHs without endstops are found at the resistance matching line, whereas the latter are also found on the matched damping line together with some Duffing oscillators. In [32], the relation between load resistance and electrical damping has been investigated. It has been found experimentally that when the electrical damping is low compared to the mechanical damping, the optimum load matched the coil load. When the electrical damping becomes on par with the mechanical, the load resistance becomes larger than the coil resistance. These results are consistent with what is shown in Fig. 3 and also in line with equation 3a. It is remarkable though, that the data points make a sudden sharp turn to the right; one would perhaps expect a more gradual path to the right.

From Figs. 4,5 it can be deduced that most VEHs can be found in the higher regime of $\lambda > 10$. This is consistent with the findings in [5], where it has been shown as well that when λ does get low, its figure of merit is typically low as well. Various reasons may be found to explain this. First, lots of research is done into resonant VEHs,

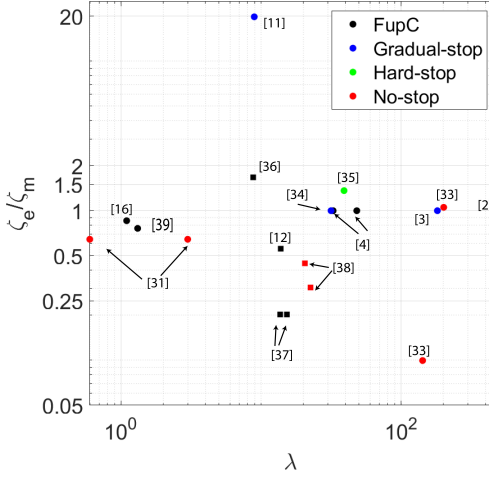


Fig. 5: Ratio of electrical damping ζ_e to mechanical damping ζ_m as function of motion ratio λ . Dots denote electromechanical transduction, squares piezoelectric.

which, when at a high frequency automatically results into a higher λ . Second, the input amplitude Y_0 on which λ depends, mostly depends on the input excitation frequency. To practically obtain a low λ , a low excitation frequency can be used, which is typically hard to achieve with standard shaker setups. To excitate a VEH at low frequency and large amplitude, using a linear stage would be most convenient, yet in most literature a setup like this is not seen. Last, the VEH length L_z influences λ and thus it comes down to scaling. Electromagnetic transducers usually scale down poorly when it comes to miniaturization and thus influences the performance in a detrimental manner [33].

Considering single degree of freedom (SDoF) harvesters it can be seen from Fig. 4 that in the low-end range of λ the total damping is quite higher compared to the rest of the data points. This is expected as the lower allowable proof mass amplitude requires larger amounts of damping. Most VEHs without endstops use low levels of damping; a large output can either be achieved through large flux linkage or large velocity and here the latter option is chosen. Duffing oscillators tend to use a higher damping. In Fig. 5 the results show some difference compared to Fig. 4. First, in the low range of λ it can be seen that for the high total damping cases, the ratios of the damping parameters differ a lot due to different levels of ζ_m . Duffing oscillators tend to have a ratio of at least one, which is likely due to their larger size and therefore larger coupling. On the other hand, piezos tend to use a lower amount

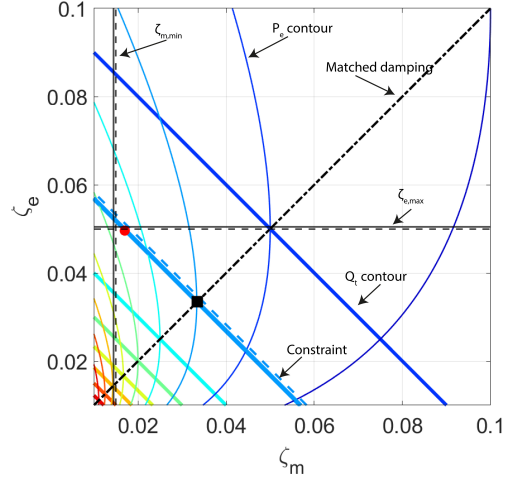


Fig. 6: Contour plot of total Q -factor Q_t as function of ζ_m and ζ_e superimposed on a contour plot of the normalized electrical power $P_e \sim \zeta_e/(\zeta_e + \zeta_m)^2$. Contours have been normalized between zero and one, so the more to red, the closer to one. Dashed lines demarcate the feasible region of the proof mass motion and attainable damping values. The dash-dotted line denotes the damping matching criterion.

of electrical damping, which may ensure larger amplitudes and with that more strain and output. Nevertheless, due to the shortage of data points, these statements cannot really be generalized; more data will be necessary to draw sharp conclusions on this.

Fig. 4 also includes the $1/\lambda$ curve, which would be the ideal total damping for a SDof harvester with a proof mass length of half the harvester length and negligible endstop volume (see section C of discussion). Interestingly, it is seen that near $\lambda = 10$ and lower the total achieved damping is not to be found above that curve anymore. This may indicate that the achievable level of damping may reach its limit near this region. However, to find the location more accurately, more data points will be necessary. Next to that, it is only valid for SDof harvesters; it doesn't count for FupC types.

FupC harvester types denote interesting damping characteristics. The total damping is mostly seen to be quite low in Fig. 4. On the other hand, the electrical damping seems mostly to be matched to the mechanical in Fig. 5. This may be a proper solution to FupC harvesters as one would like to have the high frequency oscillator (HFO) to oscillate as long as possible between subsequent impulses, which implies that low damping must be used. Next to that, as the space claimed by the HFO is usually small, a sufficient amount of total

damping will be required, which in case of a coil transducer is unlikely to be delivered electrically. Therefore matching the damping in this case may be a good solution. The same line of reasoning may be applied to MEMS resonating harvesters.

C. Damping as a design variable

It is often seen that the damping is matched in designing a harmonically excited VEH, as can be seen in Fig. 5. If the VEH has no displacement limit, then differentiating the output power as in [33] with respect to ζ_e will indeed yield the maximum power. However, this is mostly unrealistic. Consider a VEH of length L_z , proof mass length of $\frac{L_z}{2}$ and negligible spring geometry, which is considered as the ideal distribution in a VEH to gain maximum output power [6]. The maximum total Q -factor allowing harmonic motion can then be found as $Q_{T,max} = \frac{L_z}{4Y_o}$. This implies that $\zeta_{T,min} = \frac{1}{\lambda}$. If $Z_{max} = Q_{T,max}Y_o \approx \frac{Q_m}{2}$ then the matching conditions are indeed optimal, provided that Q_m is invariable. In practice however, L_z is likely to be fixed through design specifications, as well as Z_{max} . As long as Q_m is variable, it will be better then to maximize Q_m while minimizing Q_e , as long as $Q_{T,max}Y_o < Z_{max}$ is satisfied. This implies that the designer should be aware of the attainable mechanical and electrical damping levels.

In most cases, the mechanical damping is not fixed and can be reduced to a minimum. Then while reducing the mechanical damping, the electrical damping could be increased to retain the same amount of total damping. In this way, a set of damping levels can be found which yields the same Q -factor and total amount of dissipated energy.

This concept is demonstrated in Fig. 6: the contour plot of the combined Q -factor Q_t is shown and is superimposed on a contour plot of the normalized electrical power at resonance, which scales by $\zeta_e/(\zeta_e + \zeta_m)^2$ [33]. Given is a minimum mechanical and maximum electrical damping achievable and a maximum Q -factor as constraint denoted by the dashed lines. The dashed lines indicate the direction to the feasible region. Then several combinations of damping can be used to achieve that Q -factor: matched damping (black square) or maximized electrical damping (red dot). In both cases the total damping is constant, yet in the red dot case more power is dissipated to the electrical domain as seen from the power contours. On the other hand, when ζ_m is fixed and no constraint on the Q -factor is imposed, it is indeed seen that when matched damping is applied, the output power is maximized. This is often the approach taken in literature. From Fig. 6 it can thus be seen that if the maximum allowable Q_T is known, damping values can really

be considered as design variables.

D. Limitations of study

The classification of optimal loads may be thought of to be incomplete; for instance in the nonlinear dynamics category the FupC and bistable VEHs are missing. The same goes for the piezo part. However, the main goal of making an overview is to provide clarity to something indistinct. Hereto, the cases that had no clear optimality available in literature or that were too specific, were omitted from the classification to keep it clear. The main purpose is to provide the insight that damping levels are design parameters and are not necessarily to be taken for granted.

It must be noted that it is likely that many works found in literature had their primary focus on other aspects of the VEH (e.g. the stiffness or potential well), instead of optimizing the damping. It may therefore be debatable how representative certain data points are with respect to their harvester class.

Next to that, there's another uncertainty in the data. Literature is quite scarce on documenting the damping parameters. As a consequence, to ensure having a dataset large enough to generate some meaningful figures, some damping parameters had to be constructed from other data. This includes finding the damping ratio from the dimensional damping coefficient or from the Q -factor. For VEHs without an endstop, L_z had to be estimated by using the Q -factor and the proof mass size. No matter how carefully these data are reconstructed, it will introduce some uncertainty in the data points.

Lastly, it must be noted that some of the data points also belong to the same VEH, but under different testing conditions.

E. Recommendations

Finding a sufficiently large set of damping data from VEHs is not easy; many papers do not specify their used damping values, while these can provide a significant amount of information. Therefore, in order to get a more clear view on VEH damping performance in literature, it is recommended to specify the used damping levels. In most cases, the dimensionless damping ratios ζ_m and ζ_e can be easily determined through an experimental impulse response. The output voltage can be measured and a log decrement will yield the damping ratio. Under open circuit conditions, ζ_m can be determined, closed circuit conditions provides the largest ζ_e achievable and under optimal load, ζ_e under operational conditions can be found. Along with those damping values, it is very valuable to report excitation conditions and parameters needed to find FoM_g from [5]. In this way, relations

between damping, motion ratio and efficiency may be found. The current data set is suggesting, yet too incomplete to find patterns relating those variables. When more complete, design flowcharts may be generated to enable accelerated VEh design for proposed input signals.

2

F. Future research

It is seen from the Figs. 4,5 that the low range of λ is somewhat unrepresented; most harvesters are designed as resonators. It therefore seems that there is still a challenge where the input motion is large and the harvester length is small. As a small L_z has a better influence to efficiency than Y_0 at low λ [5], using piezos may be promising to find VEh with a low motion ratio and high efficiency.

As seen from from Fig. 2, an optimality for shock loading is not yet found. This type of motion input may need some more attention in analysing the optimal damping level and may be tightly connected to VEh utilizing high levels of electrical damping.

5. Conclusion

Despite the large amount of work found in energy harvesting, the amount of work done in cases where the input motion is large and the energy harvester length is small is less represented. Most VEh built are of a resonator type. In this research, it is seen that when it comes to choosing a suitable level of damping, various levels of damping may be chosen to satisfy the motion constraint. In practice though, it is seen that mostly matched damping or matched resistance is chosen as the solution. This may indeed provide a good solution when the maximum allowable amplitude is very low and the maximum achievable electrical damping is weak. It is also feasible when the mechanical damping is fixed and no displacement constraint is imposed. However, it has been shown that if a certain maximum Q -factor has to be satisfied, the mechanical damping ratio may be minimized while maximizing the electrical damping ratio. In this way, the total damping remains the same, yet more power is dissipated to the electrical domain opposed to the matching criteria. It is also seen that the optimal load resistances actually depend on what type of motion input is used. It seems that this is not often taken into consideration in works found in literature; most optimalities used are valid for harmonic inputs, yet they are used in various types of excitation. As a result, it can be concluded that the damping levels should be considered as design variables, which is often overlooked by designers. The optimality should not be taken for granted;

it should be designed with respect to the motion ratio.

Contributions to paper

- Provided a comprehensive overview of damping strategies and optimal loads for different motion inputs.
- Analysed VEh in literature to find out what is actually done in practise considering damping performance.
- Provided an intuitive graph to clarify the way how many works in literature select damping levels and how it could be done differently from a design perspective, starting at fixed motion constraints.

REFERENCES

- [1] H. Alawad and S. Kaewunruen, "Wireless Sensor Networks: Toward Smarter Railway Stations," *Infrastructures*, vol. 3, no. 3, p. 24, Sep. 2018.
- [2] S. P. Beeby, R. N. Torah, M. J. Tudor, P. Glynne-Jones, T. O'Donnell, C. R. Saha, and S. Roy, "A micro electromagnetic generator for vibration energy harvesting," *J. Micromech. Microeng.*, vol. 17, no. 7, pp. 1257–1265, Jun. 2007.
- [3] C. R. Saha, T. O'Donnell, N. Wang, and P. McCloskey, "Electromagnetic generator for harvesting energy from human motion," *Sensors and Actuators A: Physical*, vol. 147, no. 1, pp. 248–253, Sep. 2008.
- [4] T. Galchev, H. Kim, and K. Najafi, "Micro Power Generator for Harvesting Low-Frequency and Nonperiodic Vibrations," *J. Microelectromechanical Syst.*, vol. 20, no. 4, pp. 852–866, Aug. 2011.
- [5] T. W. Blad and N. Tolou, "On the efficiency of energy harvesters: A classification of dynamics in miniaturized generators under low-frequency excitation," *Journal of Intelligent Material Systems and Structures*, vol. 30, no. 16, pp. 2436–2446, Sep. 2019.
- [6] W. Q. Liu, A. Badel, F. Formosa, and Y. P. Wu, "A new figure of merit for wideband vibration energy harvesters," *Smart Mater. Struct.*, vol. 24, no. 12, p. 125012, Oct. 2015.
- [7] R. Rantz and S. Roundy, "Characterization of Real-world Vibration Sources and Application to Nonlinear Vibration Energy Harvesters," *Energy Harvest. Syst.*, vol. 4, no. 2, pp. 67–76, Aug. 2019.
- [8] V. R. Challa, M. G. Prasad, Y. Shi, and F. T. Fisher, "A vibration energy harvesting device with bidirectional resonance frequency tunability," *Smart Mater. Struct.*, vol. 17, no. 1, p. 015035, Jan. 2008.
- [9] A. Nammari, L. Caskey, J. Negrete, and H. Bardaweel, "Fabrication and characterization of non-resonant magneto-mechanical low-frequency vibration energy harvester," *Mechanical Systems and Signal Processing*, vol. 102, pp. 298–311, Mar. 2018.
- [10] P. D. Mitcheson, E. K. Reilly, T. Toh, P. K. Wright, and E. M. Yeatman, "Performance limits of the three MEMS inertial energy generator transduction types," *J. Micromech. Microeng.*, vol. 17, no. 9, pp. S211–S216, Aug. 2007.
- [11] M. Geisler, S. Boisseau, M. Perez, P. Gasnier, J. Willemin, I. Ait-Ali, and S. Perraud, "Human-motion energy harvester for autonomous body area sensors," *Smart Mater. Struct.*, vol. 26, no. 3, p. 035028, 2017.
- [12] M. A. Halim and J. Y. Park, "Theoretical modeling and analysis of mechanical impact driven and frequency up-converted piezoelectric energy harvester for low-frequency and wide-bandwidth operation," *Sensors and Actuators A: Physical*, vol. 208, pp. 56–65, Feb. 2014.

- [13] C. M. Saravia, "On the electromechanical coupling in electromagnetic vibration energy harvesters," *Mechanical Systems and Signal Processing*, Jun. 2019.
- [14] R. Munnig Schmidt, G. Schitter, A. Rankers, and J. van Eijk, "The design of high performance mechatronics." Amsterdam: Delft University Press, 2014, pp. 402,446,447.
- [15] V. R. Challa, M. G. Prasad, and F. T. Fisher, "A coupled piezoelectric-electromagnetic energy harvesting technique for achieving increased power output through damping matching," *Smart Mater. Struct.*, vol. 18, no. 9, p. 095029, Aug. 2009.
- [16] M. A. Halim, H. Cho, and J. Y. Park, "Design and experiment of a human-limb driven, frequency up-converted electromagnetic energy harvester," *Energy Conversion and Management*, vol. 106, pp. 393–404, Dec. 2015.
- [17] G. Aldawood, H. T. Nguyen, and H. Bardaweel, "High power density spring-assisted nonlinear electromagnetic vibration energy harvester for low base-accelerations," *Applied Energy*, vol. 253, p. 113546, Nov. 2019.
- [18] C. M. Saravia, J. M. Ramírez, and C. D. Gatti, "A hybrid numerical-analytical approach for modeling levitation based vibration energy harvesters," *Sensors and Actuators A: Physical*, vol. 257, pp. 20–29, Apr. 2017.
- [19] A. G. Avila Bernal and L. E. Linares García, "The modelling of an electromagnetic energy harvesting architecture," *Applied Mathematical Modelling*, vol. 36, no. 10, pp. 4728–4741, Oct. 2012.
- [20] S. Zhu, W.-a. Shen, and Y.-I. Xu, "Linear electromagnetic devices for vibration damping and energy harvesting: Modeling and testing," *Engineering Structures*, vol. 34, pp. 198–212, Jan. 2012.
- [21] S. Cheng, N. Wang, and D. P. Arnold, "Modeling of magnetic vibrational energy harvesters using equivalent circuit representations," *J. Micromech. Microeng.*, vol. 17, no. 11, pp. 2328–2335, Oct. 2007.
- [22] A. Cammarano, S. G. Burrow, D. A. W. Barton, A. Carrella, and L. R. Clare, "Tuning a resonant energy harvester using a generalized electrical load," *Smart Mater. Struct.*, vol. 19, no. 5, p. 055003, Mar. 2010.
- [23] N. G. Stephen, "On energy harvesting from ambient vibration," *Journal of Sound and Vibration*, vol. 293, no. 1, pp. 409–425, May 2006.
- [24] N. Storey, "Electronics a systems approach." Harlow: Pearson, 2013, pp. 251–253.
- [25] Q. Cai and S. Zhu, "Unified strategy for overall impedance optimization in vibration-based electromagnetic energy harvesters," *International Journal of Mechanical Sciences*, vol. 165, p. 105198, Jan. 2020.
- [26] C. Li, S. Wu, P. C. K. Luk, M. Gu, and Z. Jiao, "Enhanced Bandwidth Nonlinear Resonance Electromagnetic Human Motion Energy Harvester Using Magnetic Springs and Ferrofluid," *IEEE/ASME Trans. Mechatron.*, vol. 24, no. 2, pp. 710–717, Apr. 2019.
- [27] Y. Liao and J. Liang, "Maximum power, optimal load, and impedance analysis of piezoelectric vibration energy harvesters," *Smart Mater. Struct.*, vol. 27, no. 7, p. 075053, Jul. 2018.
- [28] M. F. Daqaq, R. Masana, A. Erturk, and D. Dane Quinn, "On the Role of Nonlinearities in Vibratory Energy Harvesting: A Critical Review and Discussion," *Appl. Mech. Rev.*, vol. 66, no. 4, Jul. 2014.
- [29] A. Cammarano, S. Neild, S. Burrow, D. Wagg, and D. Inman, "Optimum resistive loads for vibration-based electromagnetic energy harvesters with a stiffening nonlinearity," *Journal of Intelligent Material Systems and Structures*, vol. 25, no. 14, pp. 1757–1770, Sep. 2014.
- [30] P. L. Green, K. Worden, K. Atallah, and N. D. Sims, "The benefits of Duffing-type nonlinearities and electrical optimisation of a mono-stable energy harvester under white Gaussian excitations," *Journal of Sound and Vibration*, vol. 331, no. 20, pp. 4504–4517, Sep. 2012.
- [31] J. Smilek, Z. Hadas, J. Vetiska, and S. Beeby, "Rolling mass energy harvester for very low frequency of input vibrations," *Mechanical Systems and Signal Processing*, vol. 125, pp. 215–228, Jun. 2019.
- [32] F. M. Foong, C. Ket Thein, and A. R. Abdul Aziz, "Effect of Electromagnetic Damping on the Optimum Load Resistance of an Electromagnetic Vibration Energy Harvester," in *2018 2nd International Conference on Smart Grid and Smart Cities (ICSGSC)*, Aug. 2018, pp. 127–132.
- [33] T. O'Donnell, C. Saha, S. Beeby, and J. Tudor, "Scaling effects for electromagnetic vibrational power generators," *Microsyst Technol.*, vol. 13, no. 11, pp. 1637–1645, Jul. 2007.
- [34] D. F. Berdy, D. J. Valentino, and D. Peroulis, "Design and optimization of a magnetically sprung block magnet vibration energy harvester," *Sensors and Actuators A: Physical*, vol. 218, pp. 69–79, Oct. 2014.
- [35] K. Ashraf, M. H. M. Khir, J. O. Dennis, and Z. Baharudin, "A wideband, frequency up-converting bounded vibration energy harvester for a low-frequency environment," *Smart Mater. Struct.*, vol. 22, no. 2, p. 025018, Jan. 2013.
- [36] L. Gu and C. Livermore, "Impact-driven, frequency up-converting coupled vibration energy harvesting device for low frequency operation," *Smart Mater. Struct.*, vol. 20, no. 4, p. 045004, Mar. 2011.
- [37] T. Galchev, E. E. Aktakka, and K. Najafi, "A Piezoelectric Parametric Frequency Increased Generator for Harvesting Low-Frequency Vibrations," *J. Microelectromechanical Syst.*, vol. 21, no. 6, pp. 1311–1320, Dec. 2012.
- [38] H. Huang, C. Zheng, X. Ruan, J. Zeng, L. Zheng, W. Chen, and G. Li, "Elastic and Electric Damping Effects on Piezoelectric Cantilever Energy Harvesting," *Ferroelectrics*, vol. 459, no. 1, pp. 1–13, Jan. 2014.
- [39] M. A. Halim and J. Y. Park, "Modeling and experiment of a handy motion driven, frequency up-converting electromagnetic energy harvester using transverse impact by spherical ball," *Sensors and Actuators A: Physical*, vol. 229, pp. 50–58, Jun. 2015.

3

DESIGN PROCESS





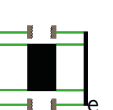
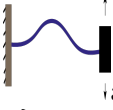
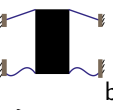
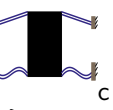
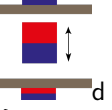
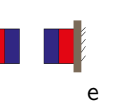
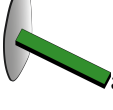
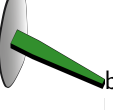
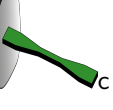
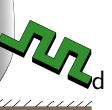

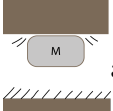
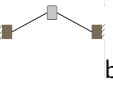

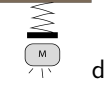
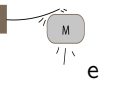
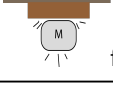

In the design process, the design requirements are formulated along with their subproblems. Subsolutions are found to these and through a structural design method, a suited prototype is found. Furthermore, finite element simulations are carried out to achieve an appropriate stiffness compensation of the piezoelectric beam.

3.1. CONCEPT GENERATION

To design a zero stiffness piezoelectric beam, many approaches can be found in order to find a suitable design. For instance, the negative stiffness that is induced can be realized in a multiple of ways, all having their advantages and disadvantages. In order to ensure that all subsolutions result into the best assembly, a systematic design procedure is used.

First, the features to be found in the harvester have to be assessed. These are as follows. A positive stiffness is to be found through the deformation of the piezoelectric beam. This stiffness is to be compensated by a negative stiffness, to bring their sum artificially to zero. The shape of the piezo is an important design parameter as well, as it has been shown that tapering a piezoelectric beam can greatly increase output performance through an improved strain distribution [9]. Furthermore, endstops need to be included to limit the deflection of the beam. These act as a strain limiter and protect the beam from strain overloading. This is important as the material is very brittle. Next to that, the endstops are also used to transfer momentum into the system. Table 3.1 shows an overview of the features to be found in the VEH with their corresponding solutions.

Table 3.1: Morphological chart comprising subcomponents featured in the design and their corresponding subsolutions. Green flexures denote piezoelectric elements, blue denote negative stiffness elements.

Features	Solutions				
1: Positive stiffness					
2: Negative stiffness					
3: Piezo					
4: Endstop					
					

3.1.1. ELIMINATION OF SUBSOLUTIONS

Some subsolutions are hard to implement in combination with other solutions or are simply infeasible. Therefore, these designs are removed before moving on to the compilation of designs. Subsolutions are eliminated due to lack of applicability, manufacturability issues or undesired interference with other solutions.

- 1d. Rotational folded suspension: this solution is suboptimal for rectilinear (SDoF) vibrations and favors rotational vibrations. Those are of less interest and also more difficult to test in practice.
- 2c. Double-tapered cantilever: although it may be superior in performance when it comes to S-shape deformation due to improved strain distribution, it becomes rather hard to manufacture when it comes to abrasive cutting of piezoelectric material.
- 3d. Meandering cantilever: may be efficient in terms of active area, but also hard to manufacture and to balance.
- 4c. Opposing magnet endstop: is likely to interfere with other (magnetic) subsolutions and may introduce undesired dynamics such as stiffening nonlinearity.
- 4g. Deformation-compliant endstop: while this solution is a good fit to limit strain in the cantilever, it is likely to underperform in transferring kinetic energy to the cantilever through impacts. Also, as the cantilever gradually makes contact with the endstop, friction due to sliding may occur, resulting into extra losses.

3.1.2. DESIGN CRITERIA

From the subsolutions that are left, many solutions can be assembled. However only one or a few designs will be used in the end for further analysis. To assess which design(s) will be most promising, assessment criteria need to be formulated to provide a solution to the issue posed in section 1.3.3:

1. The design should be as such that the length dimension in the excitation direction (L_z) is as small as possible in order to obtain a low motion ratio.
2. The total stiffness of the system should be as near as possible to zero.
3. The zero stiffness condition should be the most tunable. This allows for quick testing of the mechanics and reduces design iterations.
4. The design should be manufacturable. The implementation of the piezo should be viable, also in terms of output power.

3.1.3. MOST PROMISING CONCEPTS

From the full set of possible designs generated by combining all of the subsolutions left, six of them were selected on the account of being the most feasible. These are shown in figure 3.1. As can be seen, folded suspensions are excluded, as they are a bit over-complicated with respect to the problem. Therefore, the bistable fixed-guided stage is rendered obsolete as well, as these provide a pure rectilinear motion. Endstops are not yet included in the figure as these can be chosen more freely later on.

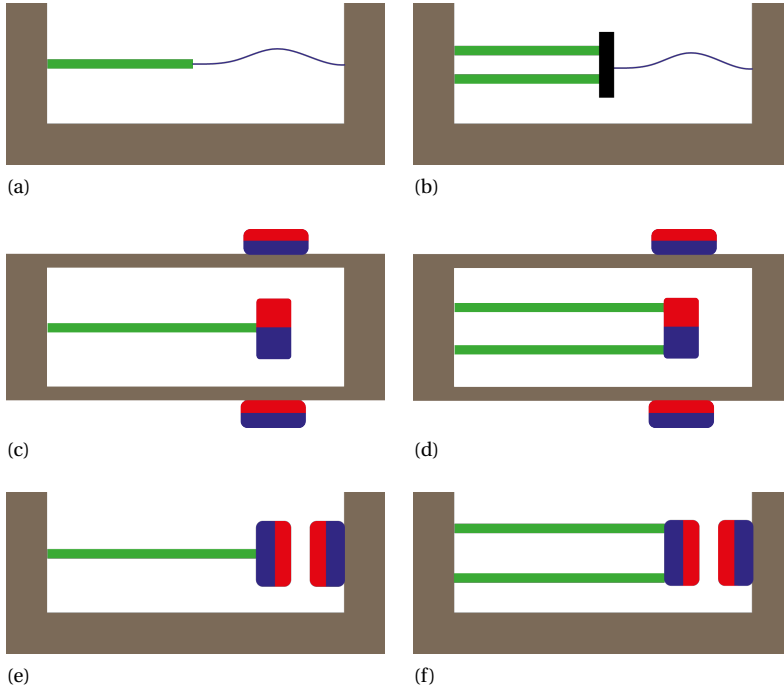


Figure 3.1: **Most promising concepts generated. Endstops have not been included into the figures.**

3.1.4. SENSITIVITY OF NEGATIVE STIFFNESS ELEMENTS

In the design criteria, it was mentioned that the amount of negative stiffness should be tunable. Various reasons can be found to see why this is important. First, the stiffness behaviour of the piezo is not entirely known in advance: a piezo is an electromechanical element, so the mechanical behaviour depends in part on the details of the electrical circuit to which it is connected. It is also known that the load resistance connected to a resonating piezo has an effect on the resonance frequency [10]. A larger load results into a higher resonance frequency, so an additional stiffness must be present due to that larger load. A piezo with a large electromechanical coupling is desired for the power output, so this effect can be of major influence. Furthermore, piezoelectric elements are known to display a rate dependent hysteresis in their relation between applied voltage and displacement [11]. For a transducer, it is likely that effects on the electrical domain could also be translated to the mechanical domain. Therefore it is likely that hysteresis will also have a strong effect in the force-displacement behaviour. As it is not exactly a priori known what effects this will cause, it is desirable to have a versatile stiffness characteristic. This means that the negative stiffness must be tuneable by altering a parameter such as a preload. Therefore, for the negative stiffness elements found in figure 3.1, a FEM simulation of negative stiffness behaviour is carried out to uncover the qualitative behaviour of these elements considering tunability.

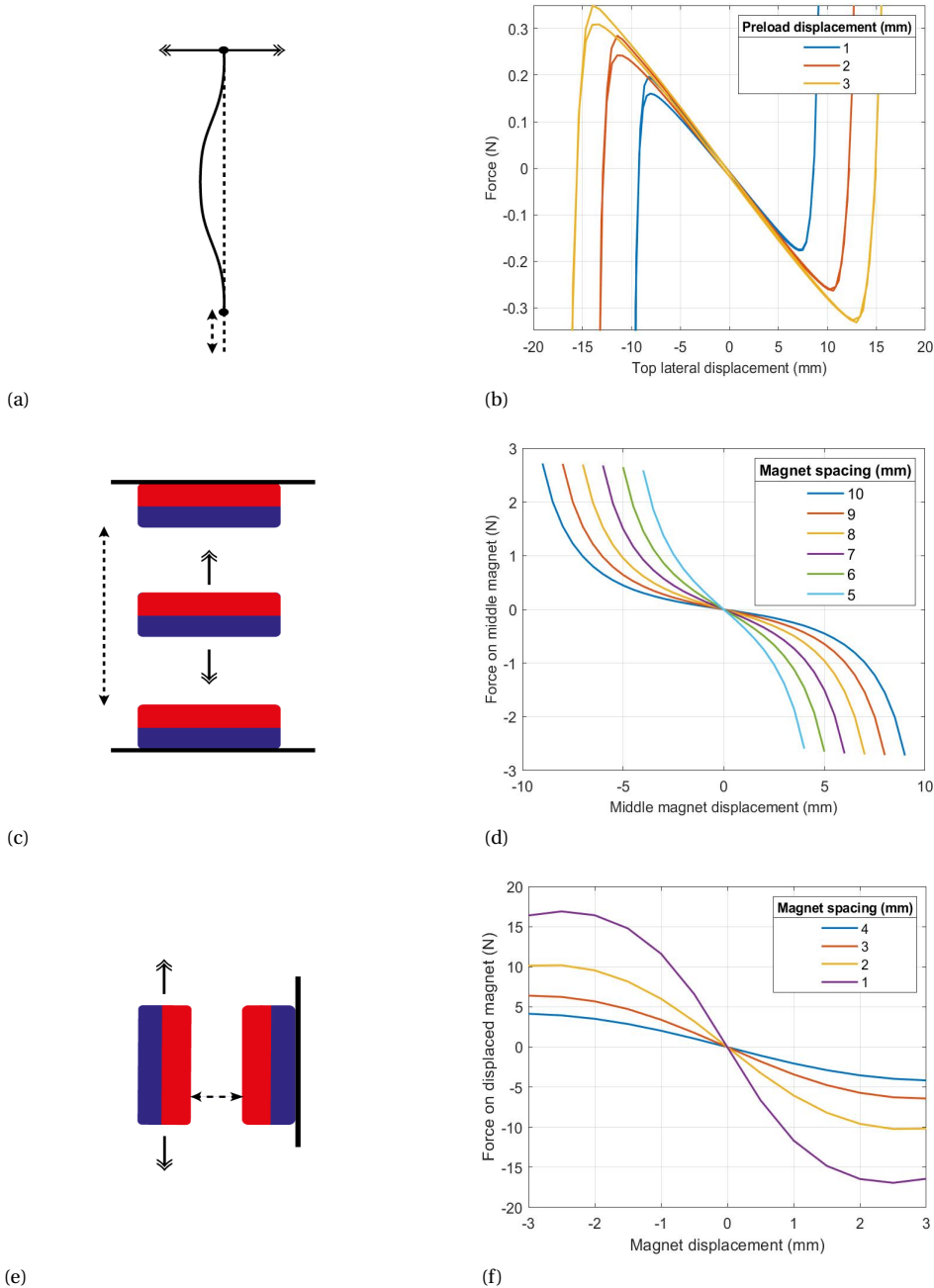


Figure 3.2: Sensitivity of negative stiffness elements to displacement tuning. (a),(b): buckled flexure, (c),(d): attracting magnets, (e), (f): repulsive magnets. Double arrows denote movement direction, dotted arrow the varied displacement parameter.

First, the buckled flexure's negative stiffness behaviour is analysed in ANSYS APDL. Here, a flexure of 50x5x0.1 mm is modelled, as can be seen in figure 3.2a. One side of the beam is fully constrained, except for the direction of the beam length, to provide for a preload displacement in this direction. The other end is also fully constrained except for the lateral displacement, this is to measure the force-displacement behaviour. The analysis is done for different preload displacements and its results can be seen in figure 3.2b.

Next to that, the configuration of attracting magnets is investigated. This case is modelled in COMSOL Multiphysics as it easily allows modelling of magnetic fields. Figure 3.2c shows the configuration that is modelled. It consists of three 1.22 T 10x1 mm disk magnets. The upper and lower magnets are fixed and a displacement sweep is applied to the middle magnet. The distance between the fixed magnets is variation parameter to investigate its influence on the stiffness. The results are shown in figure 3.2c.

Lastly, the configuration of repulsive magnets is modelled. The modelled configuration is shown in figure 3.2e. It consists of two 1.43 T rectangular magnets of 4.5x4.5x2 mm. In this case, the right magnet is fixed and a vertical displacement sweep is applied to the left magnet. The distance between them is the variation parameter. Figure 3.2f shows the results.

From the simulation results, the differences between the various negative stiffness methods become evident. A buckled flexure retains its stiffness whilst changing the preload. Adjusting the preload only results into a larger stroke and thus a larger potential barrier. Consequentially, a buckled flexure is unable to compensate for stiffness perturbations through preload tuning. It will require using a flexure with different geometry. The attracting magnet configuration shows quite a different behaviour. It becomes evident that varying the distance between the fixed magnets alters the negative stiffness as well. Moving the magnets closer together raises the stiffness and lowers the linear regime; the curves display a stiffness hardening. Last, the repelling configuration also shows alteration of the stiffness through varying the distance between the magnets. Here, the configuration rapidly stiffens if the magnets are getting close. However, opposed to the previous configuration, now stiffness softening is present.

3.1.5. ASSESSMENT OF BEST DESIGN

As the criteria, most promising concepts and their abilities are now known, their performance can be assessed by use of a morphological chart. First, for each of the criteria, scores need to be assigned for certain features that correspond to that criterion. These scores are between ± 2 . The scores are defined as follows:

1. Small length:

- **+2** Buckled flexure: a planar design may be realized, which takes little space in out of plane direction.
- **-1.5** Parallel guided stage: a second piezo beam for a parallel guided stage claims more space in excitation direction.
- **+1** Repelling magnet: this configuration allows for a collinear design, taking less space in the excitation direction.

- **+0.5** Attracting magnet: the magnets need to be placed in excitation direction, claiming more space.

2. Zero stiffness proximity:

- **+1** Buckled flexure: depending on implementation, the reaction moment of the buckling flexure may force the system to bistability.
- **+0.5** Parallel guided stage: no rotations of the piezo flexure and less parasitic movements that need to be compensated. May be beneficial in combination with buckling flexure of opposing magnet.
- **-1** Opposing magnet: due to opposing polarity, there is a torque on the magnet. This may result into a position bifurcation, forcing the cantilever into bistability.
- **+2** Attracting magnet: low magnetic torque exerted on magnet and it is a stable configuration.

3. Negative stiffness tunability

- **-1** Buckled flexure: only the motion range or energy barrier can be adjusted by preloading, stiffness can not be tuned.
- **+0.5** Parallel guided stage: may provide stability against bifurcation behaviour.
- **+1** Opposing magnet: stiffness can be tuned through adjusting distance between the magnets, yet the system may become rapidly unstable due to bifurcations.
- **+2** Attracting magnet: stiffness can be tuned through distance between magnets, and the attracting forces can be used to stabilize the system.

4. Manufacturability

- **+1** Buckled flexure: endstops are not mandatory as the flexure limits the motion range. Planar design out of a single metal sheet is possible.
- **-1** Parallel guided stage: this configuration will induce an s-shape or inflection point in the deflection pattern of the piezo. This results into charge cancellation which can be avoided, but complicates the design.
- **+1** Opposing magnet: easy to implement yet the placement of the magnets will demand great accuracy.
- **+1** Attracting magnet: also easy to implement, also sensitive to magnet placement but probably less problematic in this case.

This morphological chart to assess the best concept is shown in figure 3.3. The columns show the concepts and the rows the criteria. Each criterion can attain a score between ± 2 .

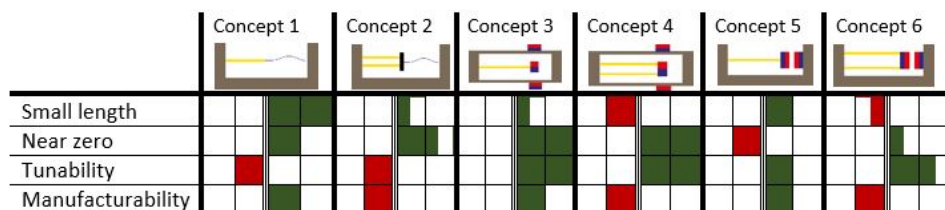


Figure 3.3: Morphological chart used to assess the best concept.

From the morphological chart it can be seen that Concept 3 has the best score, followed by Concept 1. Concept 3 performs best when it comes to approaching zero stiffness and tuning capabilities, although the length in the excitation direction may be a bit larger. Concept 1 on the other hand may perform very well when it comes to length in excitation direction. The extent to which it can approach zero stiffness is considered lower, as the buckled flexure induces a bending moment at the tip of the piezo, rendering it easily bistable. Concept 1 has no tuning capability as was demonstrated in figure 3.2b.

3.2. ENDSTOPS

One thing may be noticed in the design process up till now. Endstops were a subsolution included in the morphological chart in figure 3.1. However, they aren't included yet in the concept choice. The main reason for this is that almost every type of endstop could be combined with the designs so far, thus creating a very large set of possible designs. Therefore, a design is chosen based on the first three functional requirements and the choice of endstops comes afterwards. The best type of endstop can be deduced from a short line of reasoning.

- As already pointed out in section 3.1.1, opposing magnets (4c) are infeasible due to magnetic interference and deformation-conforming endstops (4g) are infeasible due to friction.
- No bistable mechanism is utilized in the chosen concept so (4b) is eliminated.
- Gradually stiffening endstops such as springs (4d,e) have to be designed with extreme care with respect to the force-displacement characteristics. The spring material should be non-magnetic and non-conductive to prevent eddy current losses. Considering these points renders these suboptimal.
- Hyperelastic endstop (4f): a rubber endstop is beneficial when it comes to protection from collision damage. However, losses in the material may also render it suboptimal as it may result into a very low coefficient of restitution.

This leaves only one solution behind, which is the hard stop (4a). What remains is to choose from what material the endstop is made. As mentioned before, the endstop must be non magnetic to prevent the magnetic proof mass from adhering to it. Furthermore, a non conductive material is more suitable to exclude the presence of eddy currents. These will provide an additional damping to the proof mass motion. Although it is an

effect that occurs at rather larger velocities, it is always preferred to exclude potentially detrimental effect when exploring something novel.

Considering the points just mentioned, a plastic may be a good solution as endstop implementation. As it is softer than a metal, it helps to prevent the impact from being so hard that it damages the piezo. A disadvantage of using plastics is that plastic deformation is more likely to occur, resulting into energy losses. However, as the proof mass is rectangular and the filleted edges makes contact with the endstop, the contact can be seen as a line contact. As a result, plastic deformation will require an amount of force that is unlikely to be encountered in this case.

3.3. EARLY DESIGNS

Before the manufacturing of the final prototype, a few early prototypes were made to investigate the behaviour of a statically balanced piezo. The designs of those prototypes and accompanying preliminary results from measurements can be found in appendix A.

3.4. DESIGN FOR FINAL PROTOTYPE

Most designs found in appendix A preceding the final prototype have a tunable magnet configuration: by turning the screws, the distance between the magnets can be adjusted, enabling the stiffness levels to be tuned. While this is very convenient, it results into a prototype that is quite large, also in the excitation direction, which is exactly against the problem that is to be solved. Consequentially, the need arises for a prototype that has a fixed distance between the magnets, enabling a small length in the excitation direction. As such, a COMSOL model is used to determine the correct distance between the magnets.

3.4.1. DETERMINATION OF THE MAGNET DISTANCE

To find the required distance between the magnets, first the force required to deflect the beam must be found experimentally. Therefore, a force-displacement measurement has been taken for the piezo in uncompensated condition. A load resistance of $1\text{M}\Omega$ was connected to the piezo during the measurement. The results can be found in figure 3.5b.

To find the distance between the magnets, first one needs to have magnets. As can be seen in appendix A, one of the preceding prototypes has disc magnets clamped to the tip of the beam. The mass of these disc magnets forming the proof mass proved to be suitable, therefore a rectangular block magnet of about equal size and mass was sourced from HKCM Engineering. After having found the proof mass magnet, the endstop magnets needed to be found. Bar magnets were chosen with equal height of that of the proof mass, allowing 2D magnetics simulation (So the out of plane dimension in the simulation is the same).

Next, the distance between the magnets can be found by simulation of magnetic forces by using COMSOL Multiphysics 2D magnetics. Figure 3.4 shows the flux density contour plot of the simulation. The upper and lower magnets are the fixed magnets, the middle is the proof mass magnet. It is shown in the upper outmost position and it can be seen that the proof mass magnet is slightly rotated which is due to the tip rotation of the piezoelectric beam. A rectangle of air is modelled around the magnets to represent the medium in which the magnets are present.

To find the force-displacement relation, the parametric sweep function is used. In this way, a certain calculation can be repeated by sweeping over a parameter. In this case, it is the lateral displacement of the proof mass. The proof mass is displaced in steps over its displacement limit and at each step, the magnetic force between the proof mass magnet and fixed magnet is evaluated. As a result, a force-displacement relationship is found.

However, this only results into a force-displacement for a certain magnet distance. Therefore, to find the correct magnet distance, another parametric sweep is applied over the magnet distance. In this way the correct magnet distance can be easily found by checking which negative stiffness curve matches best with the measured curve of the piezo. In figure 3.5a the negative stiffness is shown for magnet distances between 4 and 7 mm. Comparing the results to figure 3.2d, a difference may be spotted. In figure 3.2d, the stiffness is pretty nonlinear whereas it is linear in figure 3.5a. Apparently, the geometry of the magnet influences the stiffness nonlinearity. It has been observed that this nonlinearity plays a larger role in axisymmetric models/disc magnets than in the magnets that are used now; it has been observed that enlarging the fixed magnets does introduce nonlinearity, but not as extreme as in figure 3.2d. Figure 3.5b shows the resulting negative stiffness that is close to the stiffness of the piezo and that is used for further developing the harvester. To verify the model, the negative stiffness has been verified with the setup from 5. As can be seen from figure 3.5b, the negative stiffness is indeed linear.

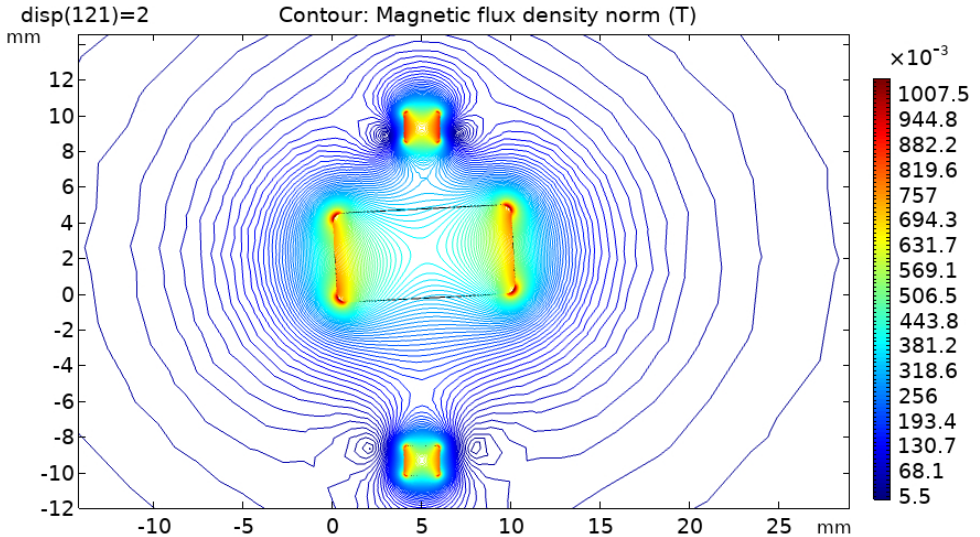


Figure 3.4: Flux density plot in the simulation.

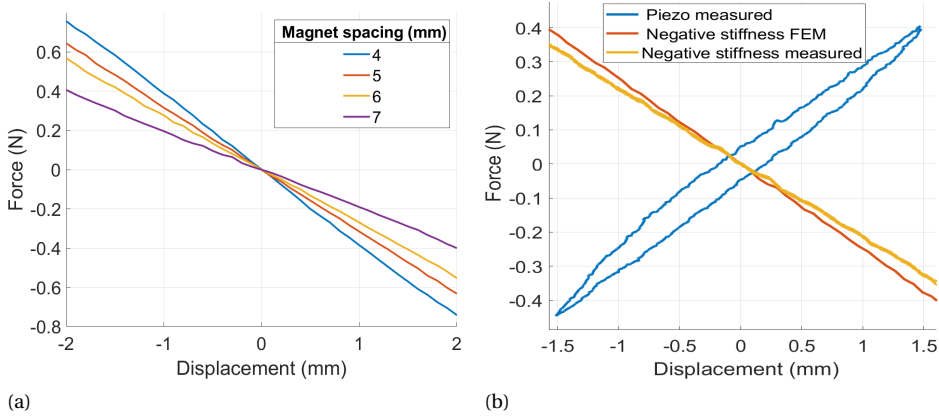


Figure 3.5: (a) Negative stiffness for various magnet distances, (b) measured positive stiffness of the piezo with simulated and measured negative stiffness from the magnets.

3.5. FINAL PROTOTYPE

In figure 3.6 renders, cross section views and an exploded view of the final prototype can be seen. The large block magnet is glued to the tip of the piezo by means of metal epoxy glue. A header is soldered to the terminals of the piezo to allow connection of wires. This avoids the risk of stripping off the terminals when a directly soldered wire is pulled too hard. Two frames printed in PLA with 100% infill clamp the piezo from both sides. Two M3 socket head cap screws in combination with M3 brass threaded inserts are used to firmly clamp the piezo. The threaded inserts have been pressed into the plastic with a soldering iron, melting the plastic around the insert to obtain a good fit of the insert. The other four threaded inserts are used to connect the VEH. Four nylon M2 screws are used to clamp the two frames together around the magnets. Non-conductive screws were chosen here to prevent possible eddy currents. The frame was printed just a little larger in the excitation direction. This is for the reason that the magnet distances are not a perfect prediction and of course there is a tolerance in the printing. By printing it a little larger, sanding it down and iteratively testing for stability, a good zero-stiffness condition can be obtained.

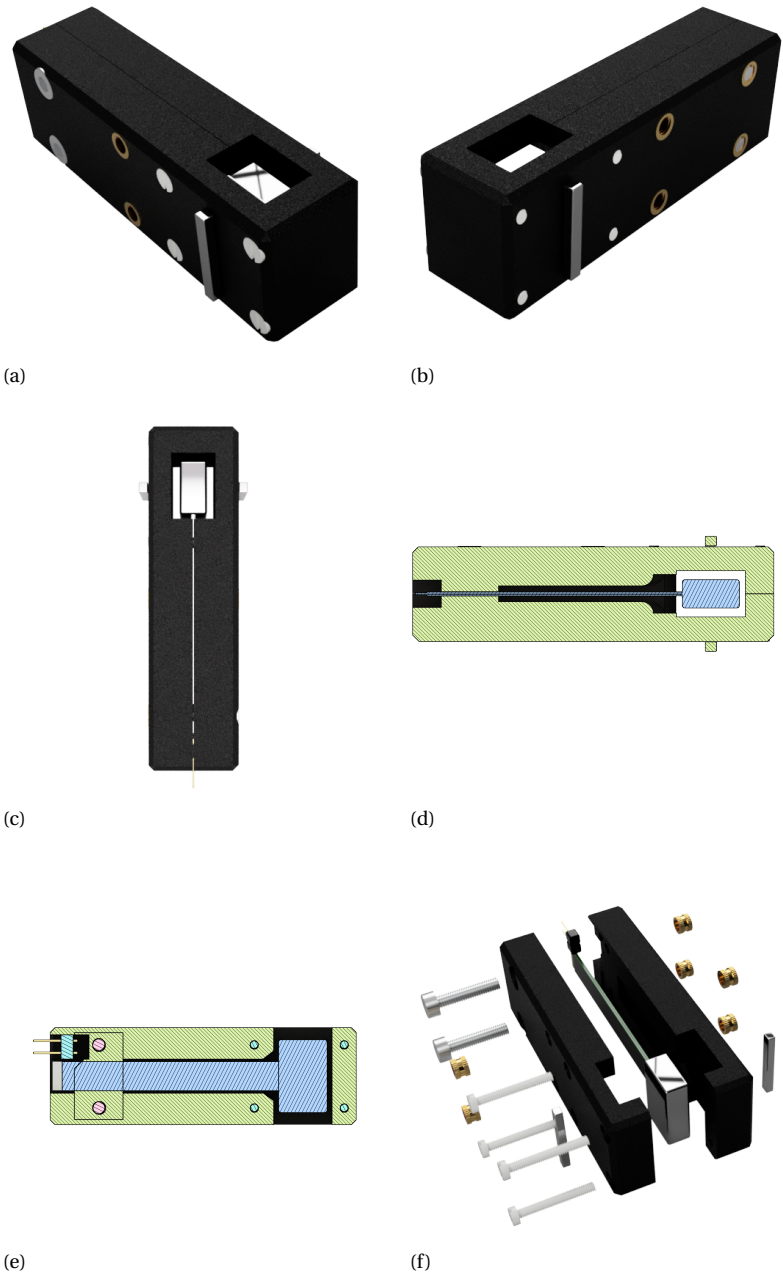


Figure 3.6: Renders and cross-sections of the final design.

4

MODEL

In this chapter, the approach for modelling the dynamics of the stiffness compensated energy harvester is extensively discussed. A distributed parameter model is used from literature and its derivation is shown. The model is further developed by including the mechanics of the harvester in this work.

4.1. MECHANICS OF A PIEZOELECTRIC ELEMENT

Piezoelectric elements can be classified as transducers. That means, dynamics in the electrical domain are transduced to for example the mechanical domain and the other way around. This working principle can already be noticed in the constitutive equations of a piezoelectric element [12] .

$$S = s^E T + d E \quad (4.1)$$

$$D = d T + \epsilon^T E \quad (4.2)$$

Where S is the strain, s^E is the compliance under constant electric field, T is the stress, d is the charge constant, E the electric field, D the electric displacement and ϵ^T the permittivity under constant stress. The interpretation of the constitutive equations is straightforward: the induced strain in the element is equal to the sum of the mechanically induced strain and the strain induced due to the electric field that is formed through polarization of the material. When the element is short-circuited, no electric field can be generated and thus the strain is merely present due to mechanical stresses. Furthermore, the electric displacement is equal to the displacement induced by stresses and by the electric field. If no mechanical stress is applied, the charge distribution will only be a result of the applied electric field, as in the case of a capacitor.

The foregoing clearly indicates the need for a model that considers the dynamics in both domains and that couples them together. Therefore, the model will consist of a system of two equations, similar to the constitutive equations shown above. The derivation of those will be shown in the following sections.

4.2. MODELLING APPROACH

Modelling a piezoelectric energy harvester in this specific case is far from straightforward. First, in order to obtain an accurate result in terms of output voltage and power, the distribution of displacement and strain along the beam length must be accurately known. This necessitates the use of a distributed parameter or continuum model. Lumped parameter models are available as well [13], but these are known to show inaccuracies and correction factors from distributed parameter models as in [14] are necessary to compensate for the loss of accuracy.

In [15], a distributed parameter model is described for a cantilever piezo beam that is used as a resonator. The model shows very accurate results compared to experiments. Modal analysis is used to find its dynamic deflection and voltage output. As the beam is driven into resonance, a certain mode shape is dominant which renders modal analysis as a useful tool. Now in the case of a statically balanced piezo beam, there is virtually no stiffness present. As a consequence, there will be no resonance (or at least a very low resonance frequency due to some remanent stiffness) and its accompanying mode shape.

Nevertheless, a deflection pattern must be present and it is likely to remain quite constant throughout low frequencies. The fixed magnets introduce a tip force on the proof mass magnet, resulting in a static deflection pattern. In the limit, a zero stiffness condition is achieved and then one could reason that the deflection can be described by that static deflection pattern of a cantilever beam with tip force and moment multiplied

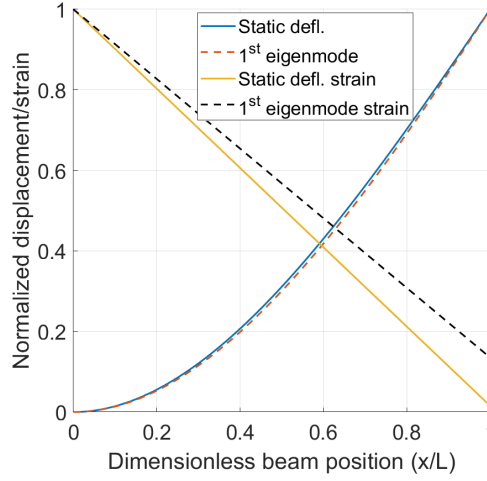


Figure 4.1: **Normalized deflection and strain for static deflection pattern and mode shape of the first eigenmode.**

by some temporal function:

$$\delta = \left(\frac{Px^2(3L-x)}{6YI} + \frac{Pdx^2}{2YI} \right) \sin \omega t \quad (4.3)$$

Where P is the load on the beam tip induced by the magnets, x is the beam coordinate, L the beam length, YI the bending stiffness and d the distance between beam tip and the center of gravity of the tip magnets, which induces a moment at the beam tip. The static deflection δ is plotted along with the first eigenmode from [15] in figure 4.1. The second derivative, which directly relates to strain is plotted as well. All curves have been normalized with respect to the largest value. As can be seen from the figure, the deflections from the static pattern and the eigenmode are very similar. The second derivatives show an increasing difference when moving toward the beam tip. Nevertheless, at the region where the strain is the largest, the difference is the lowest. Now the following can be deduced. Be it the case that all stiffness would be compensated, i.e. a perfect zero stiffness mechanism is produced, then the static deflection pattern δ could be used. On the other hand, if no stiffness were reduced, the eigenfunction of the first eigenmode could be used, so this sets the extremes inbetween which the deflection could be. It is observed that both cases are pretty similar in deflection and partially in strain. As it not clear yet what the exact condition is going to be, it is justifiable to assume that the eigenfunction can be used to describe the deflection pattern.

The modelling approach is therefore as follows. First, modal analysis is used and for this, the model from [15], [14] is used. The derivation of this model is discussed in section 4.4-4.6. Once the equations of motion have been found for a cantilever piezo beam, the endstops are included in the model. Next, the negative stiffness is added and the force-displacement data is added into the equations of motion. This is to account for hysteresis and remanent stiffness.

4.3. MODE OF OPERATION

Piezoelectric elements can be manufactured in all sorts of shapes and can also have different modes of operation. Piezoelectric constants denote the relation between mechanical and electric quantities, e.g. the relation between mechanical strain and electric field [12]. The vectorial direction of these quantities depend on the mode of operation. Constants as the piezoelectric constant d_{ij} have two subscripts i and j , which are the directions of poling and strain, respectively. In piezoelectric ceramics, there is a convention stating that '3' is by default denoted as the poling direction and all perpendicular directions to the poling direction as '1' [12]. So as a result, d_{33} means strain and electric field are in the same direction, enabling use as a linear actuator. In the case of a bending bimorph beam the d_{31} constant is used. This implies that the bending moment induced in the beam stretches the beam in its length direction, inducing an electric field in the transverse direction. This principle is shown in figure 4.2, where the directions have been indicated as well.

4.4. BEAM EQUATION

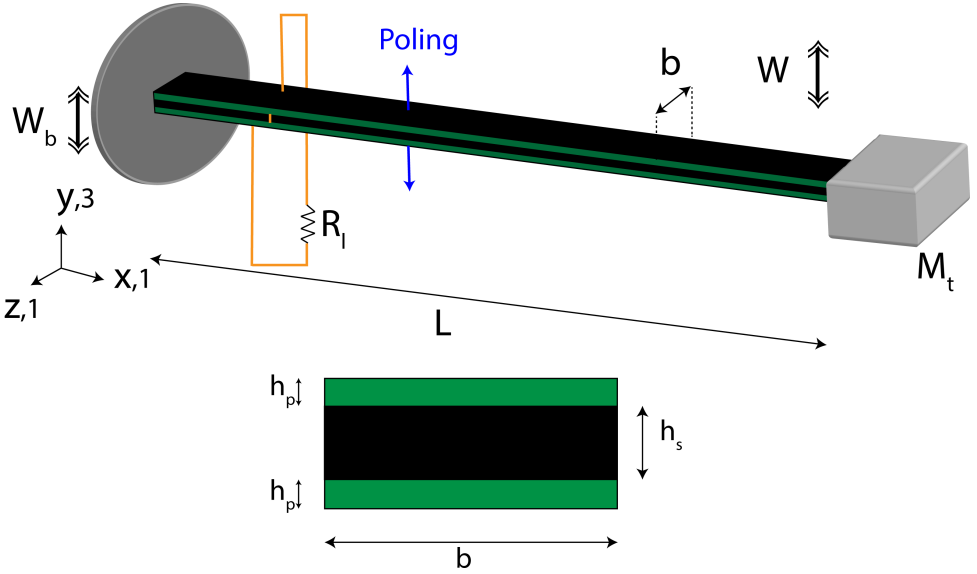


Figure 4.2: Diagram indicating model parameters. The lower figure shows the cross section of the beam.

The differential equation for the equation of motion (EoM) can be found as follows:

$$m \frac{\partial^2 w(x, t)}{\partial t^2} + C_s I \frac{\partial^5 w(x, t)}{\partial x^4 \partial t} + C_a \frac{\partial w(x, t)}{\partial t} + \frac{\partial^2 M(x, t)}{\partial x^2} = -(m + M_t \delta(x - L)) \frac{\partial^2 w_b(x, t)}{\partial t^2} \quad (4.4)$$

With

$$\frac{\partial^5 w(x, t)}{\partial x^4 \partial t} = \frac{\partial}{\partial t} \frac{\partial^4 w(x, t)}{\partial x^4} = \frac{\partial}{\partial t} \frac{\partial^2 M(x, t)}{\partial x^2} \quad (4.5)$$

Here M is the internal moment, C_s the Kelvin-Voigt strain rate damping, I the area moment of inertia, w the transverse displacement of the beam, C_a the viscous damping coefficient, m the mass per length, M_t the tip mass, w_b is the base excitation and δ is the Dirac delta function. The internal moment can be found by integration of the axial stresses encountered in the beam cross-section. As the beam is composite, this needs to be done for the piezoelectric and substrate layers separately. The internal moment can therefore be found as follows:

$$M(x, t) = -b \left(\int_{-\frac{h_s}{2} - h_p}^{-\frac{h_s}{2}} T_1^p y dy + \int_{-\frac{h_s}{2}}^{\frac{h_s}{2}} T_1^s y dy + \int_{\frac{h_s}{2}}^{\frac{h_s}{2} + h_p} T_1^p y dy \right) \quad (4.6)$$

Where b is the width of the beam, h_s the height of the substrate layer, h_p the height of the piezoelectric layer and T_1^{PS} the axial stress in piezoelectric and substrate layer, respectively. These can be formulated as follows:

$$T_1^S = Y_s S_1^S \quad (4.7)$$

$$T_1^P = c_{11}^E S_1^P - e_{31} E_3 \quad (4.8)$$

$$S_1(x, y, t) = -y \frac{\partial^2 w(x, t)}{\partial x^2} \quad (4.9)$$

With Y_s the Young's modulus of the substrate, S_1^{PS} the bending strain, c_{11}^E the Young's modulus of the piezoelectric layer, e_{31} the piezoelectric constant and E_3 the electric field. Substitution of eqns. 4.8-4.9 in eqn. 4.6 results in:

$$M(x, t) = -b \left(\int_{-\frac{h_s}{2} - h_p}^{-\frac{h_s}{2}} -c_{11}^E \frac{\partial^2 w}{\partial x^2} y^2 - e_{31} E_3 y dy + \int_{-\frac{h_s}{2}}^{\frac{h_s}{2}} -Y_s \frac{\partial^2 w}{\partial x^2} y^2 dy + \int_{\frac{h_s}{2}}^{\frac{h_s}{2} + h_p} -c_{11}^E \frac{\partial^2 w}{\partial x^2} y^2 - e_{31} E_3 y dy \right) \quad (4.10)$$

Evaluation of eqn. 4.10 results into:

$$M(x, t) = \frac{bc_{11}^E}{3} \frac{\partial^2 w}{\partial x^2} \left((h_p + \frac{h_s}{2})^3 - (\frac{h_s}{2})^3 \right) + \frac{be_{31}E_3}{2} \left(\frac{h_s^2}{4} - (h_p + \frac{h_s}{2})^2 \right) + Y_s I \frac{\partial^2 w}{\partial x^2} + \frac{bc_{11}^E}{3} \frac{\partial^2 w}{\partial x^2} \left((h_p + \frac{h_s}{2})^3 - (\frac{h_s}{2})^3 \right) + \frac{be_{31}E_3}{2} \left((\frac{h_s}{2} + h_p)^2 - (\frac{h_s}{2})^2 \right) \quad (4.11)$$

It is important to note that if the piezoelectric layers are connected in series, the polarisation of the bottom layer has to be in opposite direction with respect to the top layer. As the strain at bottom has an opposite sign with respect to the top, the direction of the generated charge or voltage is opposite as well. However, the due to series connection the voltages are summed up and a zero voltage will result if the polarisation direction is the same. Therefore opposite polarisation is necessary at one of the piezoelectric layers. This means that a minus sign may be added before the last term as this is the moment

term due to generated voltage. As a result, eqn. 4.11 can be simplified to:

$$M(x, t) = \frac{\partial^2 w}{\partial x^2} \left(Y_s I + \frac{2bc_{11}^E}{3} \left((h_p + \frac{h_s}{2})^3 - (\frac{h_s}{2})^3 \right) \right) + \frac{e_{31}b}{2} V \left(\frac{h_s^2}{4} - \left(h_p + \frac{h_s}{2} \right)^2 \right) (H(x) - H(x-L)) \quad (4.12)$$

Notice the inclusion of the Heaviside step function $H(x)$. The reason of the inclusion of this function is twofold: first, it is necessary as to guarantee that the voltage coupling term remains to exist when plugging it into eqn. 4.6. Otherwise, the term would drop due to double differentiation in x . Furthermore, it allows for introducing the case where only a patch of piezoelectric layer instead of the full beam length. Notice that a voltage term V is present in eqn. 4.12 by recognizing that

$$E_3 = \frac{V}{2h_p} \quad (4.13)$$

Furthermore, the bending stiffness YI and coupling coefficient θ can be recognized as:

$$YI = \frac{2b}{3} \left(Y_s \frac{h_s^3}{8} + c_{11}^E \left((h_p + \frac{h_s}{2})^3 - \frac{h_s^3}{8} \right) \right) \quad (4.14)$$

$$\theta = \frac{e_{31}b}{2} \left(\frac{h_s^2}{4} - \left(h_p + \frac{h_s}{2} \right)^2 \right) \quad (4.15)$$

Substituting in eqn. 4.4, the following coupled beam equation is obtained:

$$m \frac{\partial^2 w}{\partial t^2} + C_s I \frac{\partial^5 w}{\partial x^4 \partial t} + C_a \frac{\partial w}{\partial t} + YI \frac{\partial^2 w}{\partial x^2} + \theta V \left(\frac{d\delta(x)}{dx} - \frac{d\delta(x-L)}{dx} \right) = -(m + M_t \delta(x-L)) \frac{\partial^2 w_b}{\partial t^2} \quad (4.16)$$

4.5. MODAL ANALYSIS

Solving the equations as partial differential equations is fairly complicated. A method to simplify the process is modal analysis. Here, a certain deformation pattern, called an eigenfunction or mode shape ϕ_i is dominant at a corresponding natural frequency ω_i . As such, the response can be split into a spatial eigenfunction $\phi_i(x)$ depending only on geometry and a temporal function $q(t)$ depending only on time. Multiplying these two will result in the response at or near that certain frequency. Repeating this process for every natural frequency and summing them, the infinite series in eqn. 4.17 shows the displacement for a general condition. Note the similarity to separation of variables, used for solving partial differential equations.

$$w(x, t) = \sum_{i=1}^{\infty} \phi_i(x) q_i(t) \quad (4.17)$$

The eigenfunction is defined as :

$$\phi_i = A_i \left(\cos \frac{\lambda_i}{L} x - \cosh \frac{\lambda_i}{L} x + \sigma_i \left(\sin \frac{\lambda_i}{L} x - \sinh \frac{\lambda_i}{L} x \right) \right) \quad (4.18)$$

with

$$\sigma_i = \frac{\sin \lambda_i - \sinh \lambda_i + \lambda_i \frac{M_t}{mL} (\cos \lambda_i - \cosh \lambda_i)}{\cos \lambda_i + \cosh \lambda_i - \lambda_i \frac{M_t}{mL} (\sin \lambda_i - \sinh \lambda_i)} \quad (4.19)$$

Details on the derivations of the derivations in this section can be found in suited textbooks [16], [14] In eqs. (4.18) and (4.19) λ_i is the eigenvalue corresponding to the i^{th} vibration mode and is related to its natural frequencies. It can be found through the following characteristic equation:

$$1 + \cos \lambda_i \cosh \lambda_i + \frac{\lambda_i M_t}{mL} (\cos \lambda_i \sinh \lambda_i - \sin \lambda_i \cosh \lambda_i) - \frac{\lambda_i^3 I_t}{mL^3} (\cosh \lambda_i \sin \lambda_i + \sinh \lambda_i \cos \lambda_i) + \frac{\lambda_i^4 M_t I_t}{m^2 L^4} (1 - \cos \lambda_i \cosh \lambda_i) = 0 \quad (4.20)$$

In eqn. 4.18, the eigenfunction has a scaling factor A_i . The magnitude of this scaling factor can be found by using mass normalization of the eigenfunction, which is implemented through the following orthogonality condition:

$$\int_0^L \phi_i(x) m \phi_j(x) dx + \phi_i(L) M_t \phi_j(L) + \left[\frac{d\phi_i(x)}{dx} I_t \frac{d\phi_j(x)}{dx} \right]_{x=L} = \delta_{ij} \quad (4.21)$$

Substituting for ϕ_i and separating A_1 , the following equation can be obtained, which can be evaluated numerically in MATLAB. From now on, i becomes a 1 since only the first eigenmode is of importance.

$$A_1^2 \left(m \int_0^L \left(\cos \frac{\lambda_1}{L} x - \cosh \frac{\lambda_1}{L} x + \sigma_1 \left(\sin \frac{\lambda_1}{L} x - \sinh \frac{\lambda_1}{L} x \right) \right)^2 dx + M_t \left(\cos \lambda_1 - \cosh \lambda_1 + \sigma_1 \left(\sin \lambda_1 - \sinh \lambda_1 \right) \right)^2 + I_t \frac{\lambda_1}{L} \left(-\sin \lambda_1 - \sinh \lambda_1 + \sigma_1 \left(\cos \lambda_1 - \cosh \lambda_1 \right) \right)^2 \right) = 1 \quad (4.22)$$

Having completely found ϕ_1 , by making use of equation 4.17, the beam equation 4.16 can be transformed into modal coordinates:

$$m \phi_1(x) \frac{\partial^2 q_1(t)}{\partial t^2} + C_s I \frac{\partial^4 \phi_1(x)}{\partial x^4} \frac{\partial q_1(t)}{\partial t} + C_a \phi_1(x) \frac{\partial q_1(t)}{\partial t} + Y I \frac{\partial^2 \phi_1(x)}{\partial x^2} q_1(t) + \theta V = f_1(t) \quad (4.23)$$

Through premultiplication of the same eigenfunction, vibration mode orthogonality conditions will result into:

$$\frac{d^2 q_1(t)}{dt^2} + 2\zeta_1 \omega_1 \frac{dq_1(t)}{dt} + \omega_1^2 q_1(t) + \theta \frac{d\phi_1(x)}{dx} \Big|_{x=L} V(t) = f_1(t) \quad (4.24)$$

where for sinusoidal excitations:

$$f_1(t) = -Y_0 \omega^2 \sin \omega t \left(m \int_0^L \phi_1(x) dx + M_t \phi_1(L) \right) \quad (4.25)$$

As can be seen, the viscous damping terms have been replaced by a single modal damping term ζ_1 , which can be experimentally assessed by e.g. measuring the logarithmic decrement in an impulse response. This provides a more straightforward method to obtaining the damping parameters.

4.6. CIRCUIT EQUATION

The electric displacement in the piezoelectric layer can be found as:

$$D_3 = d_{31} T_1 + e_{33}^T E_3 = e_{31} S_1^P + \epsilon_{33}^S E_3 \quad (4.26)$$

The relative permeability is mostly given in case of constant load, ϵ_{33}^T . The constant strain case ϵ_{33}^S can be found as a function of it. Next to that, the electric field E_3 can be expressed in terms of the voltage and the height of the piezoelectric layer.

$$\epsilon_{33}^S = \epsilon_{33}^T - d_{31}^2 c_{11}^E \quad (4.27)$$

$$D_3 = e_{31} S_1 - \epsilon_{33}^S \frac{V(t)}{h_p} \quad (4.28)$$

The piezoelectric constant e_{31} can be related to the charge constant and Young's modulus through:

$$e_{31} = \frac{d_{31}}{s_{11}^E} = d_{31} c_{11}^E \quad (4.29)$$

The strain can be found by substituting eqn. 4.9 for S_1 . An average bending strain is used through the use of h_{pc} , which is the distance between the center of the piezoelectric layer and the neutral axis of the composite beam.

$$D_3(x, t) = -d_{31} c_{11}^E h_{pc} \frac{\partial^2 w(x, t)}{\partial x^2} - \epsilon_{33}^S \frac{V(t)}{h_p} \quad (4.30)$$

Next, Gauss's law can be used to relate the electric displacement to the built up charge

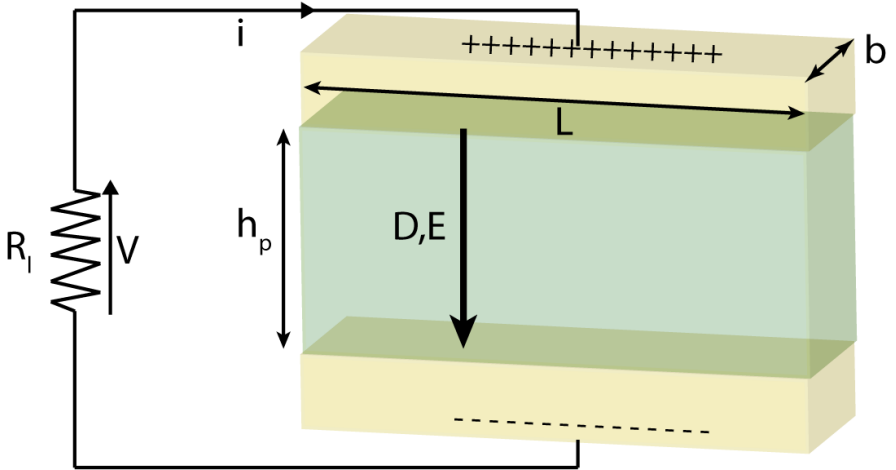


Figure 4.3: Schematic depiction of a piezoelectric capacitive element for the use of Gauss's law. Green indicates the piezoelectric material, yellow the electrodes.

and thus to the current. Figure 4.3 shows a depiction of how it is applied.

$$\frac{d}{dt} \left(\int_A \mathbf{D} \cdot \mathbf{n} dA \right) = \frac{V(t)}{R_l} = i(t) \quad (4.31)$$

The charge can be found as:

$$Q(t) = -b \int_0^L d_{31} c_{11}^E h_{pc} \frac{\partial^2 w(x, t)}{\partial x^2} + \epsilon_{33}^S \frac{V(t)}{h_p} dx \quad (4.32)$$

$$i(t) = \frac{dQ}{dt} = -b \int_0^L d_{31} c_{11}^E h_{pc} \frac{\partial^2 w(x, t)}{\partial t \partial x^2} dx - \frac{\epsilon_{33}^S b L}{h_p} \frac{dV(t)}{dt} \quad (4.33)$$

$$\frac{\epsilon_{33}^S b L}{h_p} \frac{dV(t)}{dt} + \frac{V(t)}{R_l} = -b d_{31} c_{11}^E h_{pc} \int_0^L \frac{\partial^3 w(x, t)}{\partial t \partial x^2} dx \quad (4.34)$$

Having found the circuit equation, modal substitution may be used though the use of eqn. 4.17.

$$\begin{aligned} \frac{\epsilon_{33}^S b L}{h_p} \frac{dV(t)}{dt} + \frac{V(t)}{R_l} = & -b d_{31} c_{11}^E h_{pc} \int_0^L \frac{\partial^2 \phi_1(x)}{\partial x^2} dx \frac{dq_1(t)}{dt} = \\ & -b d_{31} c_{11}^E \frac{h_p + h_s}{2} \frac{d\phi_1(x)}{dx} \Big|_{x=L} \frac{dq_1(t)}{dt} \end{aligned} \quad (4.35)$$

Looking at the circuit equation, one can identify the capacity and output current terms of the piezo. As a result, it can be seen that the output current is dependent on the applied strain and the velocity by which it deforms, i.e. it is related to the strain rate.

$$\frac{C_p}{2} \frac{dV(t)}{dt} + \frac{V(t)}{R_l} = I_p \quad (4.36)$$

Equation 4.36 can also be found by making use of Kirchhoff's circuit laws. A piezoelectric element can be modelled as a current source parallel to a capacitor. Connecting the lower and upper layer in series will result in the electric circuit as shown in figure 4.4. From the figure, one can easily deduce eqn. 4.36.

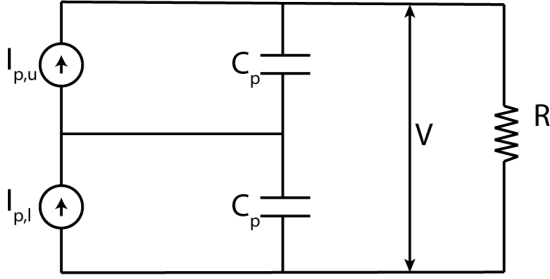


Figure 4.4: Electrical circuit representation of two in series connected piezoelectric elements.

4.7. MECHANICAL DAMPING

The mechanical damping of the cantilever is one of the parameters that is hard to find analytically. However, it can be assessed in a straightforward manner through experiments. One method is to put an impulse response to the cantilever and measure the response of the tip mass. Then through a logarithmic decrement the damping ratio can be assessed [16]. The logarithmic decrement method is defined as follows:

$$\zeta = (1/2\pi) \cdot \ln \frac{y_i}{y_{i+1}} \quad (4.37)$$

This is only valid for $\zeta \ll 1$. To find the damping, the unbalanced piezo was clamped and a Keyence LK-H052 laser sensor was used to measure the tip deflection. After flicking the tip, an impulse response is created. The results of this are shown in figure 4.5a. To find the real damping intrinsic to the piezo, it needs to be short circuited. In this way, no charge is built up influencing the stiffness and damping, thus measuring mechanical damping only. The open circuit condition is measured as well for comparison. Figure 4.5b shows the damping ratio found by eqn. 4.37. Their responses appear to be similar, however it can be seen that the open circuit damping ratio ζ is just a little lower, which can be explained by the increase in stiffness due to the built up charge. Interestingly, it is seen that in both cases no constant value for ζ can be found. Its value decreases almost linearly. At lower amplitudes uncertainty increases as the signal has an increased noise level and quantization errors become more prominent. Normally, when damping is purely viscous, ζ should remain about constant. This measurement indicates that damping in strongly coupled piezos is not purely viscous, as also pointed out in [10]. Nevertheless, an average viscous damping coefficient can be assessed by filtering out the uncertainty and taking the average. This amounts to an average damping ratio ζ of 0.026 for short circuit condition and 0.02 for open circuit.

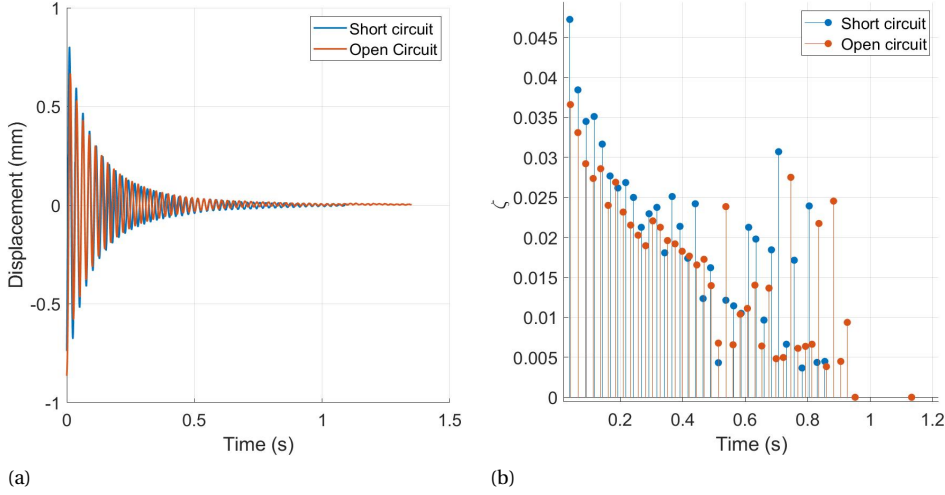


Figure 4.5: Measurements for finding the damping ratio, (a) impulse response, (b) damping ratios defined by consecutive peaks.

4.8. NEGATIVE STIFFNESS

As the mechanics and parameters for the resonating cantilever are known by now, negative stiffness can be added to the equation. One way to do it is to measure the stiffness of the cantilever or simulate it in FEM and add a negative stiffness to the equation. That means that the results from figure 3.5b could be used. However, this is prone to errors and it is hard to guarantee that the prototype has the exact same conditions. Furthermore, by subtracting the negative stiffness, a remanent stiffness is present, which is also present in the hysteresis measurement that will be included. As a result, the remanent stiffness will then be present twice. A better way is to use the bending stiffness YI that is already present in the equations. Then to compensate the stiffness of the cantilever beam, a static tip deflection force must be counterbalanced. This tip force can be found by the following beam tip deflection equation:

$$w(L) = \frac{FL^3}{3YI} \quad (4.38)$$

Note that only a tip force is used and no tip bending moment. As the tip boundary condition in the model is located at the tip of the beam, only the tip force needs to be included to deform it.

Subtraction of this force in the EoM will remove all bending stiffness of the beam resulting into a situation of $F = 0$ as bending stiffness. So in this case, a zero stiffness condition is achieved. This results into a clean slate for the bending stiffness. Measuring the force-displacement of the stiffness compensated prototype will yield the real level of stiffness in the VEH. Adding this into the EoM will result into an accurate representation of the bending stiffness that is left in the compensated condition.

4.9. ENDSTOPS

To avoid overload of the piezoelectric beam and to transfer kinetic energy to it through impact, endstops need to be included and thus need to be included in the model as well. In the case where the proof mass attached to the beam collides with a hard surface, a rapid stiffening occurs in the force-displacement graph. This allows the endstop to be modelled as a spring with a large stiffness. Furthermore, energy is partly converted to heat as well through the impact. This energy loss can be modelled by introducing a viscous damper element in parallel to the spring [17].

In figure 4.6, a diagram is shown that depicts how the endstop is modelled. In general, inclusion of endstops in the equations of motion can be implemented as shown in the following lumped parameter equation:

$$M\ddot{w} + C\dot{w} + Kw + f^{stop}(w) = F(t) \quad (4.39)$$

where

$$f^{stop}(w) = \begin{cases} K_{stop}(w - w_{stop}) + C_{stop}\dot{w} & \text{if } w \geq w_{stop} \\ 0 & \text{if } |w| < w_{stop} \\ K_{stop}(w + w_{stop}) + C_{stop}\dot{w} & \text{if } w \leq -w_{stop} \end{cases} \quad (4.40)$$

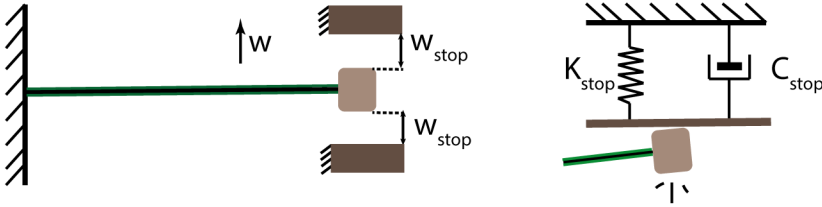


Figure 4.6: Spring-damper representation of the endstops.

4.9.1. ENDSTOP STIFFNESS

The stiffness and damping parameters of the endstops are not defined in a straightforward manner as in practise they are not embodied by spring or dampers; they are rather properties of the rigid material of which the endstop is made. As such, in this case it is a contact stiffness that is encountered, which may be modelled through the use of Hertz contact mechanics. As the proof mass magnet is filleted in its corners and only these corners make contact with the endstop, it may be seen as a contact between a cylinder and a plate. The relevant equations for Hertz contact mechanics are given by [18]:

$$Y' = \left(\frac{1 - \nu_1^2}{2Y_1} + \frac{1 - \nu_2^2}{2Y_2} \right)^{-1} \quad (4.41)$$

$$\frac{1}{R'} = \frac{1}{R_{x'}} + \frac{1}{R_{y'}}, \quad \frac{1}{R_{x'}} = \frac{1}{r_{1x}} + \frac{1}{r_{2x}}, \quad \frac{1}{r_{y'}} = \frac{1}{r_{1y}} + \frac{1}{r_{2y}} \quad (4.42)$$

$$K = \frac{dF}{d\delta} = Y'(2R'\delta)^{1/2} \quad (4.43)$$

Here Y' is the reduced Young's modulus, ν_i is the Poisson's ratio, Y the Young's modulus, R' is the combined contact radius, that is comprised of the radii in r_{ix} and r_{iy} of the components. The contact stiffness K is dependent on the indentation δ of the magnet in the endstop, generating a nonlinear stiffness profile.

In figure 4.7, it can be seen that the contact force behaves in a nonlinear relation to the indentation, which is generally seen in contact mechanics [19]. As the indentation increases, the contact load increases more rapidly. The contact stiffness between the endstop and the magnet is load dependent and therefore no singular stiffness value is to be found that characterizes the endstop stiffness. Therefore, a tangent stiffness must be found by constructing a tangent line to the contact load curve. To find the correct indentation and with that the correct endstop stiffness, a method of trial and error was used. An endstop stiffness value was used in the ODE-solver and then it was checked how much the displacement would overshoot the endstop distance (meaning indentation in the endstop material). This was iteratively done for a few frequencies and input accelerations. Eventually, this resulted in an endstop stiffness of 250kN/m with a corresponding indentation of $5\mu\text{m}$.

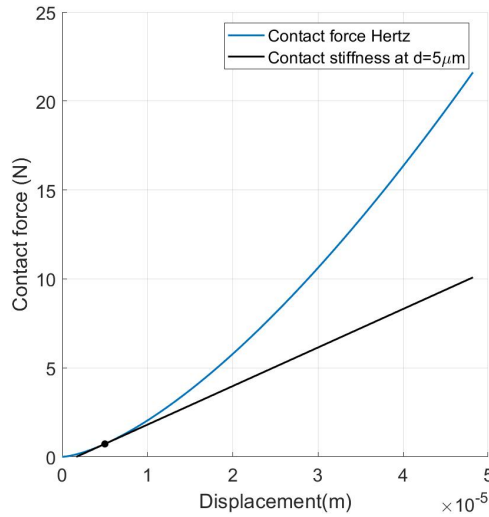


Figure 4.7: Contact force resulting from the Hertz contact stiffness formulation. Black tangent line indicates the contact stress at an indentation of $5\mu\text{m}$.

4.9.2. ENDSTOP DAMPING

Unlike the stiffness of the endstop, its damping coefficient is less easily found through simulations. Therefore, it is more straightforward to assess its order of magnitude through experimental methods. A method to find the endstop damping is through finding the coefficient of restitution and then convert that to a damping coefficient. The coefficient of

restitution (CoR) is defined as the ratio between the outgoing and ingoing velocity of the proof mass hitting the endstop, see eqn. 4.44.

$$CoR = -\frac{v_2}{v_1} \quad (4.44)$$

In [20], a method is provided to transform the CoR e into a damping coefficient:

$$\zeta = -\frac{\ln(e)}{\sqrt{\pi^2 + \ln(e)^2}} \quad (4.45)$$

$$c = 2\zeta \sqrt{K_{stop} \frac{m_1 m_2}{m_1 + m_2}} \approx 2\zeta \sqrt{K_{stop} M_t} \quad (4.46)$$

Here masses m_1 and m_2 are assigned to the proof mass and endstop, respectively. As the endstop can be thought of as a immovable object, its mass can be assumed to be infinite, which simplifies the formula.

To find the CoR, the velocities have to be found. Measuring them directly is not straightforward so they need to be derived from another measurement. One way is to measure the displacement and then numerically derive it to velocity, or derive it from the voltage output. The first option is more reliable as the latter requires a few intrinsic parameters of the piezo which introduces extra uncertainty.

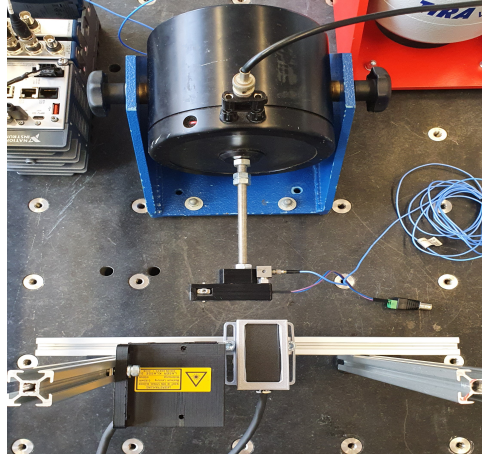


Figure 4.8: Setup used to assess the coefficient of restitution of the endstops.

In figure 4.8 the setup is shown that is used to measure the displacements. The energy harvester is attached to a shaker and an accelerometer is attached to the harvester to assess the acceleration to which it is subjected. Two laser sensors measure the displacement of the harvester frame and the displacement of the proof mass. Subtracting these from one another results in the relative displacement of the proof mass, which is shown in figure 4.9a. In blue the displacement of the proof mass is shown. It can be seen that it bounces from one endstop, whereas it only hits the other. In black the velocity is shown

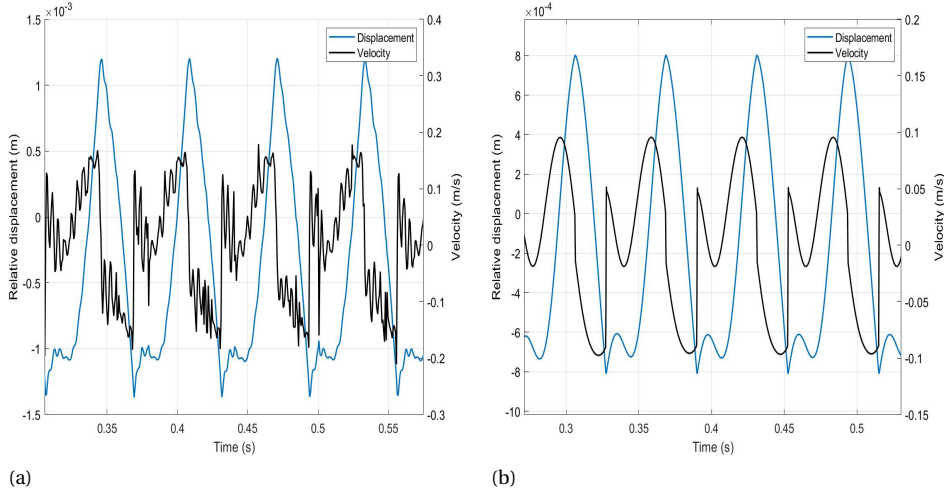


Figure 4.9: Displacement and velocity in (a) measurement and (b) simulation at 16Hz and 2g.

through numerical differentiation. Compared to the simulation, shown in figure 4.9b, it can be seen that displacement and velocity are quite similar in the general trend. The velocity has a large noise level, which is due to differentiation of the noise present in the displacement signal. Nevertheless, the dynamics are the same.

Taking the velocities just before and after the endstop collision, the CoR can be found. This has been done for 18 impacts, resulting in a CoR of $e=0.615\pm0.071$, which is equal to a damping coefficient of 15 Ns/m. Figure 4.10 shows the relation between the CoR and the damping ratio. The uncertainty propagation to the damping coefficient can be found through eqn. 4.48 and is equal to 2.85 Ns/m.

$$\sigma_c = \left. \frac{\partial c}{\partial e} \right|_{e=\bar{e}} \cdot \sigma_e \quad (4.47)$$

$$\sigma_c = \frac{2 \left(\sqrt{\pi^2 + \ln(e)^2} - \frac{\ln(e)^2}{\sqrt{\pi^2 + \ln(e)^2}} \right)}{e(\pi^2 + \ln(e)^2)} \cdot \sqrt{K_{stop} M_t} \quad (4.48)$$

4.10. INCLUSION OF FORCE-DISPLACEMENT DATA

Up till now, the zero stiffness condition is implemented as $F=0$ since the entire bending stiffness has been removed from the EoM. This is in the limit the ideal case of zero stiffness and is far from realistic, as piezos are known to behave hysteretically. Therefore, the force-displacement characteristics of the stiffness compensated piezo are measured and this is used as an input to the EoM to make the situation more realistic. Figure 4.12a shows the measurement taken for a compensated piezo connected to a 1MΩ load, which is the load used to compensate the system. The figure shows the raw data as well as the spline interpolated data in order to make it processable. The data has been split into

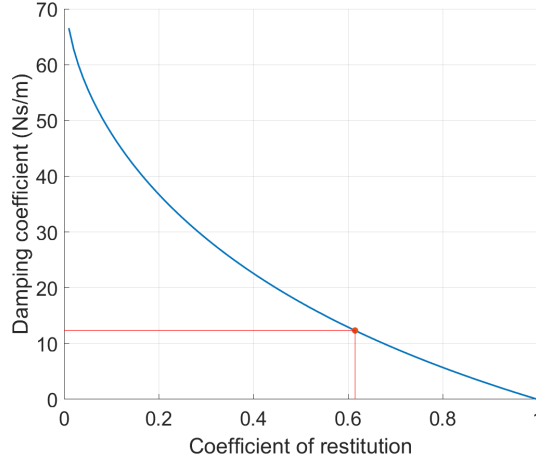


Figure 4.10: **Relation between CoR and damping coefficient.**

two curves and has been fitted by spline interpolation as seen in figure 4.12b. These two curves are used as an input to the EoM. The ODE-solver detects when an endstop is hit and when that happens, the input to the EoM switches to the other curve. This process is shown in figure 4.11. The hysteretic force may then be interpreted as follows:

$$f^{hyst}(w) = \begin{cases} f_{asc}^{hyst}(w) & \text{after } w + w_{stop} = 0 \\ f_{desc}^{hyst}(w) & \text{after } w - w_{stop} = 0 \end{cases} \quad (4.49)$$

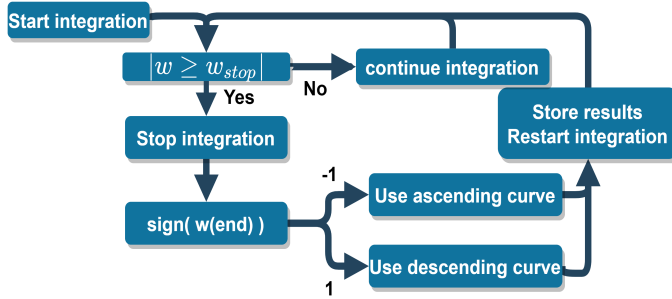


Figure 4.11: **Flowchart indicating how the ODE-solver deals with hysteresis curve switching.**

Note must be taken that this method of describing the hysteretic force in compensated state during quasi-static deflection is far from complete. With this implementation, the hysteretic force remains on a curve once an endstop is hit. It will only flip to the other curve once the other endstop is hit afterwards. This is not necessarily what happens in practice, as figure 4.12c demonstrates. Here, first the peak-peak displacement is applied after which the displacement amplitude is consecutively lowered. This clearly demonstrates that when a displacement is reversed before hitting an endstop, a new distinctive

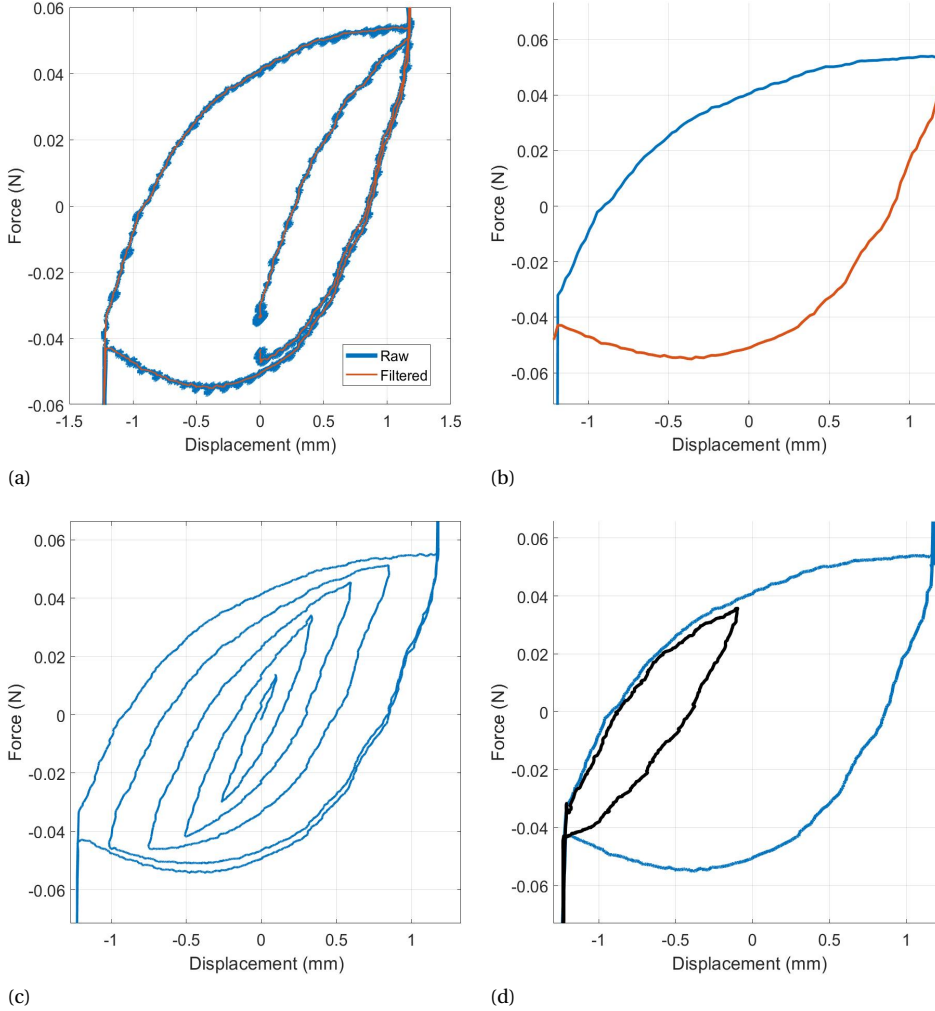


Figure 4.12: Measured force-displacement at compensated condition with in (a) raw measured and interpolated data, in (b) interpolated data split into two functions. Figure (c) shows small-displacement behaviour, (d) exaggeration of what happens after a rebound from an endstop.

internal load path is created. Nevertheless, the force eventually converges back to the peak force-displacement point, which is a phenomenon named curve alignment. This can also be found in actuators in the relation between input voltage and displacement [21]. Methods are available to model this behaviour as shown in chapter 5.

Furthermore, when the proof mass bounces from an endstop, according to this approach the hysteretic force would remain on the curve it has just switched to. This is also not entirely the case, as demonstrated in figure 4.12d. In the figure, a bounce from the left endstop is shown with an exaggerated magnitude. Once it bounces from an endstop,

another smaller internal loop is created near the endstop. In practice, this effect shall not have much influence, as the amplitudes from a rebound are quite small (i.e. less than 0.1 mm).

Although the previous things pointed out may devaluate the method, they don't necessarily form a problem. As long as full peak-peak displacements are obtained, the method is representative, and peak-peak displacements are mostly of interest as they generate the most power. It is more likely to be problematic when only one endstop is made contact with. All in all, the approach taken is a good start for now. The results in figure 4.12c follow a certain pattern that could be captured in a model as well and that could be a potential improvement when non-peak peak displacements are to be studied.

4.11. COMPLETE FORM OF EQUATIONS OF MOTION

Now all parts of the mechanics have been analysed, they can be assembled into the final form of the EoM. Eqn. 4.24 formed the mechanical equation and eqn. 4.36 the circuit equation. The mechanics of the endstops, negative stiffness and hysteresis can then be added to former equation resulting into:

$$\frac{d^2 q_1(t)}{dt^2} + 2\zeta_1 \omega_1 \frac{dq_1(t)}{dt} + \omega_1^2 q_1(t) + \theta \left. \frac{d\phi_1(x)}{dx} \right|_{x=L} V(t) + \phi_1(L)^2 f^{stop} - \phi_1(L)^2 \frac{3YI}{L^3} q_1(t) + \phi_1(L)^2 f^{hyst} = f_1(t) \quad (4.50)$$

$$\frac{C_p}{2} \frac{dV(t)}{dt} + \frac{V(t)}{R_l} = I_p - b d_{31} c_{11}^E \frac{h_p + h_s}{2} \left. \frac{d\phi_1(x)}{dx} \right|_{x=L} \frac{dq_1(t)}{dt} \quad (4.51)$$

where for sinusoidal excitations:

$$f_1(t) = -Y_0 \omega^2 \sin \omega t \left(m \int_0^L \phi_1(x) dx + M_t \phi_1(L) \right) \quad (4.52)$$

Note that the added terms are premultiplied by $\phi_1^2(L)$. The reason for that is as follows: going to modal coordinates requires the modal transformation from eqn. 4.17. Furthermore, through the orthogonality condition, the terms need to be premultiplied by $\phi_1(x)$ once again. The mechanics act at the tip of the beam, resulting in a $\phi_1^2(L)$ term. As the added mechanics are actually part of the partial differential equation, these terms need the orthogonality multiplications as well.

5

RESEARCH PAPER 1

In this paper, force-displacement measurements are carried out for the uncompensated and compensated piezoelectric beam. The effect of load resistance on the stiffness of the compensated beam is investigated as well as the effect of deformation rate. Furthermore, memory effects encountered in the hysteresis of piezoelectric actuators are also found in the force-displacement behaviour. It has been shown that the effect of a load resistance on the stiffness strongly depends on the deformation rate.

On the mechanical behaviour in stiffness compensated piezoelectric beams - an experimental investigation towards energy harvesting

E. van de Wetering, T.W.A. Blad and R.A.J. van Ostayen

Abstract—In this work, the stiffness of a piezoelectric cantilever beam is compensated through addition of attracting magnets which add a negative stiffness. The main purpose for this mechanism is low frequency energy harvesting at large input motions. To investigate the effect of deformation speed on the stiffness of the compensated beam, force-displacement measurements are taken at different speeds and with different load resistors connected. It has been found that the effect of the load resistance on the stiffness of the mechanism strongly depends on the deformation speed. A load that results in the same stiffness as in a closed circuit at low deformation speed results in a stiffer response at a faster deformation speed. Due to charge reduction, this stiffening is temporary. Therefore, the stiffness decreases over time to the stiffness of the closed circuit condition corresponding to that deformation speed. Furthermore, memory effects in the hysteresis found in piezoelectric actuators (curve alignment, wipeout), related between input voltage and displacement, were also confirmed between displacement and force in sensor application through force-displacement measurements. It has been concluded that stiffness compensation of a piezoelectric beam through addition of attracting magnets is a feasible method to produce a statically balanced piezoelectric beam that can be used as an energy harvester.

Keywords: Piezoelectricity, static balancing, zero stiffness, stiffness compensation, hysteresis, vibration energy harvesting

1. Introduction

In vibration energy harvesting, one method for transducing vibrations into electricity is by means of a piezoelectric element. A piezoelectric beam is frequently utilized in such a way that it is driven into one of its resonant vibration modes, preferably the first mode [1], [2]. Others use piezos by impacting them at a low frequency, generating an impulse response in the piezo at its resonant frequency, known as frequency upconversion [3], [4]. Another relatively unexplored method is static balancing of a piezoelectric beam. In this way, the

stiffness of a beam or mechanism is compensated through addition of negative stiffness elements [5]. In the limit, the total stiffness reduces to zero. The mechanism is then said to be statically balanced and as a result, the mechanism becomes neutrally stable within a certain displacement range. This configuration can be a solution to the problem that was discussed in [6], where prior art in energy harvesting was analysed. It was found that energy harvesters have a relatively poor performance at low frequency excitation with large input amplitudes. Stiffness compensation ensures that a stiff piezo can be deformed easily at these conditions so that a decent amount of power may be generated.

To successfully bring a piezo in a stiffness compensated condition and to model its behaviour, knowledge about the piezoelectric mechanics is necessary. Piezoelectric elements are known to show a wide range of nonlinear behaviour. When it comes to piezoelectric actuators, a lot can be found in prior art. Piezoelectric actuators are known to behave hysteretically. In [7], a model was developed to compensate for hysteretic effects in actuation. In [8] several types of hysteresis models were reviewed, among which rate-independent and rate-dependent. This rate dependence influences the shape of the hysteresis loop. When a sinusoidal voltage is applied as input and the frequency is varied, it was shown that the peak displacement reduces and the hysteresis loop widens [9], [10]. Furthermore, certain memory effects in hysteresis such as curve alignment and wipeout were investigated in [11].

However, when it comes to sensory or energy harvester applications, specifically in a statically balanced state, little is known about the electromechanical behaviour of such a piezoelectric beam. In general, there is an electromechanical coupling that in the easiest case of energy harvesting is affected by the load resistance connected to the piezo [12]. This is often the impedance matched load to maximize power output [13]. Besides that, the effects mentioned in prior art considering piezos in actuation mode, could also play a major role in the force-displacement behaviour of a statically

balanced piezo.

In this paper, the force-displacement behaviour of a piezoelectric beam that is stiffness compensated through the use of attracting magnets is investigated experimentally. This concerns measuring the force-displacement characteristics at different speeds and different load resistances.

Section 2 will present the prototype, a short background on the electromechanic coupling and memory effects and it discusses the measurement setup used in the research. The results that were found are presented in section 3 to be discussed in section 4. The main findings and conclusions will be summarized in section 5.

2. Method

A. Mechanical design

In Fig. 1, a top view schematic of the stiffness compensated piezo and a render and cross-section of the implementation is shown. A Morgan Ceramics bimorph PZT-508 beam is clamped in a frame that is 3D printed at 100% infill in PLA. The physical and electromechanical parameters of the beam are shown in table I. Attracting magnets are used to introduce a negative stiffness that counteracts the stiffness of the beam. To find the right distance between the magnets, the stiffness of the uncompensated beam was found experimentally by quasistatic force-displacement measurements with a load of $1\text{M}\Omega$ connected. Then, an electromagnetic finite element simulation was carried out in COMSOL Multiphysics to find the right magnet distance to generate a force counteracting that of the beam. To find the negative stiffness, the tip magnet was displaced by a parametric sweep. Another parametric sweep was applied on the magnet distances to find the setup to counteract the measured positive stiffness. The negative stiffness is shown in Fig. 5.

B. Electromechanical background

It is known in literature that the piezoelectric coupling affects the resonance frequency of the piezoelectric beam [1]. A closed circuit condition results into a lower resonance frequency than open circuit. This is for the reason that in an open circuit the charge is unable to flow away, resulting in an additional bending moment and stiffening of the beam. When a load resistance is connected, the magnitude of the load resistance determines how quickly the built up charge can flow away, thus affecting the stiffness. As a result, the resonance frequency can be altered by selection of the load resistance.

As buildup and flow of charge are directly related to stiffness, it also determines how persistent a

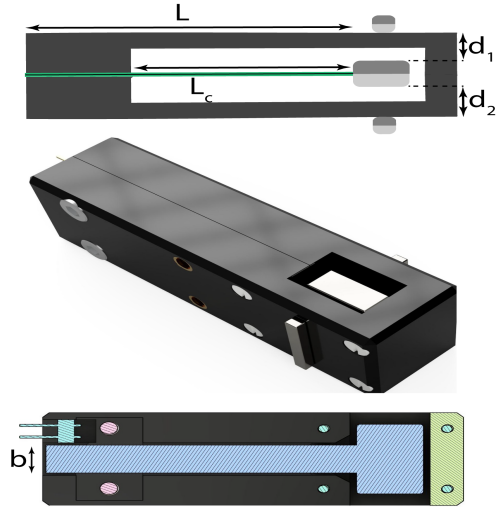


Fig. 1: Top view schematic, render and lateral section view of the statically balanced piezoelectric beam.

TABLE I: PZT-508 beam and magnet specifications.

Parameter	Symbol	Value
Beam length	L	46 mm
Free length	L_c	32 mm
Beam width	b	6 mm
Substrate thickness	h_s	0.37 mm
Piezo thickness	h_p	0.19 mm
Capacitance single layer	C	36.22 nF
Relative permittivity	ϵ_{r33}^T	3900
Charge constant	d_{31}	-315 pC/N
Piezoelectric constant	e_{31}	-19.2
Elasticity Piezo	Y_{33}^E	61 GPa
Elasticity Substrate	Y_s	200 GPa
Beam mass	m	0.95 g
Tip magnet size	-	15x10x5 mm
Fixed magnet size	-	15x2x1.8 mm
Distance between magnets	$d_{1,2}$	5.65/5.82 mm
Tip magnet flux density	B_T	1.17 T
Fixed magnet flux density	B_F	1.08 T

stiffening effect can be. This effect is schematically depicted in Fig. 2. Here, the force-displacement graph of the compensated beam is sketched. The open circuit (OC) and closed circuit (CC) conditions form the upper and lower boundaries for the stiffness. The endstops introduce a rapid stiffening when the tip magnet hits the PLA frame. This is shown by the bold black line. A curve that starts from the endstop stiffens increasingly with the load resistance. This stiffening is temporary, as the built up charge flows away.

C. Memory effects

In [11], memory effects of piezoelectric hysteresis were investigated for a piezoelectric element in actuation mode (voltage as input and displacement as output). It introduced the concept of turning points, which are local extrema in displacement,

see the numbered dots in Fig. 3. The theory of turning points was as follows. If a displacement-voltage curve starting from a turning point reaches a new turning e.g. **2** to **3**, then the next curve that is in reverse direction to **4** slowly converges back to the previous turning point **2**. The curves are seen to align themselves to converge to that point and the effect was therefore named curve alignment. Furthermore, when a voltage-displacement loop is closed, all curves inside the loop are erased from the hysteretic memory effect. This was called the wipeout effect. This means that if the curve from **6** reaches **5** again and continues to **3**, the closed loop **5-6-5** within the closed loop **3-4-3** does not affect the memory anymore.

As can be seen from Fig. 3, the inner curves (e.g. **5-6**) have the same shape as the outer curve, **1-2**. The same goes for the descending curve. In [11], a model was developed to predict the trajectories of these inner curves, by only using characteristics of the outer curves. The following type of fit was used:

$$y(x) = k(1 + ae^{-\tau(x-x_1)})(x - x_1) + y_1 \quad (1)$$

$$k = \frac{y_2 - y_1}{x_2 - x_1} (1 + ae^{-\tau(x_2-x_1)})^{-1} \quad (2)$$

Where x and y are the data on the horizontal and vertical axes, respectively. To predict an inner ascending curve, one takes the outer ascending curve and fits eqns. 1 and 2 to it. Here, x_1 , x_2 , y_1 , y_2 are the voltage and displacement at the start and endpoints, respectively. Furthermore, a and τ are fitting parameters. Once the fitting parameters are found for the outer ascending curve, any inner ascending curve can be predicted by using the same constant values for a and τ and by knowing the start and endpoints. The same procedure is taken for the descending curves. These effects will also be investigated for the case of a stiffness compensated piezo.

D. Measurement setup

To measure the mechanical behaviour, a setup is built to measure the force-displacement at the uncompensated and compensated conditions. An overview of that setup is shown in Fig. 4. The setup consists of a Moons' 24Q-3AG stepper motor connected to an Almotion LT50-TR-G8-200 linear stage. A Futek LSB200 sensor is used to measure the force of which the signal is amplified by a Scaime CPJ analog transmitter. The displacement is measured by a Micro-Epsilon optoNCDT1300 laser distance sensor and ELC DR07 resistance decade boxes are used to set the load resistance. An ME-systeme AS28e accelerometer is used to record the

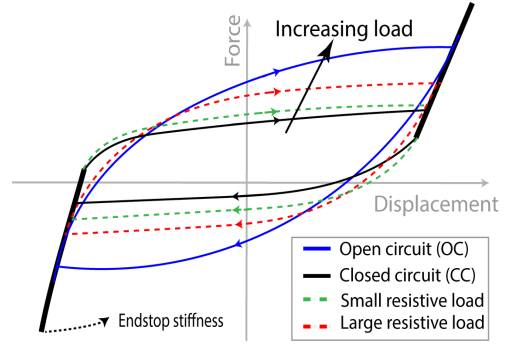


Fig. 2: Schematic diagram indicating the force-displacement behaviour of a stiffness compensated piezo under open circuit, closed circuit and load resistances.

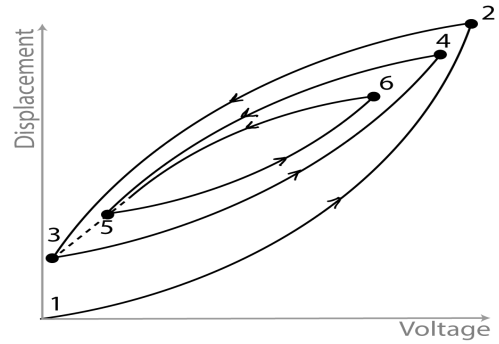


Fig. 3: Schematic displacement-voltage diagram indicating the curve alignment effect. Numbered dots are turning points and indicate the direction of the measurement.

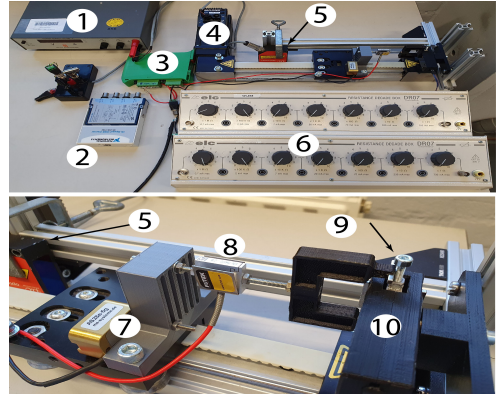


Fig. 4: Force-displacement setup with (1) power supply, (2) DAQ, (3) signal amplifier, (4) nema 24 stepper, (5) laser sensor, (6) resistance decade box, (7) accelerometer, (8) load cell, (9) magnetic contact and (10) prototype. Cabling has been removed to improve visibility.

acceleration applied to the stage. This is to check whether inertial forces are large enough to play a role in the measurements or whether they may be neglected. The outputs are measured by an NI 9215 DAQ which is analysed with the MATLAB data acquisition toolbox. The bracket connected to the load cell has magnets that magnetically attach to the screws attached to the tip magnet of the piezo.

E. Measurement procedure

The force-displacement measurements are taken at different rates expressed in a time period, which is the time it takes to go from one peak displacement to the other and back. At these rates, different load resistances are connected during the measurements. In this way, the rate dependent behaviour can be assessed.

As force-displacement measurements are carried out at different rates, inertial forces may come into play. To check whether these are negligible, first a spring steel flexure with a known bending stiffness equal to the bending stiffness of the piezoelectric beam and equal tip mass was deflected at faster rates. At the fastest rate in uncompensated condition, the maximum error would amount to 10%. Next, the flexure was compensated in stiffness as much as possible. The inertial forces encountered at the speeds for the stiffness compensated measurements were indistinguishable and can therefore be neglected.

To assess whether the curve alignment and wipeout effects also occur in the (compensated) force-displacement, a displacement pattern similar to the applied voltage in [11] is applied to the piezo. During this applied displacement, the force is measured.

3. Results

The force-displacement diagram of the uncompensated piezoelectric beam is shown in Fig. 5. The measurements are taken for different rates between 11.7 and 0.12 s. The negative stiffness from the FEM simulation is shown as well.

In Fig. 6a and 6b force-displacement measurements are shown for the beam in compensated condition and with different load resistances connected to the piezo, cf. Fig. 2. In Fig. 6a the time period equals 11.7 s and in Fig. 6b 1 s, so this measurement is taken at a faster rate. The same load resistances are used for comparison.

It can be seen in Figs. 5, 6a that within ± 0.5 mm the most linear stiffness is obtained. For the ascending curves at $1M\Omega$, the uncompensated state in Fig. 5 has a stiffness of 324 N/m whereas the compensated state in Fig. 6a has a stiffness of 26.3 N/m. This amounts to a linearized stiffness

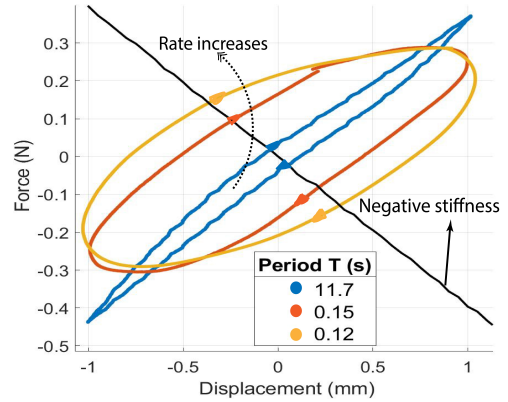


Fig. 5: Force-displacement measurement of the uncompensated beam at different speeds and a $1M\Omega$ load. The loop widens at larger speeds and the peak lowers. The negative stiffness is introduced by the magnets used for stiffness compensation.

reduction of 92 %. Comparing the uncompensated $1M\Omega$ to the compensated OC in the same region, a stiffness reduction of only 76% is obtained.

In Fig. 7 and 8, the force-displacement and applied displacement are shown for the assessment of the curve alignment and wipeout effects. The curve alignment is shown in blue and the wipeout in red. The results from the curve alignment are also fitted to predict the behaviour of the inner curves and this is shown in Fig. 9.

4. Discussion

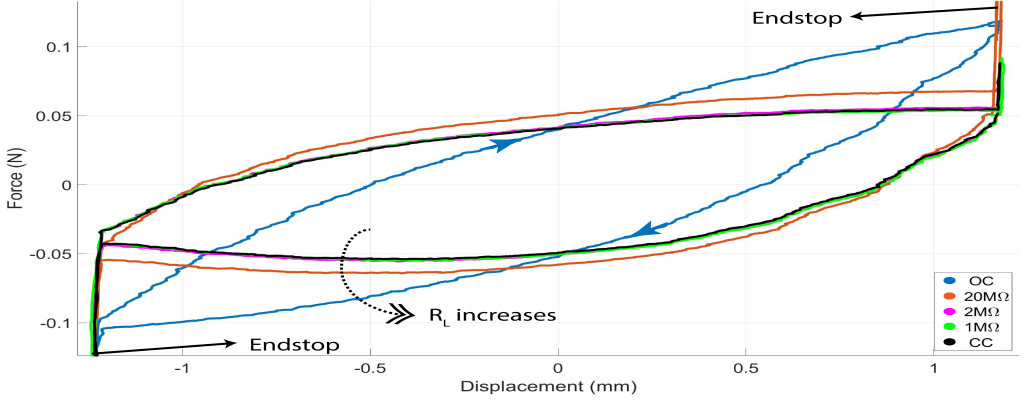
A. Rate dependence and directionality

Piezoelectric elements that are used as actuators are known to have a rate dependent hysteresis: the shape of the hysteresis loop is affected by the frequency of the input voltage [9], [10]. This phenomenon is also clearly visible in the uncompensated measurement in Fig. 5. For a fixed applied displacement, the hysteresis loop greatly widens at the faster rates and the peak force is reduced.

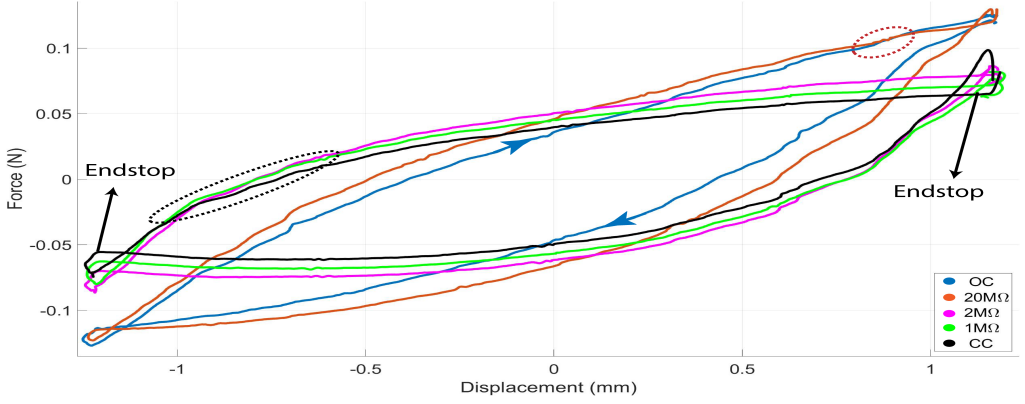
A certain directionality can also be seen in the peak forces. There is a slight difference in the positive and negative peak forces. Consequentially, the distance between the tip magnet and fixed magnets is not the same; one magnet needs to be positioned a bit closer to obtain a good stiffness compensation.

B. Load resistances and characteristic loads

Looking at Figs. 6a and 6b, several things can be noted. At peak displacement, a rapid stiffening is seen, which is due to the contact made with the



(a) Force-displacement measurement for the compensated beam at a time period of 11.7s.



(b) Force-displacement measurement for the compensated beam at a time period of 1s.

Fig. 6: Force-displacement measurements at compensated state at (a) slow and (b) faster rate. At the faster rate, the curves with lower load resistance become distinguishable from the closed circuit (CC) curve. Blue arrows at open circuit (OC) curve indicate the direction.

frame, acting as an endstop. The stiffness depends on the load connected to the piezo, as was clearly demonstrated by the stiffness reduction in section 3. The upper bound is set by the OC condition, the lower by the CC. Furthermore, it can be seen that when the displacement is reversed after an endstop hit, the curve stiffens. How persistent this stiffening is depends on the magnitude of the load. In the black encircled region in Fig. 6b, it can be seen that the $1\text{M}\Omega$ load crosses the $2\text{M}\Omega$ load, meaning that its stiffness is reduced just a little faster. Eventually, this stiffening diminishes due to reduction in charge and attains the same stiffness as the CC condition, i.e. it runs parallel to it. An exception to this is the OC curve.

This effect is also dependent on the speed by which the deformation took place. To characterize this, the load resistance R_L can be compared to a characteristic load R_c , which is from the impedance

TABLE II: Comparison between load resistance and characteristic load impedance

T (s)	$R_c(\text{M}\Omega)$	$R_L(\text{M}\Omega)$	R_L/R_c
11.7 (Fig. 6a)	103	20	0.19
11.7	103	1	0.0097
1 (Fig. 6b)	8.8	20	2.27
1	8.8	1	0.11

matching criterion [13].

$$R_c = \frac{1}{\omega C} \quad (3)$$

Table II shows a few of the characteristic loads, load resistances and their ratios for the two time periods. The first row shows a ratio of 0.19 resulting in a curve that is distinguishable from CC. The second row shows a ratio of 0.0097 and the result is indistinguishable from CC: the load resistance of $1\text{M}\Omega$ corresponding to this deformation speed is low enough to consider it as closed circuit. The

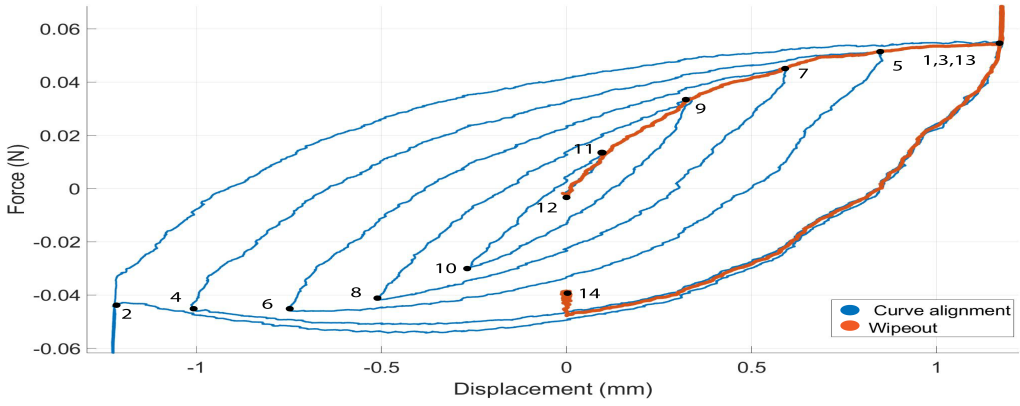


Fig. 7: Curve alignment and wipeout memory effects in the compensated beam. Numbered dots indicate the turning points and the order in which the measurement was taken.

third row is at a faster rate and shows a ratio larger than one. The effect is clearly seen in Fig. 6b, starting from the lower left corner: For the most part, the stiffness is equal to OC, but when the displacement becomes positive, it is seen that it slowly reduces due to charge reduction and the curve crosses OC in the region encircled in red. The last row shows a ratio of 0.11 and now at a faster rate its corresponding $1M\Omega$ load curve isn't indistinguishable from CC anymore. At the faster speed the $1M\Omega$ load is not to be considered the same as CC whereas it certainly was for the lower speed.

From the previous discussion, it can be seen that when $R_L \ll R_C$, then its corresponding curve approaches that of the CC condition. When R_L reaches the order of magnitude of R_C , the curve dissociates from the CC curve and becomes distinguishable. Furthermore, it can be seen that the basics of the force-displacement are defined by the CC condition. In this condition, virtually no charge can be built up. When a load is connected, charge can be built up and the system stiffens as the load impedes the charge from flowing away. Therefore, the magnitude of the load determines how persistent the stiffening effect is in time and displacement. The larger the load, the more persistent the stiffening is. Eventually, the charge reduces as much that the stiffness is equal to that of the CC condition: the curve corresponding to that load is then parallel to the CC curve.

C. Curve alignment and wipeout

In Figs. 7 and 8 the force-displacement and its corresponding applied displacement are shown to assess the memory effects. The turning points are indicated by the numbered dots. From the displacement plot, it can be seen that first a large

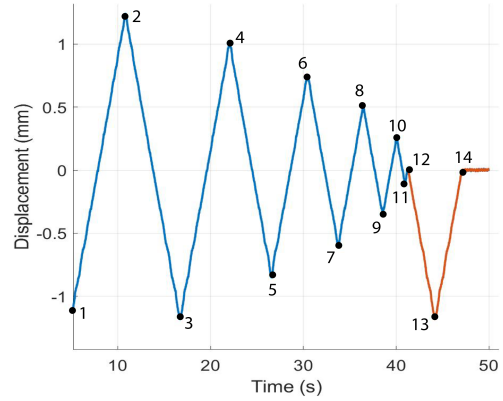


Fig. 8: Corresponding applied displacement to assess memory effects in the piezoelectric beam.

loop is created, after which the displacement amplitude is reduced with each subsequent curve. The force curve emanating from **3** reaches **4**, then the displacement is reversed and the force slowly converges back to **3** (it actually doesn't reach it as the displacement is once again reversed at **5** to reach **6**). This process repeats itself until point **12** and was named *curve alignment* in [11].

The other phenomenon that was found in actuators was the *wipeout effect*. This is effect is shown in red in the plots: after being reduced for several consecutive times, the displacement is now increased. The following curve now passes through previous turning points to escape from surrounding loops, ending up in the endstop at the right again. Now it follows the outmost path again to **14** and the foregoing history has no influence anymore: the memory is said to be wiped out.

From this, the following is observed, which is fully in line with [11]: a hysteretic force curve

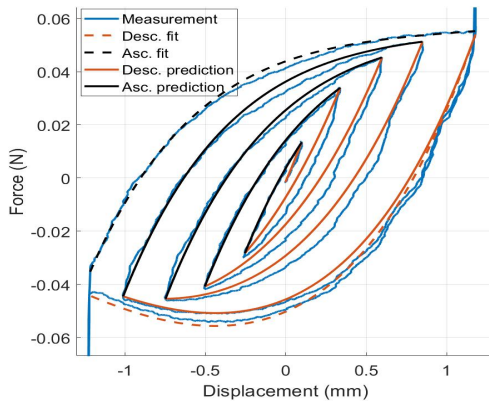


Fig. 9: By fitting the outer curves, parameters can be obtained to predict the inner curves.

5

surrounded by other curves is unable to cross those curves. It can only converge to the turning points previously created. These turning points are found when a curve is halted and the displacement direction is reversed. When a curve passes through a previous turning point forming a closed loop, the history associated to everything in that formed closed loop is then wiped out from the internal memory. When a loop is wiped out by passing through turning point n , the curve converges to turning point $n - 2$ if the displacement direction remains the same and to $n - 1$ if it reverses.

In Fig. 9, the curve alignment measurement is shown along with the dashed fit curves from eqns. 1 and 2 corresponding to the outer curves. It can be seen that fitting a and τ to an outer curve and using these to predict an inner curve results in a satisfactory prediction. The equations from [11] can be said to perform very well to predict the memory behaviour in the hysteretic force-displacement of a piezoelectric beam. It performs better for the ascending curves than the descending curves, which is likely due to the outer descending curve being a little different in shape compared to the inner descending curves.

This procedure can be very valuable for modelling the output of a stiffness compensated energy harvester. If the force-displacement data is used as an input to the equations of motion, only the outer curves are necessary to predict inner curves, i.e. to predict any form of non-peak-peak displacement. Furthermore, the findings considering the memory effects again depict the duality of piezoelectric elements between it being used as an actuator or as a sensor, or, the magnitude equality between the inverse and direct piezoelectric effect [12].

5. Conclusion

In this research, force-displacement measurements were taken for a piezoelectric beam that was stiffness compensated through the addition of attracting magnets. Compensated with a $1\text{M}\Omega$ load connected, the stiffness is reduced by 92% over a 1 mm range when it is deflected quasistatically. The force-displacement measurements were taken at different speeds and load resistances. It was found that the connected load resistance relative to the impedance matched load can be interpreted as an indication of how the force-displacement behaves in terms of stiffness. If the load resistance is equal to or larger than the impedance matched load the stiffness is temporarily equal to that of the open circuit condition. Due to charge reduction, this stiffness decreases over time. If the load resistance is several orders of magnitude lower than the matched load, the stiffness can be fully considered as short circuit condition. As such, a single load resistance can be seen as open circuit, short circuit or inbetween depending on the rate with which the piezo is deformed.

After a strain reversal at peak displacement, a stiffening occurs due to buildup of charge. The magnitude of the load affects this stiffening in such a manner that a larger load results into a stiffening that is more persistent throughout the displacement. Eventually, the stiffening effect diminishes due to a decrease in charge and the same stiffness as in closed circuit condition is obtained.

Furthermore, it was found that memory effects in the hysteretic behaviour, named curve alignment and wipeout, acting between voltage and displacement in actuators, are also seen in the relation between force and displacement. It was observed that fitting techniques used to predict hysteretic trajectories in piezoelectric actuators are very useful for predicting the force-displacement behaviour within a closed loop. This can be very useful when modeling the output of a stiffness compensated energy harvester. Last, it can be concluded that the act of compensating the stiffness of a piezo with attracting magnets can be a suitable procedure for designing a statically balanced piezoelectric beam, which can be used as an energy harvester.

REFERENCES

- [1] A. Erturk and D. J. Inman, "An experimentally validated bimorph cantilever model for piezoelectric energy harvesting from base excitations," *Smart Mater. Struct.*, vol. 18, no. 2, p. 025009, Feb. 2009. [Online]. Available: <https://iopscience.iop.org/article/10.1088/0964-1726/18/2/025009>
- [2] V. R. Challa, M. G. Prasad, Y. Shi, and F. T. Fisher, "A vibration energy harvesting device with bidirectional resonance frequency tunability," *Smart Mater. Struct.*, vol. 17, no. 1, p. 015035, Jan. 2008. [Online]. Available: <https://doi.org/10.1088%2F0964-1726%2F17%2F01%2F015035>

- [3] T. Galchev, E. E. Aktakka, and K. Najafi, "A Piezoelectric Parametric Frequency Increased Generator for Harvesting Low-Frequency Vibrations," *J. Microelectromechanical Syst.*, vol. 21, no. 6, pp. 1311–1320, Dec. 2012.
- [4] L. Gu and C. Livermore, "Impact-driven, frequency up-converting coupled vibration energy harvesting device for low frequency operation," *Smart Mater. Struct.*, vol. 20, no. 4, p. 045004, Mar. 2011. [Online]. Available: <https://doi.org/10.1088%2F0964-1726%2F20%2F4%2F045004>
- [5] A. J. Lamers, J. A. Gallego Sánchez, and J. L. Herder, "Design of a statically balanced fully compliant grasper," *Mechanism and Machine Theory*, vol. 92, pp. 230–239, Oct. 2015. [Online]. Available: <http://www.sciencedirect.com/science/article/pii/S0094114X15001342>
- [6] T. W. Blad and N. Tolou, "On the efficiency of energy harvesters: A classification of dynamics in miniaturized generators under low-frequency excitation," *Journal of Intelligent Material Systems and Structures*, vol. 30, no. 16, pp. 2436–2446, Sep. 2019. [Online]. Available: <https://doi.org/10.1177/1045389X19862621>
- [7] J. M. Rodríguez-Fortun, J. Orús, J. Alfonso, F. Buil, and J. A. Castellanos, "Hysteresis in Piezoelectric Actuators: Modeling and Compensation," *IFAC Proceedings Volumes*, vol. 44, no. 1, pp. 5237–5242, Jan. 2011. [Online]. Available: <http://www.sciencedirect.com/science/article/pii/S1474667016444381>
- [8] J. Gan and X. Zhang, "A review of nonlinear hysteresis modeling and control of piezoelectric actuators," *AIP Advances*, vol. 9, no. 4, p. 040702, Apr. 2019. [Online]. Available: <https://aip.scitation.org/doi/10.1063/1.5093000>
- [9] M.-J. Yang, C.-X. Li, G.-Y. Gu, and L.-M. Zhu, "A Modified Prandtl-Ishlinskii Model for Rate-dependent Hysteresis Nonlinearity Using m th-power Velocity Damping Mechanism," *International Journal of Advanced Robotic Systems*, vol. 11, no. 10, p. 163, Oct. 2014. [Online]. Available: <https://doi.org/10.5772/58984>
- [10] M. A. Janaideh, C.-Y. Su, and S. Rakheja, "Development of the rate-dependent Prandtl–Ishlinskii model for smart actuators," *Smart Mater. Struct.*, vol. 17, no. 3, p. 035026, Apr. 2008. [Online]. Available: <https://doi.org/10.1088%2F0964-1726%2F17%2F3%2F035026>
- [11] S. Bashash and N. Jalili, "Underlying memory-dominant nature of hysteresis in piezoelectric materials," *Journal of Applied Physics*, vol. 100, no. 1, p. 014103, Jul. 2006. [Online]. Available: <https://aip-scitation-org.tudelft.idm.oclc.org/doi/full/10.1063/1.2208805>
- [12] P. Groen and J. Holterman, *An Introduction to Piezoelectric Materials and Components*, 1st ed. Apeldoorn: Stichting Applied Piezo, 2012.
- [13] V. R. Challa, M. G. Prasad, and F. T. Fisher, "A coupled piezoelectric–electromagnetic energy harvesting technique for achieving increased power output through damping matching," *Smart Mater. Struct.*, vol. 18, no. 9, p. 095029, Aug. 2009. [Online]. Available: <https://doi.org/10.1088%2F0964-1726%2F18%2F9%2F095029>

6

RESEARCH PAPER 2

In this paper, the performance of the model from chapter 4 is evaluated by comparing it to the measured performance of the energy harvester. The harvester is excited at low frequency with a linear air bearing stage. It has been shown that for low frequencies, the model can predict the performance in terms of output power very well, but the error diverges as the frequency increases. Furthermore, the performance is benchmarked in terms of motion ratio and generator figure of merit. It has been demonstrated that for a certain range in motion ratio, this energy harvester has the largest generator figure of merit with respect to the known literature.

A stiffness compensated piezoelectric energy harvester for low frequency and large input excitations

E. van de Wetering, T.W.A. Blad and R.A.J. van Ostayen

Abstract—In this work, a stiffness compensated piezoelectric vibration energy harvester is modelled and tested for low frequency excitations and large input amplitudes. Attracting magnets are used to introduce a negative stiffness that counteracts the stiffness of the piezoelectric beam. This results into a nearly statically balanced condition and makes the harvester a nonresonant device. A distributed parameter model based on modal analysis is used to model the output of the energy harvester. This model is extended by including the negative stiffness, endstop mechanics and force-displacement data to the model. The peak RMS power amounts 1.20 mW at 9 hz and 3 g input acceleration. Furthermore, to benchmark the energy harvester in this work, the efficiency is evaluated in terms of generator figure of merit and is compared to prior art. This peak efficiency amounts to 0.567%, which is the highest value reported for its range of excitation. It is observed that only a factor of 1.38 is seen in the efficiency across the frequency response, which greatly contrasts the behaviour of resonating single-degree of freedom energy harvesters.

Keywords: Vibration energy harvesting, low-frequency, piezoelectricity, static balancing, zero stiffness, stiffness compensation

1. Introduction

In a world that increasingly implements remote sensors to monitor all sorts of processes, the demand for ways to power these rises as well. Nowadays, batteries are commonly used to power them. However, they deplete over time and must be replaced, which can be challenging when the sensor is placed somewhere hazardous or hard to reach. As vibrations are omnipresent, transducing the vibrational power into useful electric power can provide a suitable alternative [1].

In many cases, a dominant frequency is present in the vibration signal as demonstrated in Rantz and Roundy, allowing a tuned resonating mechanism to be a good solution to extract power from the signal [1]. However, this only works well at higher frequencies. At low frequencies (< 10 Hz), the driving motion amplitude rapidly increases for constant acceleration. As a resonator relies on amplifying the

input amplitude, the length of the vibration energy harvester (VEH) then rapidly grows to dimensions unsuitable for its intended applications.

Nevertheless, there are methods to keep the size of the VEH within bounds. Geisler *et al* [2] made a tubular electromagnetic energy harvester with an increased amount of electrical damping to allow larger input amplitudes from human motion. Smilek *et al* [3] used a rolling mass in a circular cavity and as such the proof mass has no displacement limit. Others use the principle of frequency up-conversion (FupC) where a low frequency oscillator induces an impulse response in a high frequency oscillator that generates the output. Halim *et al* [4] made a tubular electromagnetic FupC harvester and Galchev *et al* [5] produced a piezoelectric variant.

However, there is something that they all have in common: the largest dimension of the VEH is in the direction of the excitation. This makes sense as the output power scales quadratically with the internal displacement limit and linearly with the other dimensions [6]. Furthermore, electromagnetic transducers scale down poorly as shown in O'Donnell *et al* [7]. So a small length VEH excited at low frequency tends to perform poorly due to scaling issues. When a high efficiency, defined as the generator figure of merit (FoM_g) [8], is

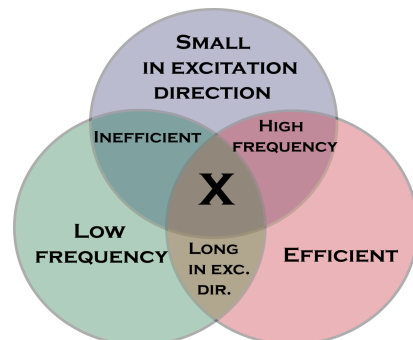


Fig. 1: Venn diagram representation of the problem of low frequency energy harvesting. Combining two juxtaposed characteristics will result in the opposite of the one left. The intersection of all three seems infeasible till now.

to be found at low frequency it will require a greater length of the VEH as seen in [9], [10], [11]. On the other hand, when a small length in excitation direction is needed in conjunction with high efficiency, the VEH tends to operate at higher frequencies as in [12].

The problem that arises due to this is summarized in Fig. 1. It shows that two characteristics can be picked, and their intersection results in the opposite of the characteristic that is left. The intersection of all three, an energy harvester small in excitation direction operating efficiently at low frequency with large inputs seems infeasible up till now.

The research objective of this work is to end up in the intersection of all three characteristics by taking a new approach for energy harvester design. A piezoelectric cantilever beam is brought close to a statically balanced condition, i.e. most of its stiffness is compensated through addition of negative stiffness counteracting the positive stiffness of the piezo. This negative stiffness can be introduced by buckled flexures, attracting or repelling magnets [13], [14]. In this work, attracting magnets are used. A piezoelectric beam is generally stiff at low frequencies and by compensating the stiffness, the required force to deform it becomes much lower. A piezo claims little space in the excitation direction and can therefore be a good candidate for ending up in the intersection of the three characteristics. A model will be developed throughout this work to predict the dynamics and voltage output, which will be validated experimentally.

The next sections are organized as follows: in section 2, two important parameters that are used to benchmark the harvester performance with respect to prior art are discussed. The design of the harvester is discussed along with the approach for modelling the voltage output. In section 3, the results from the simulation are compared to experimental results and are discussed in section 4 along with the performance of the harvester with respect to literature. Finally, the main conclusions are summarized in section 5.

2. Method

A. Motion ratio and generator figure of merit

Two parameters that are of major importance throughout this work are the motion ratio λ and the generator figure of merit FoM_g introduced in the work of Blad and Tolou [8]. These are defined

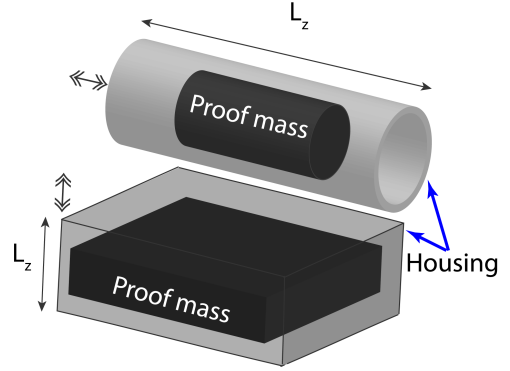


Fig. 2: Two harvester configurations of equal volume and proof mass. The upper is often found in literature as it is beneficial for power generation, the lower configuration is the focus of this work. Double arrows indicate excitation directions.

as:

$$\lambda = \frac{L_z}{2Y_0} \quad (1)$$

$$FoM_g = \frac{P_{RMS}}{\frac{1}{16}Y_0\rho_{pm}VL_z\omega^3} \cdot 100\% \quad (2)$$

Where L_z is the length of the VEH along the excitation direction, Y_0 is the input motion amplitude, P_{RMS} is the RMS output power, ρ_{pm} is the density of the proof mass, V is the package volume of the VEH and ω is the radial frequency corresponding to the driving motion.

The motion ratio is the ratio between the length of the VEH and the applied driving motion. In the ideal case where the frame claims no space, this length would be the displacement limit of the proof mass. It is a measure to determine to what extent the VEH can be used as a resonator. For instance, it can be used as a resonator when $\lambda > 1$ as in this case, resonant amplification of the input motion is possible. Hence, a resonator with a large Q -factor has a large motion ratio as well. When $\lambda \leq 1$, the input motion is larger than that of the proof mass and resonant amplification is not possible, resulting into a nonresonant device.

The generator figure of merit FoM_g is an improved version of the volume figure of merit FoM_v introduced in [6]. It uses the density of the proof mass and instead of using $V^{4/3}$, it uses VL_z as the power output is more dependent on L_z than the other directions [6]. This principle is shown in Fig. 2. The upper tubular configuration with larger L_z is often seen in literature due to its larger potential for power generation. The lower configuration with smaller L_z is the configuration that is focussed on in this work for obtaining a lower motion ratio. The FoM_g enables a fair performance comparison

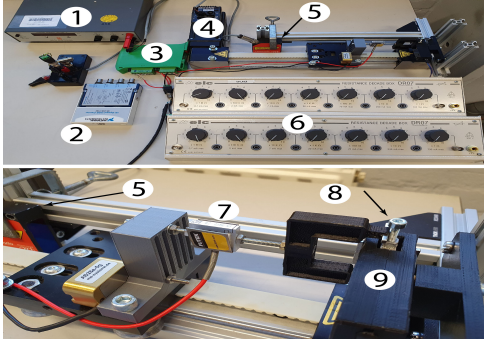


Fig. 3: Force-displacement test setup with (1) power supply, (2) DAQ, (3) signal amplifier, (4) stepper motor, (5) laser sensor, (6) resistance decade box, (7) load cell, (8) magnetic contact and (9) harvester.

between both configurations by removing the excitation length bias.

B. Force-displacement setup

For the design and modelling of the VEH, force-displacement measurements are necessary. The setup to measure these are shown in Fig. 3. The setup consists of a Moons' 24Q-3AG stepper motor connected to an Almotion LT50-TR-G8-200 linear stage. A Futek LSB200 sensor is used to measure the force followed by a SCAIME CPJ analog transmitter. The displacement is measured by a Micro-Epsilon optoNCDT1300 laser distance sensor and ELC DR07 resistance decade boxes are used to set the load resistance. The outputs are measured by an NI 9215 DAQ of which the data is analysed in MATLAB.

C. Mechanical design

To compensate the stiffness of the piezoelectric beam, attracting magnets have been chosen in the configuration shown in Fig. 4. Details on the specifications can be found in table I. By using attracting magnets in this setup, the introduced negative stiffness can be tuned best through adjusting the distance between the magnets. As can be seen from Fig. 4, the frame acts as an endstop to limit the motion of the proof mass. A few reasons for this are: (1) the strain needs to be limited as to not damage the piezo, (2) it prevents the proof mass magnet from clinging to the fixed magnets and (3) it is a mechanism to transfer momentum into the proof mass motion.

The VEH is designed to function around excitations of lower than 10 hz with input amplitudes that are such that the motion ratio is lower than one. Normally, to ensure that maximum power is extracted from the energy harvester, the load resistance is assessed by using the impedance matching

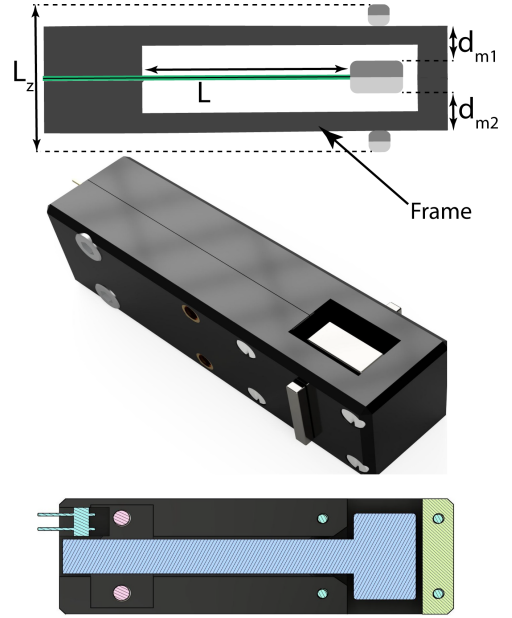


Fig. 4: Schematic diagram, render and lateral cross section of the energy harvester.

criterion as in [15]. It must be noted that the load must remain constant, as the load resistance will affect the stiffness due to the electromechanical coupling. Altering the load may result into an increase or decrease in the stiffness, which can be detrimental to the harvester performance. Therefore, a load of $1M\Omega$ is used and is kept constant.

In order to compensate the stiffness of the piezoelectric beam, its stiffness needs to be known. Therefore, a force-displacement measurement was taken to assess the stiffness at the uncompensated condition with a load of $1M\Omega$ connected. This measurement can be seen in Fig. 8a. Then, a COMSOL Multiphysics electromagnetic simulation was carried out to find the distances d_{m1} and d_{m2} between the proof mass magnet and fixed magnets to provide an appropriate negative stiffness. The proof mass magnet was displaced inbetween the fixed magnets by a parametric sweep and the force was evaluated, resulting in a force-displacement relation. A parametric sweep was applied on d_{m1} , d_{m2} and the proof mass displacement to find the negative stiffness that fits best to the positive stiffness of the beam. The stiffness has been verified with the setup from Fig. 3. This results are shown in Fig. 8a.

D. Fabrication

The piezoelectric beam used in the energy harvester is a Morgan Ceramics PZT-508 of 46x6x0.76 mm.

TABLE I: Specifications of the energy harvester.

Parameter	Symbol	Value	Parameter	Symbol	Value
Clamped length	L	32 mm	Damping ratio	ζ_1	0.021
Beam width	b	6 mm	Tip magnet size	-	15x10x5 mm
Substrate thickness	h_s	0.37 mm	Fixed magnet size	-	15x2x1.8 mm
Piezo thickness	h_p	0.19 mm	Magnet spacing 1,2	$d_{m1,2}$	5.65/5.82 mm
Capacitance single layer	C	36.22 nF	Tip magnet flux density	B_T	1.17 T
Relative permittivity	ϵ_{r33}^T	3900	Fixed magnet flux density	B_F	1.08 T
Charge constant	d_{31}	-315 pC/N	VEH package volume	V	60x20x20 mm ³
Piezoelectric constant	e_{31}^E	-19.2 N/Vm	Tip mass	M_t	6.5 g
Elasticity Piezo	c_{11}^E	61 GPa	Tip inertia	I_t	0.0677 kg · mm ²
Elasticity Substrate	Y_s	200 GPa	Endstop stiffness	K_{stop}	250 kN/m
Mass per beam length	m	0.0217 g/mm	Endstop damping	C_{stop}	15 Ns/m
Endstop position	w_s	1.5 mm	Length in excitation direction	L_z	20 mm

An N35 Neodymium block magnet has been fixed to its tip with epoxy glue to form a proof mass. The frame of the VEH is printed with 100% infill in PLA. As the stiffness compensation becomes increasingly delicate as the total stiffness approaches zero and to account for printing tolerances, the frame was printed a few tens of millimeters larger in the L_z direction. It was then manually sanded down and iteratively tested for neutral stability.

E. Model

To model the dynamics and voltage output of the stiffness compensated piezo, a distributed parameter model is preferred over a lumped parameter model as an accurate description of the strain distribution is necessary. Furthermore, it was shown that the distributed parameter model from [16] could be used to provide corrections to a lumped model [17]. The main question is what this strain distribution looks like. One could reason that if no stiffness is reduced, modal analysis is suitable if resonance occurs. On the other hand, if the stiffness is fully removed, it could be reasoned that the deflection pattern can be described by the static deflection pattern of a cantilever beam multiplied by some temporal forcing function:

$$\delta(t) = \left(\frac{Px^2(3L-x)}{6YI} + \frac{Mx^2}{2YI} \right) f(t) \quad (3)$$

Where δ is the tip deflection, P the tip load, L the beam length, x the beam length coordinate, YI the bending stiffness, M the tip moment and f the temporal forcing function. The eigenfunction from modal analysis and the static deflection pattern form the bounds where the real deflection pattern should be in. To compare them, they are plotted Fig. 5 along with their second derivatives which are related to strain. All functions have been normalized.

The figure shows that the deflections are very similar and that the strain diverges with the beam length. However, near the clamping the largest

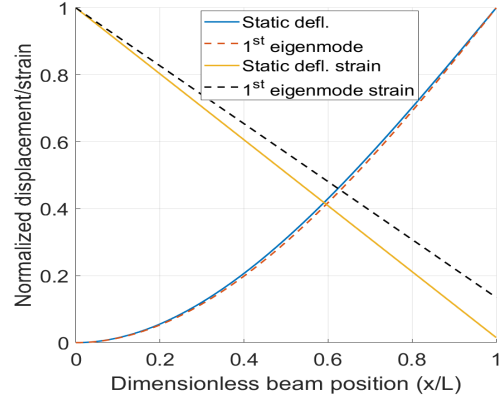


Fig. 5: Normalized deflection and strain for static deflection pattern and first eigenmode.

strain can be found and here the error is minimal. It can therefore be assumed modal analysis can be a representative method for modelling.

The modelling approach is as follows. First, modal analysis is used for the case of a cantilever beam. Next, the endstops are included in the equations and then the negative stiffness is added. Finally, the force-displacement data of the compensated beam is added to the equations. This last step makes sure that the remanent stiffness and hysteresis are included in the model. These steps will be discussed next.

1) *Modal analysis*: Since many energy harvesters operate at a certain resonance frequency to deliver peak power, it is useful to use modal analysis as this is centered around that certain resonance frequency. The distributed parameter model of Erturk and Inman [16], [18] utilized this principle. In their work, they had found closed-form solutions for the output voltage. However, these are based on the Laplace transform and are not suited when nonlinear terms from the endstops and hysteresis are introduced. Therefore, in this work the coupled equations in

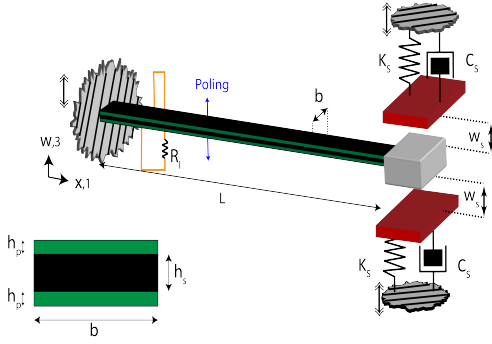


Fig. 6: Schematic diagram of the in series connected piezo. The red plates form the endstop contact surface, the lower left shows the cross-section of the piezo. Hashed platforms denote the vibrating world.

modal coordinates for an in series connected piezo are used and will be solved numerically. Their derivation is concisely shown. The nomenclature is kept the same for easy reference. In Fig. 6, a schematic diagram of the piezo is shown. To transform the deflection w to modal coordinates the following infinite series is used:

$$w(x, t) = \sum_r^{\infty} \phi_r(x) \eta_r(t) \quad (4)$$

Here, $\phi_r(x)$ is the mass-normalized eigenfunction corresponding to eigenmode r and $\eta_r(t)$ is the temporal response corresponding to that same mode. The eigenfunction is defined as:

$$\phi_r(x) = C_r \left[\cos \frac{\lambda_r}{L} x - \cosh \frac{\lambda_r}{L} x + \varsigma_r \left(\sin \frac{\lambda_r}{L} x - \sinh \frac{\lambda_r}{L} x \right) \right] \quad (5)$$

where

$$\varsigma_r = \frac{\sin \lambda_r - \sinh \lambda_r + \lambda_r \frac{M_t}{mL} (\cos \lambda_r - \cosh \lambda_r)}{\cos \lambda_r + \cosh \lambda_r - \lambda_r \frac{M_t}{mL} (\sin \lambda_r - \sinh \lambda_r)} \quad (6)$$

The modal eigenvalue λ_r is found by solving the characteristic equation:

$$1 + \cos \lambda_r \cosh \lambda_r + \frac{\lambda_r M_t}{mL} (\cos \lambda_r \sinh \lambda_r - \sin \lambda_r \cosh \lambda_r) - \frac{\lambda_r^3 I_t}{mL^3} (\cosh \lambda_r \sin \lambda_r + \sinh \lambda_r \cos \lambda_r) + \frac{\lambda_r^4 M_t I_t}{m^2 L^4} (1 - \cos \lambda_r \cosh \lambda_r) = 0 \quad (7)$$

Where M_t , m , L and I_t are the tip mass, beam mass per length, clamped beam length and tip inertia, respectively. To find the amplitude C_r , the

eigenfunction is normalized by the orthogonality condition:

$$\int_0^L \phi_r(x) m \phi_s(x) dx + \phi_r(L) M_t \phi_s(L) + \left[\frac{d\phi_r(x)}{dx} I_t \frac{d\phi_s(x)}{dx} \right]_{x=L} = \delta_{rs} \quad (8)$$

The bending stiffness is defined as:

$$YI = \frac{2b}{3} \left(Y_s \frac{h_s^3}{8} + c_{11}^E \left((h_p + \frac{h_s}{2})^3 - \frac{h_s^3}{8} \right) \right) \quad (9)$$

Where b , Y_s , c_{11}^E , h_p and h_s are the beam width, Young's moduli and layer thicknesses of the substrate and piezo layer, respectively. Using the bending stiffness, the eigenfrequency can be found as:

$$\omega_r = \lambda_r^2 \sqrt{\frac{YI}{mL^4}} \quad (10)$$

The coupled beam and electric circuit equations confined to the first mode in modal coordinates are as follows:

$$\frac{d^2 \eta_1(t)}{dt^2} + 2\zeta_1 \omega_1 \frac{d\eta_1(t)}{dt} + \omega_1^2 \eta_1(t) + \theta \frac{d\phi_1(x)}{dx} \bigg|_{x=L} V(t) = F_1(t) \quad (11)$$

$$\frac{C_p}{2} \frac{dV(t)}{dt} + \frac{V(t)}{R_l} = -e_{31} b \frac{h_p + h_s}{2} \frac{d\phi_1(x)}{dx} \bigg|_{x=L} \frac{d\eta_1(t)}{dt} \quad (12)$$

where the forcing term $F_1(t)$ and electromechanical coupling θ are equal to:

$$F_1(t) = -Y_0 \omega^2 \sin \omega t \left(m \int_0^L \phi_1(x) dx + M_t \phi_1(L) \right) \quad (13)$$

$$\theta = \frac{e_{31} b}{2} \left(\frac{h_s^2}{4} - (h_p + \frac{h_s}{2})^2 \right) \quad (14)$$

Where ζ_1 , V , C_p , R_l , e_{31} , Y_0 and ω are the damping ratio, output voltage, single layer capacitance, load resistance, piezoelectric constant, driving motion amplitude and driving motion radial frequency. Most parameters can be found in table I. The details on the derivation of these equations can be found in [16], [18].

2) *Endstops*: The endstops are defined as an additional spring and damper placed in parallel [19]. Fig. 6 shows a schematic interpretation of the endstop. The force encountered by endstop contact can be described as:

$$F^s(w) = \begin{cases} K_s(w - w_s) + C_s\dot{w} & \text{if } w \geq w_s \\ 0 & \text{if } |w| < w_s \\ K_s(w + w_s) + C_s\dot{w} & \text{if } w \leq -w_s \end{cases} \quad (15)$$

Here F^s is the endstop force, K_s the endstop stiffness, w_s is the amplitude after which the stopper is hit and C_s is the endstop damping. The endstop stiffness K_s is found by Hertz contact mechanics. As Hertz contact stiffness behaves nonlinearly with indentation, its stiffness value was raised until its corresponding indentation matched the indentation in the final simulations. The endstop damping was assessed experimentally by a shaker test at 16 hz and 2 g. By measuring the tip mass displacement and velocity with laser sensors, the coefficient of restitution was found, which can be translated to the endstop damping [19].

3) *Negative stiffness*: To add negative stiffness, the negative stiffness from the finite element simulation or the measurement could be used. However, as indicated, the next step is to include the hysteresis force-displacement measurement at the compensated state. The remanent stiffness is also present in this measurement. As a result, this remanent stiffness would then be present twice in the model. Therefore, it is chosen to numerically add a negative stiffness that fully compensates the positive stiffness through addition of a tip deflection force:

$$F^N = \frac{3YI}{L^3}w(L) \quad (16)$$

By fully removing the stiffness and using the remanent stiffness present in the force-displacement measurement of the compensated beam, an accurate description of the stiffness can be obtained.

4) *Hysteresis*: As the stiffness has been fully erased in the model to provide a "clean slate", the remanent bending stiffness and the hysteresis are to be found. These are found by quasistatically measuring the force-displacement of the compensated beam with the setup in Fig. 3. In Fig. 8b the measured hysteresis is shown in a force-displacement diagram and is named F^H . The data has been filtered with a Savitzky-Golay filter and has been fitted with a cubic interpolant in order to implement it into the model. The time period to

move from one peak displacement to the other and back is equal to 11.7 s. The measurement is taken for a connected load resistance of $1M\Omega$.

The implementation of the force-displacement data is as follows: at peak displacement, one of the endstops is hit. This hit is detected as an event in the MATLAB ODE-solver. After the hit, the hysteretic force switches from curve, e.g. the left endstop is approached from the red curve and the force switches to the blue curve afterwards and stays on it until the right endstop is hit. A smaller loop is shown as well in Fig. 8b in black and green. This is for the a specific case when no peak-peak motion is obtained and the proof mass bounces from one endstop only. This case will also be validated.

5) *Integration in the modal equations*: As the descriptions of the endstops, the negative stiffness and the force-displacement have been found, they can be integrated into the coupled modal beam equation 11. The resulting equation is found by eq. 17. Note that the added terms are premultiplied by $\phi_1(L)^2$. This is because the terms have to be converted to modal coordinates given by eqn. 4 and are premultiplied by the mode shape through mode shape orthogonality. The equations of motion are thus formed by eqns. 12, 13 and 17.

$$\begin{aligned} \frac{d^2\eta_1(t)}{dt^2} + 2\zeta_1\omega_1 \frac{d\eta_1(t)}{dt} + \omega_1^2\eta_1(t) + \theta \frac{d\phi_1(x)}{dx} \Big|_{x=L} V(t) \\ + \phi_1(L)^2 F^S(\eta_1(t)) - \phi_1(L)^2 \frac{3YI}{L^3} \eta_1(t) + \\ \phi_1(L)^2 F^H(\eta_1(t)) = F_1(t) \end{aligned} \quad (17)$$

There is one thing that must be noted by taking this approach. As pointed out in Erturk and Inman [20], in a clamped-free beam, no tip force may be present at the free tip as this is one of the boundary conditions. In this model, the first vibration mode shape of the clamped-free condition is used and the added negative stiffness acting as a tip force theoretically violates the boundary condition. However, for now it is assumed that the mode shape will not differ that much and that it may be negligible for the output, more about this in section 4. An improvement would be to include the negative stiffness in the tip boundary condition when solving for the mode shape function $\phi_1(x)$.

F. Harvester excitation setup

In order to validate the model, a custom air bearing stage with a linear motor is used to excite the energy harvester at low frequencies and large amplitudes. The setup that is used is shown in

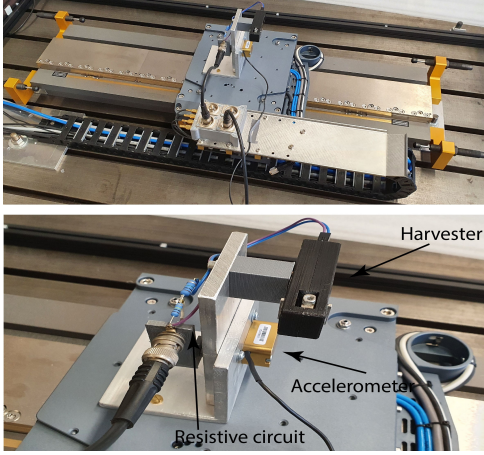


Fig. 7: Linear motion stage to excite the energy harvester at low frequency with large amplitudes.

Fig. 7. An ME-systeme AS28e accelerometer is used to record the applied acceleration and an NI cDAQ-9174 with NI-9263 and NI-9215 modules is used to create input signals and record the output, respectively. A resistive divider is used to lower the voltage from the piezo to the NI-9215.

G. Measurement procedure

In order to assess how accurately the simulation can predict the performance of the VEH, the RMS power frequency response is measured. In order to do so, a sinusoidal excitation is applied at an acceleration between 1.5 and 3 g and frequency between 2 and 10 Hz. The measurement is not really taken as a sweep: at every single frequency, the measurement is started from zero initial conditions.

H. Benchmarking with respect to prior art

In order to benchmark the performance of the VEH in this work, it is compared to prior art found in literature. This is done by plotting the $\lambda - FoM_g$ space. This approach was also taken in [8], where a comprehensive comparison of VEH performance for different classes of VEHs was carried out. It must be noted that literature falls short on reporting all the variables needed to calculate the motion ratio λ and FoM_g . In some cases however, the necessary parameters could be derived from other parameters or be estimated. For instance, in the case of a resonating cantilever, the size of the proof mass and the Q -factor are used to find L_z .

3. Results

In Fig. 8 the force-displacement measurements are shown. Fig. 8a shows the force-displacement of the unbalanced beam with a $1M\Omega$ load connected along

with the simulated and validated negative stiffness. Fig. 8b shows the force-displacement measurements for the compensated state of the VEH. A large loop is shown that indicates peak-peak motion and a smaller loop as well for smaller motions. In Fig. 9 the simulated displacement and voltage along with the measured voltage is shown at the condition of 4 Hz and 1.5/3 g. Fig. 9d shows the RMS power frequency response. This is done at a constant sinusoidal acceleration between 1.5 and 3 g and between 2 and 10 Hz. The simulation is compared to the measurements in terms of RMS output power at 2.5 and 3 g. The performance of the energy harvester in terms of motion ratio λ and FoM_g is depicted in Fig. 10 and is compared to prior art from literature. Here, two classes can be seen, single degree-of-freedom (SDoF) and frequency-upconverters (FupC).

4. Discussion

A. Time domain

The results in Figs. 9a, 9b are typical throughout the frequency response. The blue line in Fig. 9a shows that both endstops are hit, which is the case for all measurements at 2.5 and 3 g. In this case, the measurements match the simulations best, as the used hysteresis loop is also based on full peak-peak motion. Figs. 9a, 9c show what happens if no peak-peak motion is obtained, e.g. at 1.5 g. From the displacement in Fig. 9a it is seen that the proof mass detaches from the lower endstop and remains within negative displacement. Then if the simulation is used with a full peak-peak hysteresis loop, it greatly overestimates the output voltage as shown in Fig. 9c.

To improve the simulation performance for this specific case, a hysteresis loop should be used that is representative for the lower displacement. This measured loop is shown in Fig. 8b. Using this smaller loop as input for the simulation, it is seen that the voltage is resembled more closely. The consequences of this are however severe: for every separate non-peak-peak motion, a separate hysteresis loop is necessary in order to predict the output within acceptable accuracy. In [21] it was demonstrated for piezoelectric actuators that inner hysteresis loops could be predicted by using fitting curves to the outer loops. Unpublished work of the authors has confirmed this to work for force-displacement as well. This can be a good starting point to model non-peak-peak motion.

B. Frequency response

The RMS power frequency response is shown in Fig. 9d. The frequency response was measured at

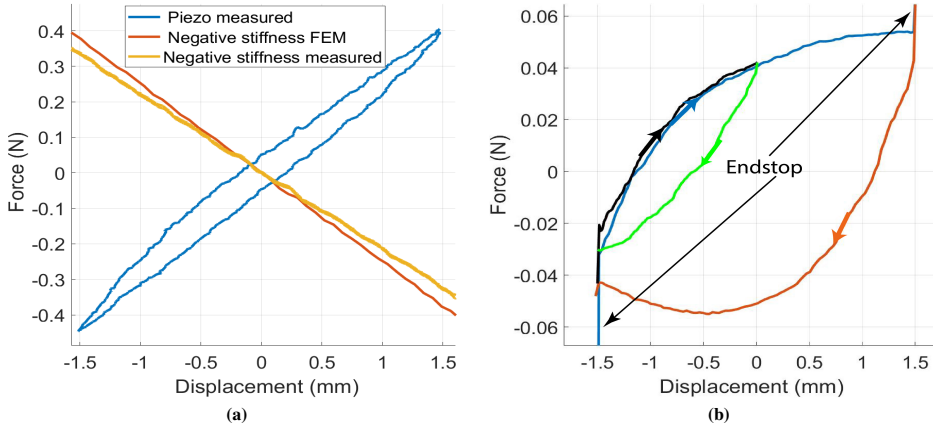


Fig. 8: Force-displacement diagrams with (a) measured force-displacement of the uncompensated beam and negative stiffness result from finite element simulation, (b) measured hysteresis paths for the compensated beam with a load resistance of $1M\Omega$. The time period equals 11.7 s.

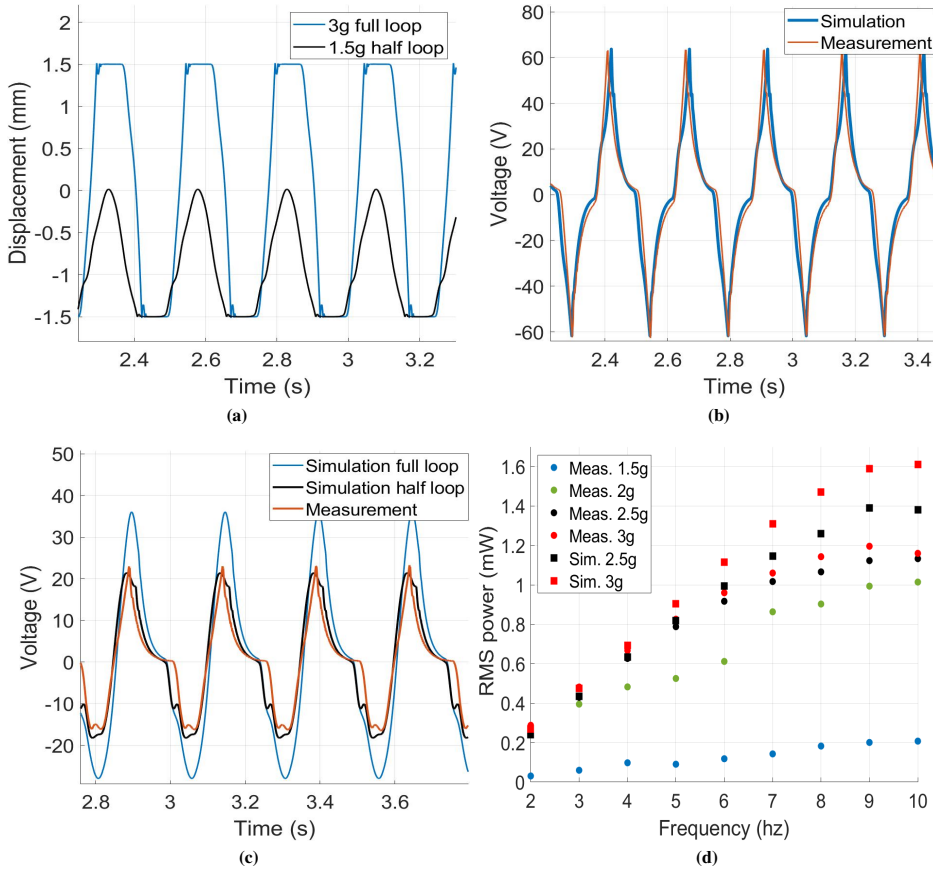


Fig. 9: Harvester performance at 4 Hz with in (a) simulated displacements, (b) simulated and measured voltage at 3 g and (c) simulated and measured performance at 1.5 g. Figure (d) shows the RMS power frequency response at constant acceleration. Dots indicate measured data, squares simulated data.

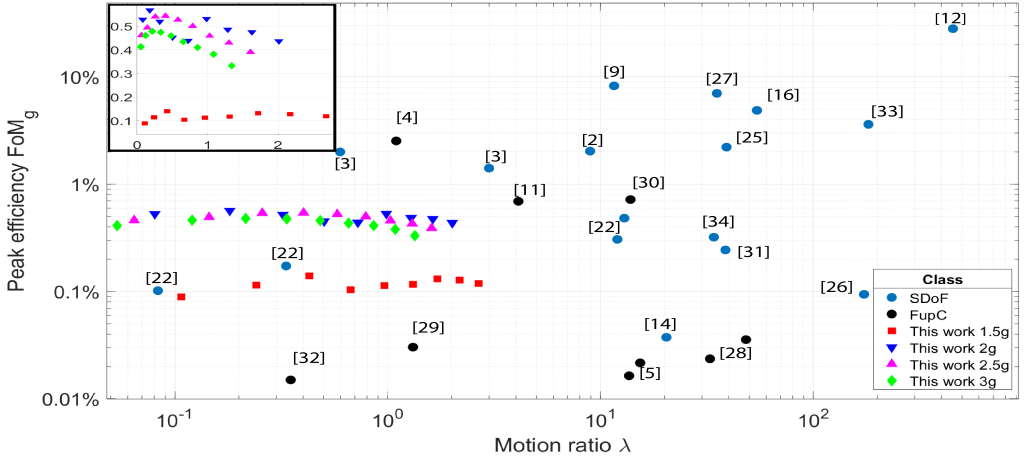


Fig. 10: Generator figure of merit (FoM_g) performance comparison of the energy harvester in this work to prior art as a function of motion ratio. SDoF stands for single degree-of-freedom, FupC for frequency-upconverter. The zoom view in the top left shows the performance of this work in linear scale.

1.5, 2, 2.5 and 3 g yet only for 2.5 and 3 g it is compared to the simulations due to the problems discussed previously. The peak performance is found at 9 Hz and 3 g where an RMS power of 1.20 mW is delivered.

The effect of increased input acceleration is also very clear. At 1.5g only one endstop is hit, resulting in a low linear response. This makes sense as the output voltage depends on the strain rate integrated over the beam length, which is lower in this case [16]. At 2 g, the second endstop is hit slightly at some frequencies and at others it is not, resulting in a larger scatter in power. At 2.5 and 3 g both endstops are hit. These curves show an interesting behaviour. First, the response is linear until 6 Hz. This is also seen in other nonresonant devices such as in [22]. After 6 Hz, the response continues in a sublinear trend and a power saturation seems to appear.

The simulated output power response at 2.5 and 3 g is also shown in Fig. 9d. It can be seen that at frequencies lower than 6 Hz, the simulated power closely predicts the measured. The error remains below 10%. However, from 7 Hz and onwards, the simulation rapidly diverges from the measurement and overestimates. The simulated voltage starts to increase, resulting in a rapid increase in RMS power. The results suggest that the exclusion of the negative stiffness in the mode shape function $\phi_r(x)$ is admissible; the difference in power is small at frequencies lower than 6 Hz. If the mode shape function were not representative, a larger error should be seen for all frequencies, as in the simulation the deflection pattern remains constant for all frequencies.

The exact reason behind the rapid error growth is not fully understood yet. A possible explanation could be that the hysteresis loop measured at quasistatic condition starts to become less representative at higher frequencies. Hysteresis loops in piezoelectric actuators show a rate dependence [23], [24] and unpublished work of the authors has confirmed this effect to be seen in force-displacement measurements as well. Therefore, additional terms may be necessary in the equations of motion which is a subject for future work.

C. Performance comparison to prior art

In Fig. 10, the measured performance of the energy harvester is compared to prior art in terms of FoM_g and λ . From the plot it can be noted that prior art is inclined to larger motion ratios. The FupC harvesters tend to be less efficient than SDoF. To the author's best knowledge, this work has the highest FoM_g for a motion ratio under 0.6. The FoM_g peaks at 0.567% at a motion ratio of 0.18. Although this is still low, larger values can be expected as no optimization has been applied yet.

Several things can be noted from the performance belonging to this work. First, the FoM_g is relatively constant throughout λ at constant acceleration. For instance, at 2.5 g a factor of 25 can be found in λ but only a factor of 1.38 in FoM_g . To put this in perspective, resonating VEHs without endstops were analysed in [8] and showed a factor 16 in λ and 344 in FoM_g . This clearly demonstrates the operational differences between resonant and nonresonant devices.

From the zoom view in Fig. 10, it is seen that the peak FoM_g does not correspond to the peak power

or peak acceleration. The peak FoM_g is found at a motion ratio of 0.18 which corresponds to a frequency of 3 Hz and acceleration of 2 g. So although a higher frequency or input acceleration results into more output power, this clearly does not benefit the efficiency. This implies that after a certain value for the acceleration or input frequency, although the output power increases, the FoM_g does not. Hence, there is a certain threshold after which the VEH starts making less practical use of its physical dimensions and properties.

5. Conclusion

In this work, the stiffness of a piezoelectric vibration energy harvester is compensated through addition of attracting magnets. It was conceived in order to provide an energy harvester that has a small length in the excitation direction, that operates at low frequency with large inputs and that is efficient. A distributed parameter model from literature based on modal analysis was further extended by the addition of endstops, negative stiffness and hysteretic force-displacement data. For peak-peak displacements, the RMS power difference between simulation and measurement has been analysed. Between 2 and 6 Hz, the error between simulation and measurement remained below 10%, yet it rapidly grows when the frequency is further increased until 10 Hz. Therefore, a modal analysis based distributed parameter model can be found to be promising for modeling the dynamics and output of a cantilever-based stiffness compensated piezoelectric beam. However, work is necessary to improve the simulation performance over a wider range of frequencies.

The measured RMS peak power was obtained at 9 Hz and 3 g and was equal to 1.20 mW. When it comes to performance in terms of generator figure of merit (FoM_g), a peak value of 0.567% was obtained. To the author's knowledge, the efficiency is the largest reported in literature for the case of excitations below 6 Hz and larger than 2 g. No optimization has been applied until now, so even larger values can be expected.

REFERENCES

- [1] R. Rantzi and S. Roundy, "Characterization of Real-world Vibration Sources and Application to Nonlinear Vibration Energy Harvesters," *Energy Harvest. Syst.*, vol. 4, no. 2, pp. 67–76, Aug. 2019. [Online]. Available: <http://www.degruyter.com/view/j/ehs.2017.4.issue-2/ehs-2016-0021/ehs-2016-0021.xml>
- [2] M. Geisler, S. Boisseau, M. Perez, P. Gasnier, J. Willemin, I. Ait-Ali, and S. Perraud, "Human-motion energy harvester for autonomous body area sensors," *Smart Mater. Struct.*, vol. 26, no. 3, p. 035028, 2017. [Online]. Available: <http://stacks.iop.org/0964-1726/26/i=3/a=035028>
- [3] J. Smilek, Z. Hadas, J. Vetiska, and S. Beeby, "Rolling mass energy harvester for very low frequency of input vibrations," *Mechanical Systems and Signal Processing*, vol. 125, pp. 215–228, Jun. 2019. [Online]. Available: <http://www.sciencedirect.com/science/article/pii/S0888327018303194>
- [4] M. A. Halim, H. Cho, and J. Y. Park, "Design and experiment of a human-limb driven, frequency up-converted electromagnetic energy harvester," *Energy Conversion and Management*, vol. 106, pp. 393–404, Dec. 2015. [Online]. Available: <http://www.sciencedirect.com/science/article/pii/S0196890415009103>
- [5] T. Galchev, E. E. Aktakka, and K. Najafi, "A Piezoelectric Parametric Frequency Increased Generator for Harvesting Low-Frequency Vibrations," *J. Microelectromechanical Syst.*, vol. 21, no. 6, pp. 1311–1320, Dec. 2012.
- [6] P. D. Mitcheson, E. M. Yeatman, G. K. Rao, A. S. Holmes, and T. C. Green, "Energy Harvesting From Human and Machine Motion for Wireless Electronic Devices," *Proc. IEEE*, vol. 96, no. 9, pp. 1457–1486, Sep. 2008.
- [7] T. O'Donnell, C. Saha, S. Beeby, and J. Tudor, "Scaling effects for electromagnetic vibrational power generators," *Microsyst. Technol.*, vol. 13, no. 11, pp. 1637–1645, Jul. 2007. [Online]. Available: <https://doi.org/10.1007/s00542-006-0363-0>
- [8] T. W. Blad and N. Tolou, "On the efficiency of energy harvesters: A classification of dynamics in miniaturized generators under low-frequency excitation," *Journal of Intelligent Material Systems and Structures*, vol. 30, no. 16, pp. 2436–2446, Sep. 2019. [Online]. Available: <https://doi.org/10.1177/1045389X19862621>
- [9] A. Munaz, B.-C. Lee, and G.-S. Chung, "A study of an electromagnetic energy harvester using multi-pole magnet," *Sens. Actuators Phys.*, vol. 201, pp. 134–140, Oct. 2013. [Online]. Available: <http://linkinghub.elsevier.com/retrieve/pii/S0924242713003191>
- [10] C. Li, S. Wu, P. C. K. Luk, M. Gu, and Z. Jiao, "Enhanced Bandwidth Nonlinear Resonance Electromagnetic Human Motion Energy Harvester Using Magnetic Springs and Ferrofluid," *IEEE/ASME Trans. Mechatron.*, vol. 24, no. 2, pp. 710–717, Apr. 2019.
- [11] P. Pillatsch, E. M. Yeatman, and A. S. Holmes, "A scalable piezoelectric impulse-excited energy harvester for human body excitation," *Smart Mater. Struct.*, vol. 21, no. 11, p. 115018, Oct. 2012. [Online]. Available: <https://doi.org/10.1088%2F0964-1726%2F21%2F11%2F115018>
- [12] S. P. Beeby, R. N. Torah, M. J. Tudor, P. Glynne-Jones, T. O'Donnell, C. R. Saha, and S. Roy, "A micro electromagnetic generator for vibration energy harvesting," *J. Micromech. Microeng.*, vol. 17, no. 7, pp. 1257–1265, Jun. 2007. [Online]. Available: <https://doi.org/10.1088%2F0960-1317%2F17%2F7%2F07>
- [13] A. J. Lamers, J. A. Gallego Sánchez, and J. L. Herder, "Design of a statically balanced fully compliant grasper," *Mechanism and Machine Theory*, vol. 92, pp. 230–239, Oct. 2015. [Online]. Available: <http://www.sciencedirect.com/science/article/pii/S0094114X15001342>
- [14] S. C. Stanton, C. C. McGehee, and B. P. Mann, "Nonlinear dynamics for broadband energy harvesting: Investigation of a bistable piezoelectric inertial generator," *Physica D: Nonlinear Phenomena*, vol. 239, no. 10, pp. 640–653, May 2010. [Online]. Available: <http://www.sciencedirect.com/science/article/pii/S0167278910000394>
- [15] V. R. Challa, M. G. Prasad, Y. Shi, and F. T. Fisher, "A vibration energy harvesting device with bidirectional resonance frequency tunability," *Smart Mater. Struct.*, vol. 17, no. 1, p. 015035, Jan. 2008. [Online]. Available: <https://doi.org/10.1088%2F0964-1726%2F17%2F01%2F015035>
- [16] A. Erturk and D. J. Inman, "An experimentally validated bimorph cantilever model for piezoelectric energy harvesting from base excitations," *Smart Mater. Struct.*, vol. 18, no. 2, p. 025009, Feb. 2009. [Online]. Available: <https://iopscience.iop.org/article/10.1088/0964-1726/18/2/025009>
- [17] D. J. Inman and S. Priya, *Energy Harvesting Technologies*, 1st ed. New York: Springer, 2009. [Online]. Available: DOI10.1007/978-0-387-76464-1

- [18] D. J. Inman and A. Erturk, *Piezoelectric Energy Harvesting*, 1st ed. Chichester: John Wiley & Sons, 2011.
- [19] D. Zhao and Y. Liu, "Improved Damping Constant of Hertz-Damp Model for Pounding between Structures," *Mathematical Problems in Engineering*, vol. 2016, pp. 1–7, 2016. [Online]. Available: <http://www.hindawi.com/journals/mpe/2016/9161789/>
- [20] A. Erturk and D. J. Inman, "Issues in mathematical modeling of piezoelectric energy harvesters," *Smart Mater. Struct.*, vol. 17, no. 6, p. 065016, Dec. 2008. [Online]. Available: <http://stacks.iop.org/0964-1726/17/i=6/a=065016?key=crossref.2c9ea418f2ce70369a621285b33432a8>
- [21] S. Bashash and N. Jalili, "Underlying memory-dominant nature of hysteresis in piezoelectric materials," *Journal of Applied Physics*, vol. 100, no. 1, p. 014103, Jul. 2006. [Online]. Available: <https://aip-scitation-org.tudelft.idm.oclc.org/doi/full/10.1063/1.2208805>
- [22] Y. Wang, Q. Zhang, L. Zhao, and E. S. Kim, "Non-Resonant Electromagnetic Broad-Band Vibration-Energy Harvester Based on Self-Assembled Ferrofluid Liquid Bearing," *J. Microelectromechanical Syst.*, vol. 26, no. 4, pp. 809–819, Aug. 2017.
- [23] M. A. Janaideh, C.-Y. Su, and S. Rakheja, "Development of the rate-dependent Prandtl-Ishlinskii model for smart actuators," *Smart Mater. Struct.*, vol. 17, no. 3, p. 035026, Apr. 2008. [Online]. Available: <https://doi.org/10.1088%2F0964-1726%2F17%2F3%2F035026>
- [24] M.-J. Yang, C.-X. Li, G.-Y. Gu, and L.-M. Zhu, "A Modified Prandtl-Ishlinskii Model for Rate-dependent Hysteresis Nonlinearity Using nth-power Velocity Damping Mechanism," *International Journal of Advanced Robotic Systems*, vol. 11, no. 10, p. 163, Oct. 2014. [Online]. Available: <https://doi.org/10.5772/58984>
- [25] K. Ashraf, M. H. M. Khir, J. O. Dennis, and Z. Baharudin, "A wideband, frequency up-converting bounded vibration energy harvester for a low-frequency environment," *Smart Mater. Struct.*, vol. 22, no. 2, p. 025018, Jan. 2013. [Online]. Available: <https://doi.org/10.1088%2F0964-1726%2F22%2F2%2F025018>
- [26] D. F. Berdy, P. Srisingsitthisunti, X. Xu, J. Rhoads, B. Jung, and D. Peroulis, "Compact low frequency meandered piezoelectric energy harvester," *Proc. PowerMEMS*, p. 4, 2009.
- [27] D. F. Berdy, D. J. Valentino, and D. Peroulis, "Design and optimization of a magnetically sprung block magnet vibration energy harvester," *Sensors and Actuators A: Physical*, vol. 218, pp. 69–79, Oct. 2014. [Online]. Available: <http://www.sciencedirect.com/science/article/pii/S0924424714003069>
- [28] T. Galchev, H. Kim, and K. Najafi, "Micro Power Generator for Harvesting Low-Frequency and Nonperiodic Vibrations," *J. Microelectromechanical Syst.*, vol. 20, no. 4, pp. 852–866, Aug. 2011.
- [29] M. Halim and J. Park, "Modeling and experiment of a handy motion driven, frequency up-converting electromagnetic energy harvester using transverse impact by spherical ball," *Sensors and Actuators A: Physical*, vol. 229, pp. 50–58, Jun. 2015. [Online]. Available: <http://www.sciencedirect.com/science/article/pii/S0924424715001478>
- [30] A. Nammari, L. Caskey, J. Negrete, and H. Bardaweel, "Fabrication and characterization of non-resonant magneto-mechanical low-frequency vibration energy harvester," *Mechanical Systems and Signal Processing*, vol. 102, pp. 298–311, Mar. 2018. [Online]. Available: <http://www.sciencedirect.com/science/article/pii/S0888327017305198>
- [31] J. Park and M. A. Halim, "Theoretical modeling and analysis of mechanical impact driven and frequency up-converted piezoelectric energy harvester for low-frequency and wide-bandwidth operation," *Sensors and Actuators A: Physical*, vol. 208, pp. 56–65, Feb. 2014. [Online]. Available: <http://www.sciencedirect.com/science/article/pii/S0924424713006316>
- [32] M. Renaud, P. Fiorini, R. van Schaijk, and C. van Hoof, "Harvesting energy from the motion of human limbs: The design and analysis of an impact-based piezoelectric generator," *Smart Mater. Struct.*, vol. 18, no. 3, p. 035001, Jan. 2009. [Online]. Available: <https://doi.org/10.1088/0964-1726/18/3/035001>
- [33] C. R. Saha, T. O'Donnell, N. Wang, and P. McCloskey, "Electromagnetic generator for harvesting energy from human motion," *Sensors and Actuators A: Physical*, vol. 147, no. 1, pp. 248–253, Sep. 2008. [Online]. Available: <http://www.sciencedirect.com/science/article/pii/S0924424708001398>
- [34] M. Salauddin, M. A. Halim, and J. Y. Park, "A magnetic-spring-based, low-frequency-vibration energy harvester comprising a dual Halbach array," *Smart Mater. Struct.*, vol. 25, no. 9, p. 095017, 2016. [Online]. Available: <http://stacks.iop.org/0964-1726/25/i=9/a=095017>

7

REFLECTION, CONCLUSIONS AND RECOMMENDATIONS

This chapter provides an overview of all activities throughout this research. The entire process is being reflected upon and the most important conclusions are drawn. Furthermore, some future research recommendations are listed.

7.1. PROJECT OVERVIEW

To get a clear overview of the entire process of this thesis, the main research activities and their relations are shown in an overview in figure 7.1.

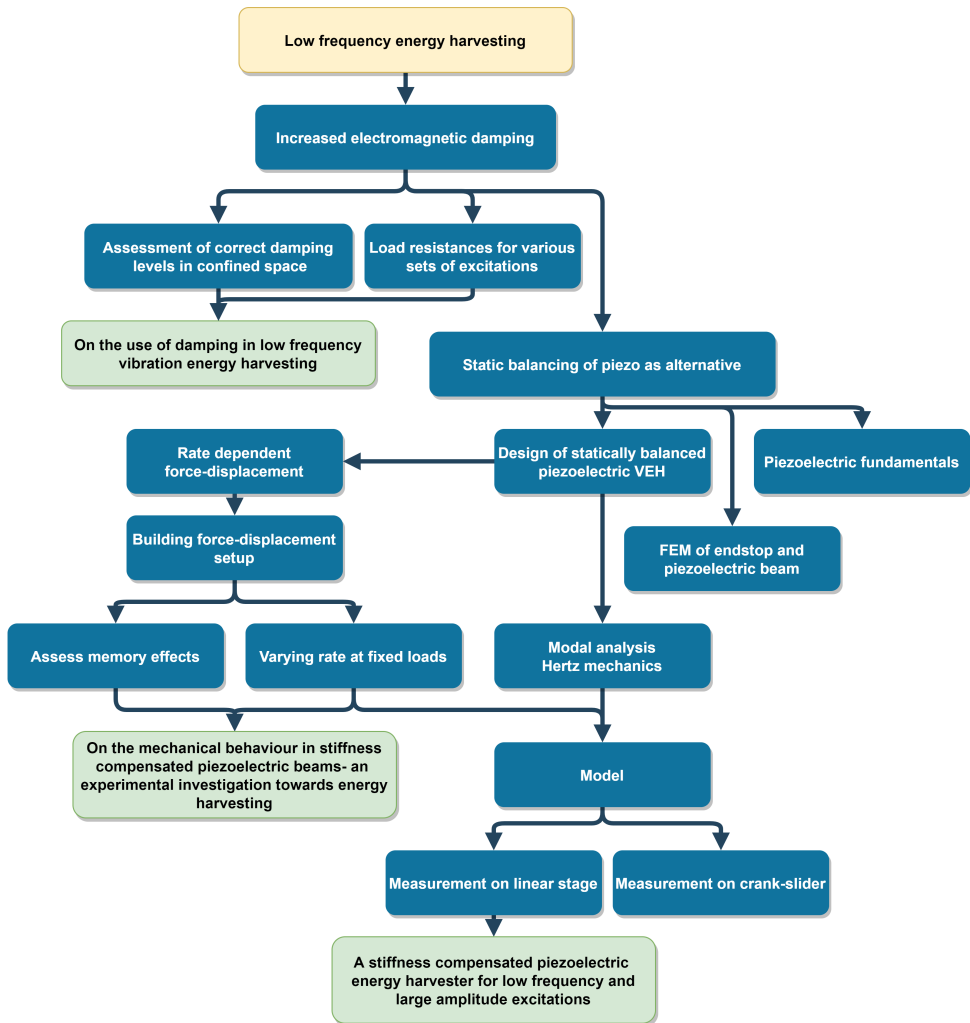


Figure 7.1: Overview of activities during the project. Yellow indicates the main focus of this thesis, blue the research activities and green indicates articles.

7.2. LEARNING PROCESS

The start of the thesis was a bit rough and chaotic. As static balancing is quite novel in the field of energy harvesting, it wasn't directly clear what the main issues would be. The only thing known at the start was the conception that electromagnetic transduction would

have very limited application when it comes to small VEHs operating at low frequency and large amplitudes; and that static balancing of a piezoelectric beam could form an interesting alternative. After deriving the *why* and *what for* concerning this project, the *how* was the next thing to tackle: the design process. Here, practicality outweighed real life implementability. After this point, the project started to split into two directions: first, the modelling of the dynamics and output and second the effect of taking force-displacement measurements at different rates. Strangely, these two directions remained independent from each other for quite some time. It took quite a while to realise that a force-displacement measurement of the hysteresis along with the remanent stiffness was the missing piece in the puzzle of a model. The force-displacement measurements formed a lengthy process, mainly as it was not known in advance what parameters were interesting to vary and which to keep constant.

In retrospect, the process could have been accelerated if more time was spent on finding out what exactly was to be measured and if the prototypes could have been dynamically tested in an earlier stage. Much time was consumed by not exactly knowing what was to be measured. This is something that would be done differently in a future project.

7.3. UNSUCCESSFUL ATTEMPTS

The least successes were found in the finite element simulations. First, a FEM Hertz contact model was developed to find the endstop stiffness, but the model seemed to overestimate by at least a factor of twenty. The cause of this was never found and analytical equations were used in stead.

Next to that, a FEM model for the piezoelectric beam was developed. This model worked quite well. It was attempted to further develop it in order to predict hysteretic force-displacement curves. This attempt was no success. This was mainly for the reason that it was unclear what the exact mechanism behind the hysteresis was (this is still ongoing research), not to mention how one is to implement it in FEM. The model was also judged to be inadequate for simulation of the balanced system, as it would involve mechanics, electrostatics, electrics and electromagnetics at a very fine meshing. The computational effort would be quite inefficient and the provided insight too little. Nevertheless, the model still proved to be useful, as it was used to validate the modal analysis based model for a linear resonator. The results from these models can be found in appendix E.

7.4. CONCLUSIONS

The research goal of this thesis was to find an energy harvester that has a small length in the excitation direction, operates at low frequency with large input motions and that is efficient in terms of generator figure of merit. In the introduction, the research objective was as follows:

Design, model and experimentally validate a stiffness compensated piezoelectric energy harvester for low-frequency, large-amplitude excitation.

- The **design** has proven to be very suitable for the art of stiffness compensation. Early prototypes with tuneable magnets (appendix A, B) have shown that magnet distances can be tuned as such that a region can be created with extremely low stiffness: a near zero stiffness or neutrally stable region can be created by accurate tuning of the magnets. Achieving the same with a fixed magnet design is harder as when zero stiffness is approached, the tuning becomes more delicate. The design has its drawbacks. First, magnets limit the range of applications that the VEh can be used for. Second, repeatability is an issue. Deviations in beam stiffness of the piezo samples and in field strength of the magnets potentially prohibits mass production and enforces custom design.
- The **model** has been **validated experimentally** by sinusoidal excitation on a linear air bearing stage. Conclusions on this are a bit mixed. In most cases, voltage time signals are closely resembled, although average output power is the most important. From the results, it was seen that at frequencies below 6 Hz the power is closely resembled and the error between the model and measurement remained below 10%. However, at higher frequencies, this error rapidly explodes up to 38% at 10 Hz as the peak voltage is overestimated. The exact reason for this remains unclear. It raises the question whether quasistatic force-displacement measurements remain a representative input when the frequency increases or whether dielectric losses start to kick in. The best that can be said is that this modeling approach is very promising considering statically balanced cantilevers, but further research and development is definitely necessary.

Two research questions were posed:

How does a stiffness compensated piezoelectric beam mechanically behave?

- This question was fairly open and has been answered by means of rate-dependent force-displacement measurements. The behaviour of a piezo with a load connected strongly depends on the strain rate by which it is deformed. A load resistance can behave as if it were a closed circuit at quasistatic rate, yet may behave as if it were open circuit at a faster rate. This effect was quantized by comparing a load to the impedance matched load. At a faster strain rate, a larger amount of charge is built up, resulting in a (temporal) stiffening. Furthermore, the memory effects in hysteresis called *curve alignment* and *wipeout* that have been observed in piezoelectric actuators in literature, have also been confirmed in force-displacement measurements. The fitting curve-based method to predict

hysteretic curves inside a hysteresis loop of an actuator has also been shown to work for force-displacement measurements. This can be an excellent method for predicting the output when the full range motion is not attained. By only knowing the hysteresis data belonging to the full range motion, non-full range motion can be predicted, resulting in a large reduction of required input data.

- Another, phenomenological find is that the act of balancing a piezoelectric beam is way easier than balancing a flexure with equal bending stiffness. That means, it is easier to end up in to a statically balanced or neutrally stable state. The piezo is less sensitive to the tuning of the magnet distance compared to the flexure. A consequence of this is that the piezo, although neutrally stable, requires more force to be displaced. In terms of dynamics, a larger input amplitude is required compared to the flexure. An explanation behind this could be that a flexure is a pure stiffness component whereas a piezoelectric beam could be seen as a spring-damper element. This could mean that it behaves viscoelastically, which can be backed up by nonlinear behaviour such as creep [22], also seen in the force-displacement measurements. However, true viscoelastic behaviour has not been seen to be confirmed in literature.

To what extent can a stiffness compensated piezoelectric vibration energy harvester form a solution to the low efficiency at low motion ratios?

- It was observed that a peak generator figure of merit efficiency of 0.567% was obtained at a motion ratio of 0.18. For motion ratios below 0.6, the generator figure of merit performance is the highest according to the author's best knowledge. That is very promising for a harvester that has seen virtually no optimization yet. The volume is still pretty large to allow for quick assembly and disassembly. The package volume can be easily reduced by a factor of 3 and assuming the frame stiffness remains about the same, the efficiency also increases with a factor of 3. Furthermore, the efficiency was observed to remain relatively constant over the motion ratio. This suggests that this type of energy harvester could also harvest efficiently over a wide band of frequencies.

7.5. ON THE PERFORMANCE DECREASE OF THE MODEL

As discussed previously, after a certain frequency the model quickly starts to overestimate the voltage and the power even more. The true cause for this has not been found yet, and identification of the cause is far from straightforward. Nevertheless, a few points will be discussed that could be an influence in this. Some references are presented as well that back it up or to provide a starting point.

- As indicated in the paper the 'free' boundary condition is actually not free as the magnets introduce a force on the tip. As the deflection pattern remains the same in the simulation throughout all frequencies, a rather static error would be expected between simulation and measurement. This is not the case, at low frequency the error is small but increases with frequency. Therefore, it seems that this is not to the main problem. Nevertheless, improvements should be expected by including the negative stiffness into the mode shape.

- The electromechanical coupling term in the beam equation represents an addition in stiffness as function of the output voltage. This work also confirmed that the stiffness rises in hysteresis loops at faster rates. However, the shape of the loop changes as well at a faster rate, which is also seen in actuators [11], [23]. This effect is not included in the equations and could affect the output. For instance, when the hysteresis loops are amplified by a certain factor, the simulation starts to match again with the measurements at higher frequencies.
- Certain input variables were taken to be constant in the model and were used as specified by the manufacturer. However, literature shows that these parameters are conditionally constant. The dielectric loss tangent $\tan\delta$, which isn't directly used in the model, is a criterion for internal losses and behaves nonlinearly with the electric field across the piezo [24], [25]. An increased electrical field results in a larger loss tangent, and large voltages actually are generated in the piezo. Data from [24] suggests that for PZT, the loss tangent could be quadrupled for the peak voltage attained in this piezo.

The same goes for the piezoelectric charge constant d_{31} and the permittivity ϵ_{r33}^T [26]. The former increases the backward electromechanical coupling, which impedes the output. The latter increases the capacitance C_p , which also results into a lower output voltage.

However, on the one hand, large voltages are obtained at low frequencies where the error is low as well as at the high frequencies where the error is large. Furthermore, in [15] this model was applied to a linear resonating cantilever and the model was in good correspondence with the measurement. It is therefore not entirely clear whether this plays a role in the large error at high frequency.

- Lastly, the formulation of the endstop model may be insufficient. The linearized stiffness and damping seem to work fine and are confirmed to work properly in energy harvesting literature [17]. The coefficient of restitution has been shown to behave nonlinearly with impact speed [27]. As such, the endstop damping changes as well. Altering levels of damping at the frequencies with large error did not improve the performance. It could still be possible that the formulation of the endstops is not accurate enough and that a better formulation could increase the model's performance.

7.6. RECOMMENDATIONS

- What do noisy signals, spikes, `medfilt1()` and lots of frustration have in common? Exactly, the use of poor power supplies. Whether grounded or not, simple power supplies have proven to perform quite poorly for these measurement purposes. The solution: the use of *lab* power supplies. Seriously, the prefix *lab* has a meaning and its significance is not to be overstated.
- When measuring something novel, think about what is to be measured and what is to be expected. When the measurements are obtained, compare them to prior art related to what is measured to check if it could make sense. In this way errors

can be quickly identified, such as a calibration error in the load cell in this case. This can save a lot of time and effort.

- Watch out for being biased by experience and results from previous projects. From a previous project where a tubular Duffing oscillator was designed, it was found that the stiffness formed by magnetic forces is nonlinear; it formed a cubic function. It was therefore assumed that the negative stiffness should be nonlinear in this design as well. However, it turned out to depend strongly on magnet size and strength. By holding on to previous experience, new results may be judged to be unjustifiably incorrect, whereas they are correct in practise.

7.7. FUTURE RESEARCH RECOMMENDATIONS

Only the tip of the iceberg has been shed light on when it comes to statically balanced piezoelectric energy harvesting. There is much work to do before it can see practical implementations. A few projects or research proposals are listed below.

- Explore the output response for non-sinusoidal excitations. Human motion is also a type of motion that has large amplitudes. Could static balancing of a piezo form a solution for human motion driven devices? Can the curve fitting method from chapter 5 be used to simulate arbitrary input/output?
- Damage mitigation: prolonged endstop collision is likely to induce cracking in the piezo. Endstop optimization is important to ensure the viability of the concept for a long period of time. Next to that, optimization of the endstop modelling could be a subject for future research.
- Damage mitigation: strain homogenization along the length of the cantilever. By lateral tapering of the cantilever, the strain is more evenly distributed, resulting in a larger power density, see [9]. This could further reduce the VEHs physical footprint and could increase reliability due to better strain distribution. Development of the corresponding mode shape functions will also be interesting.
- Miniaturization of the VEH. As abrasive cutting has shown to be successful to cut piezos in various shapes, they can be cut to smaller sizes [9]. By proper optimization the package volume may be reduced to relay-size, paving the road for low-frequency VEHs that can be socketed on a PCB.
- Implementation based on buckled beams: although the downsides of using buckled beams for negative stiffness were thoroughly discussed in chapter 3, these may turn out to be less prominent in the case of strongly coupled piezoceramics. Static balancing of piezoceramics is way easier than that of a flexure, possibly due to viscoelastic effects. This provides room for investigation using buckling, which may further reduce the footprint in excitation direction. It also eliminates the possible parasitic magnetic interference with surrounding objects.
- Investigate the influence of dielectric losses for low frequency piezoelectric energy harvesting. The dielectric loss tangent is known to increase nonlinearly with the

electric field. As these become large, dielectric losses could be detrimental to harvester performance and could also be a reason for power saturation. If this has an influence, how is this to be mitigated?

ACKNOWLEDGEMENTS

First, I would like to thank my supervisor Ron van Ostayen for his valuable feedback throughout the process and my mentor Thijs Blad for his excellent support throughout the entire process. I might have even placed titles above MATLAB figures if it weren't for your feedback. Furthermore, I would like to thank my fellow 'Stroomgraaiers' for all the valuable feedback and discussions that we have had. Especially Armin Numic for valuable problem discussions and Joeri Roos for his practical feedback and solutions, be it as simple as fixing my measurements by clamping a load cell cable with a piece of duct-tape. Last, I would like to thank my parent for their support and making this possible.

APPENDICES

A

PROTOTYPES

Prior to the manufacturing of the final prototype, several prototypes were built and investigated. This chapter briefly discusses them and shows a few of their characteristics.

A.1. TESTING OF STATIC BALANCING THROUGH MAGNETS

To assess whether magnets could be useful in the art of static balancing of a cantilever beam, a quick setup was built where a flexure was clamped at its base. Two magnets were clamped around its tip and magnets glued to threaded rods were used to accurately tune the distance between the magnets and thereby the negative stiffness encountered by the beam. Aluminium 2020 profiles and 3D printed parts were used to quickly build the prototype. The result is shown in figure A.1. The prototype was also used in combination with a piezoelectric beam clamped in. As the results were satisfactory, the prototype was further developed into a compact successor that could be used for shaker testing.

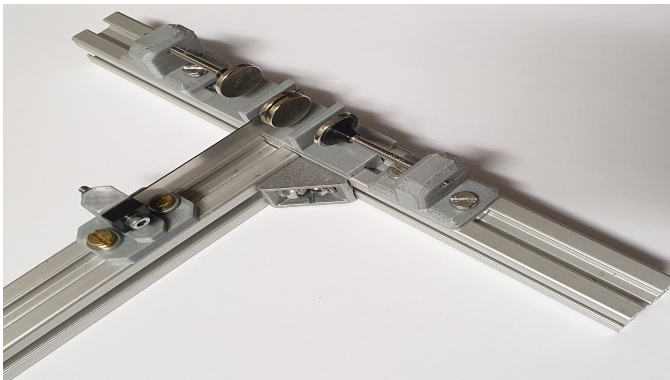


Figure A.1: **Prototype to assess the effect of static balancing by magnetic forces.**

A.2. BALANCED ENERGY HARVESTER MK.1

The previous prototype was downsized and geometrically adapted to allow shaker and force-displacement tests. The principle remains the same: magnets attached to threaded rods allow for highly accurate tuning of the zero stiffness condition. The prototype was built as such to quickly and easily swap and replace components. In stead of using two disc magnets as proof mass, a block magnet is attached to the piezo by metal epoxy glue. This allows for an improved definition of the contact stiffness between the proof mass and the endstop, as there is a line contact now. This simplifies the simulation of the contact stiffness. Two locknuts are glued on the top and bottom side of the proof mass magnet. This allows for connection of bolts to the proof mass in order to connect the energy harvester to the force-displacement setup. This new version is shown in figure A.2

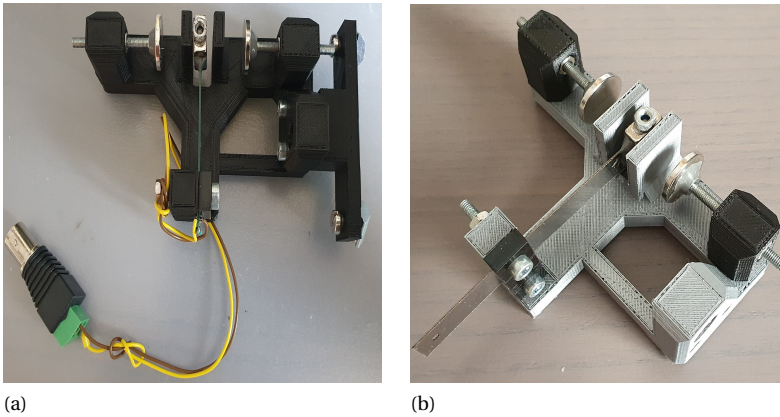


Figure A.2: Improved design of the previous prototype to allow shaker testing. In (a) a piezo is clamped, in (b) a flexure with equal bending stiffness.

A.3. BALANCED ENERGY HARVESTER MK.2

In the previous prototype it was hard to maintain reproducible measurements, as the negative stiffness could be tuned through the adjustment screws. Therefore it could also easily be detuned. As a result the necessity arose to manufacture a prototype that has a fixed geometry: the distance between proof mass and endstop magnets is fixed and cannot be changed. This results into measurements that are more reliable and reproducible, however potentially at the expense of the proximity to zero stiffness: with tuning screws it is very straightforward to reach zero stiffness as close as possible, but with a fixed magnet position this may turn out to be challenging. Figure A.3 shows the new prototype with fixed geometry. It was observed that in this configuration, it was nearly impossible to end up close to a statically balanced state. The clamping of the piezo performed poorly and had a large influence on the mechanics. The clamping was simply not stiff enough after tightening the bolts. Therefore, the need arises for a frame that clamps the

piezo symmetrically from both sides with a much larger frame stiffness. This is embodied in the final prototype.

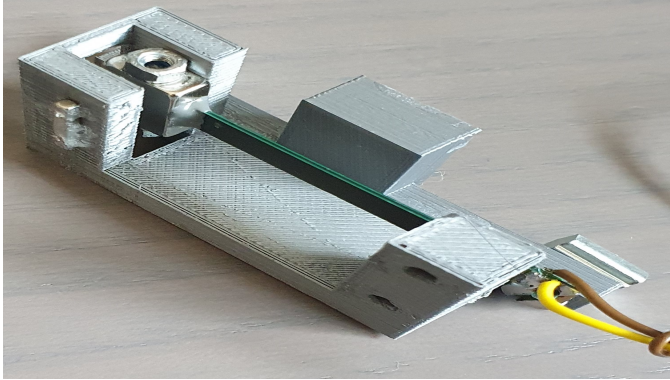


Figure A.3: **Balanced harvester mk.2 with fixed magnet design.**

B

MISCELLANEOUS MEASUREMENTS

Many force-displacement measurements were taken in this work, of which only a few were shown in the research papers. There were too many to fit it all in one coherent storyline for a paper. In this section, some of these measurements are shown. This includes measurements from early prototypes shown in appendix A. It must be noted that these measurements are not symmetric around the x-axis. There is a static offset in the measurements, which was due to a calibration error. In principle, the measurements could simply be shifted down in the force direction and they still display the qualitative behaviour.

B.1. BALANCED HARVESTER Mk.1

In appendix A the Mk.1 harvester was shown, both for the case of a piezo and a flexure that had an equal bending stiffness. The force-displacement characteristics are shown in figure B.1 for comparison. As can be seen from the figure, the uncompensated states are nearly the same. However, for the compensated conditions, great differences can be spotted. The hysteresis loop of the piezo is much larger than that of the flexure. Furthermore, the required force to move the flexure is also a lot less compared to the piezo. In practice, it was found that it was way easier to balance the piezo compared to the flexure. This observation also relates to the figure: with a much lower force level, the flexure is perturbed more easily, making it harder to balance it. This also means that it needs less input acceleration to move the beam, introducing a tradeoff: easier to balance and harder to move it dynamically or harder to balance and easier to move dynamically.

The piezo has a zero stiffness region around zero displacement and then the stiffness becomes positive. The magnets were not close enough to provide full range zero stiffness. For the flexure, the opposite is true. First around zero displacement the stiffness is slightly positive, then it decreases and becomes slightly negative. In this case, the fixed magnets are larger disk magnets and therefore likely provide a nonlinear negative stiffness, opposed to the magnets used in the final prototype which provided a nearly linear negative stiffness.

Figure B.1c shows what can be truly achieved in terms of zero stiffness when the fixed magnet distance is tuned to the best position. In this case, around two-thirds of the displacement limit has a zero stiffness condition. The figure really shows the advantage of having a tunable negative stiffness.

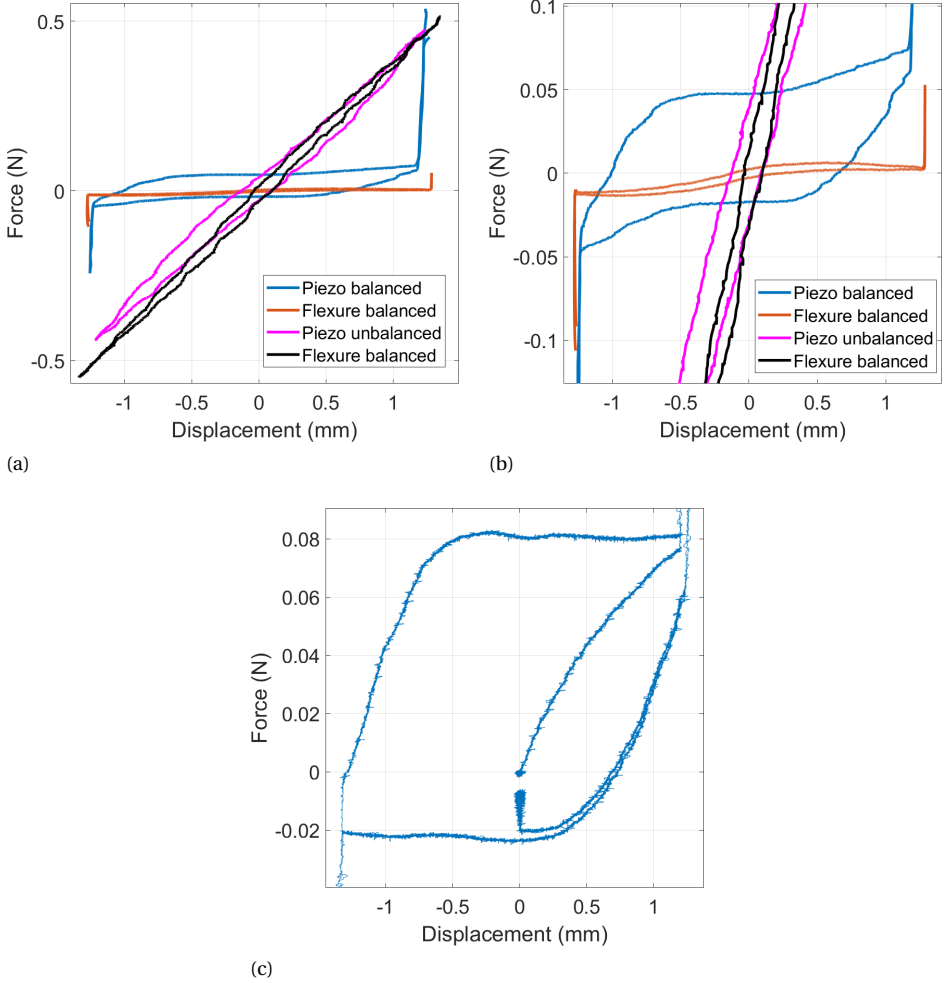


Figure B.1: **Force-displacement graph of the MK.1 harvesters in unbalanced and balanced state. Figure (c) shows the best tuning configuration resulting in a large zero stiffness region.**

B.2. MEASUREMENTS AT FIXED LOAD AND VARIED SPEED

In the force-displacement research paper, the plots shown were at fixed speed and different loads. Turning it around, plotting at fixed load and different speeds, the plots in figure B.2 are obtained. The measurements were not taken at full displacement range.

A few interesting things may be noted. First, it can be seen that for the open circuit, the hysteresis loop becomes thinner at faster rates, whereas it grows for the other cases. Furthermore, it can be seen that there is barely any difference between the 10M Ω and 1M Ω case. Perhaps the stiffening effects that were found in the force-displacement paper are less pronounced at lower displacements or without endstop hits.

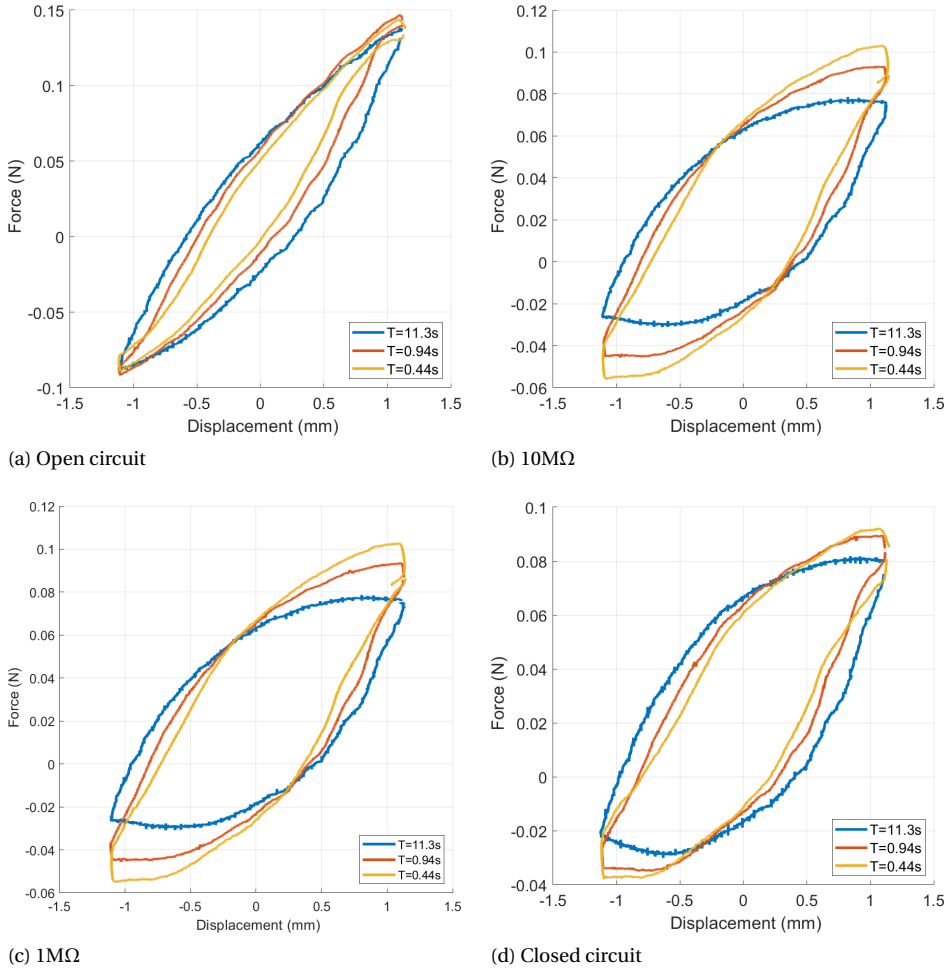


Figure B.2: Force-displacement measurements at fixed loads and varied speeds. In the legend, T indicates the time period to close a full loop.

B.3. FURTHER APPLICATION OF HYSTERESIS MAPPING

In chapter 5 it was shown that inner hysteresis curves could be predicted by fitting curves to the outer hysteresis loop. The inner curves could be predicted by 'mapping' the outer

curves to a certain start and end point while retaining the same fit parameters, similar to what had been done in [21]. Figure B.3 shows another application of this method. The blue curve is the full range motion curve along with the response for a smaller input displacement. This could occur at low input accelerations or it can be considered as an exaggerated endstop bounce. The figure shows that once the outer ascending and descending curves have been fitted, the inner ascending and descending curves can be predicted by using the same fitting parameters but different start and endpoints. Although this is not very different than what is shown in the paper in chapter 5, the application of this is worth to mention. In chapter 6 it was shown that using the full range motion curve for non-full range motion results in poor simulation performance. Using the non-full range motion curves, the performance increased. It was mentioned that for every distinctive non-full range displacement, a separately measured hysteresis curve would need to be used, which is far from efficient. This fitting technique shows a possible solution to that. By knowing the outer/full range curves, technically any inner curve should be predictable. This implies that for non-full range motion, the hysteresis curves could be predicted in real time by the ode solver by continuously generating a hysteresis curve based on current and past displacement data.

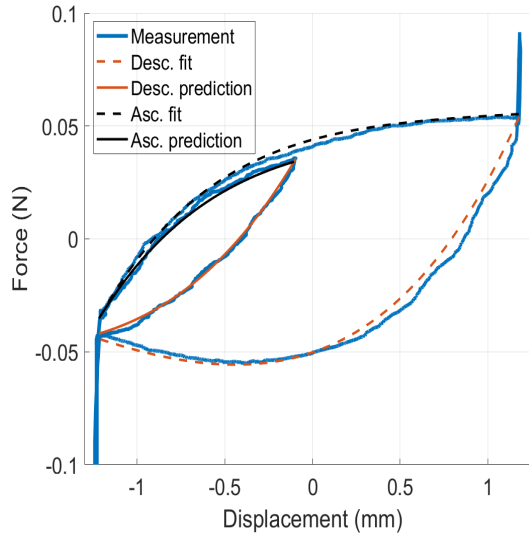


Figure B.3: By fitting curves to the outer loop, the trajectories of the inner loop can be predicted.

C

DATA OF PIEZOELECTRIC BEAM

In this section the specifications of the used piezoelectric element are shown. The elements are from Morgan Ceramics, made from PZT-508. Figure C.1 shows the piezo that is used. On the right the gilded terminals can be seen.



Figure C.1: **PZT-508 piezo** used throughout the research.

The yellow tip at the very left (left of the gilded strip left) is the actual colour of the piezoelectric material and reveals many of its properties, according to [12]: a yellow colour indicates that it belongs to the class of 'soft' piezoelectric materials. This class is known for its large dielectric constant and large coupling coefficient. It has a larger electric resistance and is less stiff. Furthermore, its quality factor is relatively low, indicating larger dielectric losses. These losses will even increase when large electric fields are present within the material [24], which is not really beneficial in the case of a balanced piezo. The low frequency operation enforces the use of large load resistances, leading to large voltages. Table C.1 displays the numerical data belonging to the used piezo.

Table C.1: **Manufacturer data for PZT-508 material of which the piezoelectric beams are made. Data are retrieved from [9].**

Description	symbol	quantity	unit
Relative permittivity	ϵ_{r33}^T	3900	
Dielectric loss tangent	$\tan \delta$	0.02	
Coupling factors	k_p	0.71	
	k_{15}	0.72	
	k_{31}	0.41	
	K_{33}	-0.75	
Charge constants	d_{33}	720	$\times 10^{-12} \text{C/N}$
	d_{31}	-315	$\times 10^{-12} \text{C/N}$
	d_{15}	750	$\times 10^{-12} \text{C/N}$
Voltage constants	g_{33}	18.5	$\times 10^{-3} \text{Vm/N}$
	g_{31}	-9	$\times 10^{-3} \text{Vm/N}$
Quality factor	Q_m	55	
Compliance	S_{33}^E	22	$\times 10^{-12} \text{m}^2/\text{N}$
	S_{11}^E	16.4	$\times 10^{-12} \text{m}^2/\text{N}$
	S_{33}^D	8.8	$\times 10^{-12} \text{m}^2/\text{N}$
	S_{33}^D	13.9	$\times 10^{-12} \text{m}^2/\text{N}$
Elasticity	Y_{33}^E	49	$\times 10^9 \text{Pa}$
	Y_{11}^E	61	$\times 10^9 \text{Pa}$
	Y_{33}^D	110	$\times 10^9 \text{Pa}$
	Y_{33}^D	70	$\times 10^9 \text{Pa}$
Density	ρ	7900	kg/m^3
Curie Temperature	T_c	208	$^\circ\text{C}$

D

FIGURE OF MERIT

The generator figure of merit from [2], derived from the volume figure of merit [6], [3] is a parameter that plays a central role in this work. It allows for a more fair comparison between energy harvesters. However, the formula is not that straightforward. Therefore, in this section it is shown how it can be derived and interpreted. One can start with the most simple equation for a mass-spring-damper system:

$$M\ddot{z} + (C_e + C_m)\dot{z} + Kz = Ma_0 \quad (\text{D.1})$$

Where M , C_e , C_m , K , z , a_0 are the mass, electrical and mechanical damping, stiffness, relative proof mass displacement and input acceleration, respectively. At resonance, the inertial and stiffness terms cancel each other, and only the damping and forcing terms are left:

$$(C_e + C_m)z\omega_n = Ma_0 \quad (\text{D.2})$$

Note that for the case of sinusoidal excitation, the velocity can be written in terms of the natural frequency ω_n . The amplitude can be found while the assumption is made that the electrical damping equals the mechanical:

$$z = \frac{Ma_0}{(C_e + C_m)\omega_n} = \frac{Ma_0}{2C_m\omega_n} \quad (\text{D.3})$$

The average power can be found by integrating the power over a cycle and once again assuming sinusoidal motion:

$$P_{avg} = \frac{1}{T} \int_0^T P(t) dt = \frac{1}{T} \int_0^T C_e \dot{z}^2 dt \quad (\text{D.4})$$

$$P_{avg} = \frac{\omega_n}{2\pi} \int_0^{2\pi/\omega_n} C_e \frac{M^2 a_0^2}{(C_e + C_m)^2} \cos^2 \omega t dt = \frac{1}{2} C_e \frac{M^2 a_0^2}{(C_e + C_m)^2} \quad (\text{D.5})$$

With the electrical damping matched to the mechanical and using eqn. D.3, the maximum average power is found as:

$$P_{avg,max} = \frac{M^2 a_0^2}{8C_m} = \frac{Ma_0 z \omega_n}{4} \quad (D.6)$$

It can be seen that the maximum power at resonance depends on the mass, input acceleration, displacement limit and natural frequency. The mass and displacement limit can be designed for, and should thus be maximized. The idea of the volume figure of merit FoM_v is to compare the output power to a reference benchmark harvester that forms the performance limit. This reference harvester is defined by having a cubic shape with a volume and input conditions equal to the harvester that is benchmarked. Figure D.1 shows the reference harvester. The proof mass density is defined to be of gold, which is to set a high standard and it is beneficial for MEMS devices [3]. So to maximize the reference harvester power, the product of the proof mass and displacement limit must be maximized, defined as follows:

$$P_{ref} = \frac{\rho_{Au} a^2 b (a - b) a_0 \omega_n}{4} \quad (D.7)$$

The term $a^2 b (a - b)$ must therefore be maximized and it can be easily identified that this is achieved at $b = a/2$. This means that the proof mass length is equal to half the length of the harvester. As a result, the reference power is equal to:

$$P_{ref} = \frac{\rho_{Au} a_0 \omega_n a^4}{16} = \frac{\rho_{Au} a_0 \omega_n V^{4/3}}{16} = \frac{\rho_{Au} V^{4/3} y_0 \omega_n^3}{16} \quad (D.8)$$

The FoM_v is then defined as the ratio between the average power of the built VEH and that of the performance limit set by the reference harvester:

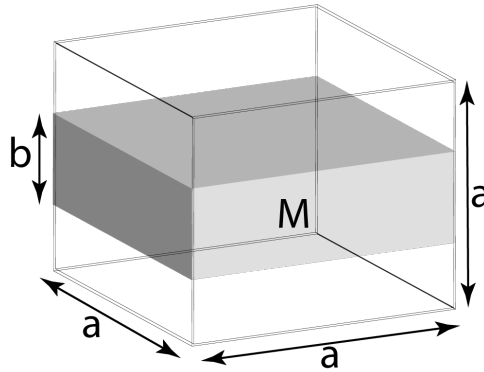


Figure D.1: Reference energy harvester of cubic shape and volume and proof mass equal to the benchmarked harvester.

$$FoM_v = \frac{P_{avg,VEH}}{P_{ref}} = \frac{P_{avg,VEH}}{\frac{1}{16} \rho_{Au} Y_0 V^{4/3} \omega_n^3} \quad (D.9)$$

As pointed out in [2], it was shown in [6] that the maximum power in a VEH depends nonlinearly on the length of the VEH and linearly on the other dimensions, see eqn. 1.5. It could therefore be argued that given two VEHs of equal volume and mass, the harvester that is the longest in the excitation direction will always perform better in terms of FoM_v . As a result, it can be argued that this performance metric is biased toward certain shapes of a VEH. To remove this bias, [2] proposed a variation on the FoM_v by changing $V^{4/3}$ to VL_z where L_z is the VEH's length. In this way, the metric also takes shape into consideration. Furthermore, the density of gold was changed into the density of the proof mass, which would also be a more fair comparison. This variation was named the generator figure of merit and is defined as:

$$FoM_v = \frac{P_{avg,VEH}}{P_{ref}} = \frac{P_{avg,VEH}}{\frac{1}{16}\rho_{PM}Y_0VL_z\omega_n^3} \quad (D.10)$$

E

COMSOL MODELS OF PIEZOELECTRIC BEAM AND ENDSTOP STIFFNESS

E.1. PIEZOELECTRIC MODEL

The force-displacement data of the stiffness compensated piezo were mainly used to investigate the behaviour of the piezo in this state and to use this as an input to the ODE-solver in MATLAB. Although this is a straightforward method, it forces the design of such an energy harvester somewhat into an iterative of forward-backward process. Dimensions of the piezo have to be assessed and then once the piezo is acquired measurements have to be done and to be judged whether everything is satisfactory. It would be a great improvement if the hysteretic behaviour of the piezo could be simulated as well, enabling more freedom in the design process and making it more unidirectional.

As COMSOL Multiphysics includes a piezoelectric and electrostatic package, piezoelectric cantilevers and accompanying electrical circuits can be easily modelled. Figure E.1 shows the geometry of the piezo cantilever. In the figure, the two-dimensional geometry of the beam can be seen. The middle layer is the substrate layer with the piezoelectric layer on top and bottom of it. The two rectangular blocks on the left form the clamping. At the right end of the cantilever, a proof mass is connected. Figure E.2 shows the stress of the cantilever at resonance.

Unfortunately, a model to predict the hysteresis behaviour in the piezo couldn't be constructed successfully. A reason for this is that, unlike hysteresis in magnets, hysteresis in piezoelectric elements is still quite in its infancy. The real origins and mechanisms behind the hysteresis aren't entirely known yet. Consequentially, there is virtually nothing to refer to when constructing such a model. Furthermore, most hysteresis models in literature are based on actuation mode, so putting a voltage on the piezo and measuring displacement. In this case however, a displacement is imposed and the force measured.

In order to still make use from the model and not to discard it, the frequency response

E

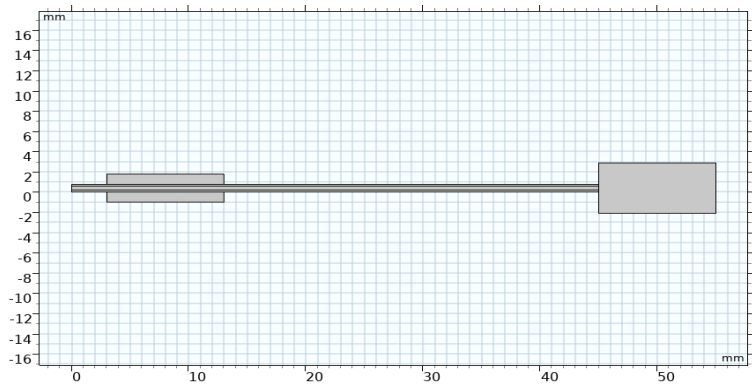


Figure E.1: Geometry of the piezoelectric cantilever that is modelled.

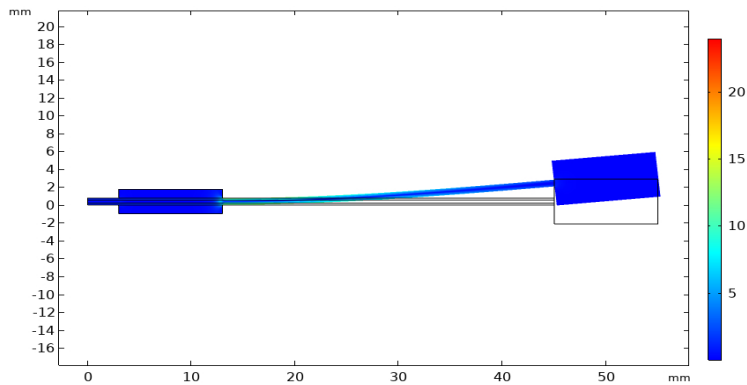


Figure E.2: Stress of deformed cantilever at resonance.

of the cantilever was simulated to provide a comparison to the results from the MATLAB ODE model. In this way the results can be verified. In figure E.3 a comparison is shown between both models for an applied frequency response of an unbalanced cantilever. As can be seen, the results match very closely. A few differences can be spotted which are mainly due to variations in the used material parameters. All in all, these results confirm the suitability of the electromechanical model in MATLAB.

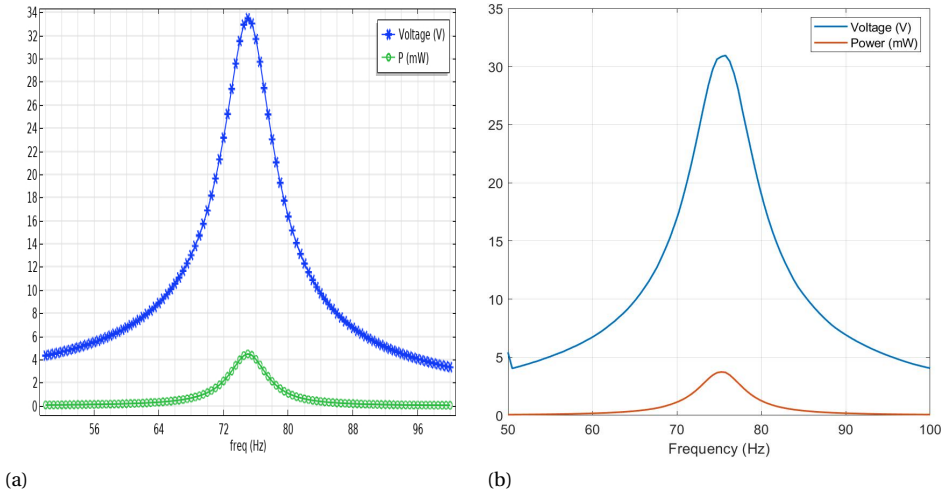


Figure E.3: Comparison of results from (a) COMSOL simulation and (b) MATLAB simulation.

E.2. ENDSTOP STIFFNESS

Besides the Hertz contact mechanics modelling, a COMSOL model was developed to find the the endstop stiffness. This was for the reason that it wasn't certain whether the contact could really be defined as a cylinder on a plate.

Figure E.4 shows the proof mass magnet on top making contact with energy harvester frame below it, consequentially forming a contact stress region. The red boundaries indicate the fixed constraints and the green arrow indicates the applied displacement. The variables of interest are the indentation of the magnet into the endstop and the total contact force that the magnet encounters. Evaluating this for a set of indentations, a force-indentation graph can be found showing the required force to indent the endstop, which is shown in figure E.5. As can be seen, the contact force and corresponding contact stiffness are way higher in comparison to the Hertz mechanics. The contact stiffness amounts 5.5MN/m compared to the 250kN/m from Hertz. It was expected that the COMSOL simulation should closely match the analytical formulations from the Hertz mechanics. Unfortunately, the problem couldn't be resolved and the results from Hertz mechanics were continued to be used.

E

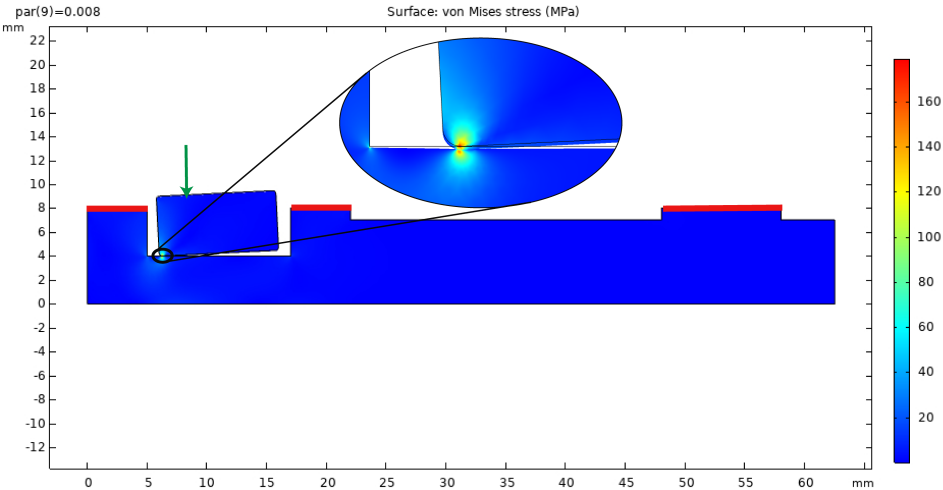


Figure E.4: Contact stress simulation of contact between proof mass magnet and endstop. The red lines indicate the fixed constraints, green arrow the applied displacement.

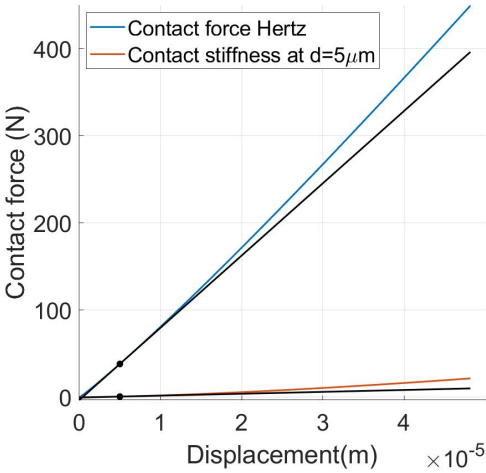


Figure E.5: Contact stiffness between the proof mass magnet and endstop. A comparison is made between the COMSOL model and the Hertz contact mechanics.

F

REFERENCES

REFERENCES

- [1] H. Alawad and S. Kaewunruen, “Wireless Sensor Networks: Toward Smarter Railway Stations,” *Infrastructures*, vol. 3, no. 3, p. 24, Sep. 2018. [Online]. Available: <https://www.mdpi.com/2412-3811/3/3/24>
- [2] T. W. Blad and N. Tolou, “On the efficiency of energy harvesters: A classification of dynamics in miniaturized generators under low-frequency excitation,” *Journal of Intelligent Material Systems and Structures*, vol. 30, no. 16, pp. 2436–2446, Sep. 2019. [Online]. Available: <https://doi.org/10.1177/1045389X19862621>
- [3] W. Q. Liu, A. Badel, F. Formosa, and Y. P. Wu, “A new figure of merit for wideband vibration energy harvesters,” *Smart Mater. Struct.*, vol. 24, no. 12, p. 125012, Oct. 2015. [Online]. Available: <https://doi.org/10.1088%2F0964-1726%2F24%2F12%2F125012>
- [4] T. O'Donnell, C. Saha, S. Beeby, and J. Tudor, “Scaling effects for electromagnetic vibrational power generators,” *Microsyst Technol*, vol. 13, no. 11, pp. 1637–1645, Jul. 2007. [Online]. Available: <https://doi.org/10.1007/s00542-006-0363-0>
- [5] P. D. Mitcheson, E. K. Reilly, T. Toh, P. K. Wright, and E. M. Yeatman, “Performance limits of the three MEMS inertial energy generator transduction types,” *J. Micromech. Microeng.*, vol. 17, no. 9, pp. S211–S216, Aug. 2007. [Online]. Available: <https://doi.org/10.1088%2F0960-1317%2F17%2F9%2Fs01>
- [6] P. D. Mitcheson, E. M. Yeatman, G. K. Rao, A. S. Holmes, and T. C. Green, “Energy Harvesting From Human and Machine Motion for Wireless Electronic Devices,” *Proc. IEEE*, vol. 96, no. 9, pp. 1457–1486, Sep. 2008.
- [7] M. Geisler, S. Boisseau, M. Perez, P. Gasnier, J. Willemin, I. Ait-Ali, and S. Perraud, “Human-motion energy harvester for autonomous body area sensors,”

- Smart Mater. Struct.*, vol. 26, no. 3, p. 035028, 2017. [Online]. Available: <http://stacks.iop.org/0964-1726/26/i=3/a=035028>
- [8] S. P. Beeby, R. N. Torah, M. J. Tudor, P. Glynne-Jones, T. O'Donnell, C. R. Saha, and S. Roy, "A micro electromagnetic generator for vibration energy harvesting," *J. Micromech. Microeng.*, vol. 17, no. 7, pp. 1257–1265, Jun. 2007. [Online]. Available: <https://doi.org/10.1088%2F0960-1317%2F17%2F7%2F007>
- [9] J. Brans, "Piezoelectric Vibrational Energy Harvesting," Msc. Thesis, Delft University of Technology, Delft, Mar. 2020.
- [10] A. Erturk and D. J. Inman, "Issues in mathematical modeling of piezoelectric energy harvesters," *Smart Mater. Struct.*, vol. 17, no. 6, p. 065016, Dec. 2008. [Online]. Available: <http://stacks.iop.org/0964-1726/17/i=6/a=065016?key=crossref.2c9ea418f2ce70369a621285b33432a8>
- [11] M. A. Janaideh, C.-Y. Su, and S. Rakheja, "Development of the rate-dependent Prandtl–Ishlinskii model for smart actuators," *Smart Mater. Struct.*, vol. 17, no. 3, p. 035026, Apr. 2008. [Online]. Available: <https://doi.org/10.1088%2F0964-1726%2F17%2F3%2F035026>
- [12] P. Groen and J. Holterman, *An Introduction to Piezoelectric Materials and Components*, 1st ed. Apeldoorn: Stichting Applied Piezo, 2012.
- [13] J. Ajitsaria, S. Y. Choe, D. Shen, and D. J. Kim, "Modeling and analysis of a bimorph piezoelectric cantilever beam for voltage generation," *Smart Mater. Struct.*, vol. 16, no. 2, pp. 447–454, Feb. 2007. [Online]. Available: <https://doi.org/10.1088%2F0964-1726%2F16%2F2%2F024>
- [14] D. J. Inman and A. Erturk, *Piezoelectric Energy Harvesting*, 1st ed. Chichester: John Wiley & Sons, 2011.
- [15] A. Erturk and D. J. Inman, "An experimentally validated bimorph cantilever model for piezoelectric energy harvesting from base excitations," *Smart Mater. Struct.*, vol. 18, no. 2, p. 025009, Feb. 2009. [Online]. Available: <https://iopscience.iop.org/article/10.1088/0964-1726/18/2/025009>
- [16] S. S. Rao, *Mechanical Vibrations*, 6th ed. Harlow: Pearson, 2018.
- [17] M. S. M. Soliman, E. M. Abdel-Rahman, E. F. El-Saadany, and R. R. Mansour, "A wideband vibration-based energy harvester," *J. Micromech. Microeng.*, vol. 18, no. 11, p. 115021, Oct. 2008. [Online]. Available: <https://doi.org/10.1088%2F0960-1317%2F18%2F11%2F115021>
- [18] A. van Beek, *Advanced Engineering Design*, 6th ed. Delft: TU Delft, 2015.
- [19] H. Soemers, *Design Principles for Precision Mechanisms*. T-pointprint, 2017.

- [20] D. Zhao and Y. Liu, "Improved Damping Constant of Hertz-Damp Model for Pounding between Structures," *Mathematical Problems in Engineering*, vol. 2016, pp. 1–7, 2016. [Online]. Available: <http://www.hindawi.com/journals/mpe/2016/9161789/>
- [21] S. Bashash and N. Jalili, "Underlying memory-dominant nature of hysteresis in piezoelectric materials," *Journal of Applied Physics*, vol. 100, no. 1, p. 014103, Jul. 2006. [Online]. Available: <https://aip-scitation-org.tudelft.idm.oclc.org/doi/full/10.1063/1.2208805>
- [22] R. Munnig Schmidt, G. Schitter, A. Rankers, and J. van Eijk, "The design of high performance mechatronics." Amsterdam: Delft University Press, 2014.
- [23] M.-J. Yang, C.-X. Li, G.-Y. Gu, and L.-M. Zhu, "A Modified Prandtl-Ishlinskii Model for Rate-dependent Hysteresis Nonlinearity Using mth-power Velocity Damping Mechanism," *International Journal of Advanced Robotic Systems*, vol. 11, no. 10, p. 163, Oct. 2014. [Online]. Available: <https://doi.org/10.5772/58984>
- [24] A. Morel, G. Pillonnet, Y. Wanderoild, and A. Badel, "Dielectric Losses Considerations for Piezoelectric Energy Harvesting," *J. Low Power Electron.*, vol. 14, pp. 244–254, Jun. 2018. [Online]. Available: <https://hal.archives-ouvertes.fr/hal-01865139>
- [25] K. Uchino and S. Hirose, "Loss mechanisms in piezoelectrics: How to measure different losses separately," *IEEE Trans. Ultrason. Ferroelectr. Freq. Control*, vol. 48, no. 1, pp. 307–321, Jan. 2001.
- [26] L. Pardo and J. Ricote, *Multifunctional Polycrystalline Ferroelectric Materials*. Dordrecht: Springer, 2011.
- [27] L. J. Blystad, E. Halvorsen, and S. Husa, "Piezoelectric MEMS energy harvesting systems driven by harmonic and random vibrations," *IEEE Trans. Ultrason. Ferroelectr. Freq. Control*, vol. 57, no. 4, pp. 908–919, Apr. 2010.
- [28] G. Aldawood, H. T. Nguyen, and H. Bardaweel, "High power density spring-assisted nonlinear electromagnetic vibration energy harvester for low base-accelerations," *Applied Energy*, vol. 253, p. 113546, Nov. 2019. [Online]. Available: <http://www.sciencedirect.com/science/article/pii/S0306261919312206>
- [29] K. Ashraf, M. H. M. Khir, J. O. Dennis, and Z. Baharudin, "A wideband, frequency up-converting bounded vibration energy harvester for a low-frequency environment," *Smart Mater. Struct.*, vol. 22, no. 2, p. 025018, Jan. 2013. [Online]. Available: <https://doi.org/10.1088%2F0964-1726%2F22%2F2%2F025018>
- [30] A. G. Avila Bernal and L. E. Linares García, "The modelling of an electromagnetic energy harvesting architecture," *Applied Mathematical Modelling*, vol. 36, no. 10, pp. 4728–4741, Oct. 2012. [Online]. Available: <http://www.sciencedirect.com/science/article/pii/S0307904X11007931>

- [31] D. F. Berdy, P. Srisungsitthisunti, X. Xu, J. Rhoads, B. Jung, and D. Peroulis, "Compact low frequency meandered piezoelectric energy harvester," *Proc.PowerMEMS*, p. 4, 2009.
- [32] D. F. Berdy, D. J. Valentino, and D. Peroulis, "Design and optimization of a magnetically sprung block magnet vibration energy harvester," *Sensors and Actuators A: Physical*, vol. 218, pp. 69–79, Oct. 2014. [Online]. Available: <http://www.sciencedirect.com/science/article/pii/S0924424714003069>
- [33] Q. Cai and S. Zhu, "Unified strategy for overall impedance optimization in vibration-based electromagnetic energy harvesters," *International Journal of Mechanical Sciences*, vol. 165, p. 105198, Jan. 2020. [Online]. Available: <https://linkinghub.elsevier.com/retrieve/pii/S0020740319329418>
- [34] A. Cammarano, S. Neild, S. Burrow, D. Wagg, and D. Inman, "Optimum resistive loads for vibration-based electromagnetic energy harvesters with a stiffening nonlinearity," *Journal of Intelligent Material Systems and Structures*, vol. 25, no. 14, pp. 1757–1770, Sep. 2014. [Online]. Available: <https://doi.org/10.1177/1045389X14523854>
- [35] A. Cammarano, S. G. Burrow, D. A. W. Barton, A. Carrella, and L. R. Clare, "Tuning a resonant energy harvester using a generalized electrical load," *Smart Mater. Struct.*, vol. 19, no. 5, p. 055003, Mar. 2010. [Online]. Available: <https://doi.org/10.1088%2F0964-1726%2F19%2F5%2F055003>
- [36] V. R. Challa, M. G. Prasad, and F. T. Fisher, "A coupled piezoelectric–electromagnetic energy harvesting technique for achieving increased power output through damping matching," *Smart Mater. Struct.*, vol. 18, no. 9, p. 095029, Aug. 2009. [Online]. Available: <https://doi.org/10.1088%2F0964-1726%2F18%2F9%2F095029>
- [37] V. R. Challa, M. G. Prasad, Y. Shi, and F. T. Fisher, "A vibration energy harvesting device with bidirectional resonance frequency tunability," *Smart Mater. Struct.*, vol. 17, no. 1, p. 015035, Jan. 2008. [Online]. Available: <https://doi.org/10.1088%2F0964-1726%2F17%2F01%2F015035>
- [38] S. Cheng, N. Wang, and D. P. Arnold, "Modeling of magnetic vibrational energy harvesters using equivalent circuit representations," *J. Micromech. Microeng.*, vol. 17, no. 11, pp. 2328–2335, Oct. 2007. [Online]. Available: <https://doi.org/10.1088%2F0960-1317%2F17%2F11%2F021>
- [39] M. F. Daqaq, R. Masana, A. Erturk, and D. Dane Quinn, "On the Role of Nonlinearities in Vibratory Energy Harvesting: A Critical Review and Discussion," *Appl. Mech. Rev.*, vol. 66, no. 4, Jul. 2014. [Online]. Available: <https://asmedigitalcollection.asme.org/appliedmechanicsreviews/article/66/4/040801/472587/On-the-Role-of-Nonlinearities-in-Vibratory-Energy>
- [40] F. M. Foong, C. Ket Thein, and A. R. Abdul Aziz, "Effect of Electromagnetic Damping on the Optimum Load Resistance of an Electromagnetic Vibration Energy Harvester," in *2018 2nd International Conference on Smart Grid and Smart Cities (ICS-GSC)*, Aug. 2018, pp. 127–132.

- [41] T. Galchev, H. Kim, and K. Najafi, "Micro Power Generator for Harvesting Low-Frequency and Nonperiodic Vibrations," *J. Microelectromechanical Syst.*, vol. 20, no. 4, pp. 852–866, Aug. 2011.
- [42] T. Galchev, E. E. Aktakka, and K. Najafi, "A Piezoelectric Parametric Frequency Increased Generator for Harvesting Low-Frequency Vibrations," *J. Microelectromechanical Syst.*, vol. 21, no. 6, pp. 1311–1320, Dec. 2012.
- [43] J. Gan and X. Zhang, "A review of nonlinear hysteresis modeling and control of piezoelectric actuators," *AIP Advances*, vol. 9, no. 4, p. 040702, Apr. 2019. [Online]. Available: <https://aip.scitation.org/doi/10.1063/1.5093000>
- [44] P. L. Green, K. Worden, K. Atallah, and N. D. Sims, "The benefits of Duffing-type nonlinearities and electrical optimisation of a mono-stable energy harvester under white Gaussian excitations," *Journal of Sound and Vibration*, vol. 331, no. 20, pp. 4504–4517, Sep. 2012. [Online]. Available: <http://www.sciencedirect.com/science/article/pii/S0022460X12003549>
- [45] L. Gu and C. Livermore, "Impact-driven, frequency up-converting coupled vibration energy harvesting device for low frequency operation," *Smart Mater. Struct.*, vol. 20, no. 4, p. 045004, Mar. 2011. [Online]. Available: <https://doi.org/10.1088%2F0964-1726%2F20%2F4%2F045004>
- [46] M. A. Halim, H. Cho, and J. Y. Park, "Design and experiment of a human-limb driven, frequency up-converted electromagnetic energy harvester," *Energy Conversion and Management*, vol. 106, pp. 393–404, Dec. 2015. [Online]. Available: <http://www.sciencedirect.com/science/article/pii/S0196890415009103>
- [47] M. Halim and J. Park, "Modeling and experiment of a handy motion driven, frequency up-converting electromagnetic energy harvester using transverse impact by spherical ball," *Sensors and Actuators A: Physical*, vol. 229, pp. 50–58, Jun. 2015. [Online]. Available: <http://www.sciencedirect.com/science/article/pii/S0924424715001478>
- [48] H. Huang, C. Zheng, X. Ruan, J. Zeng, L. Zheng, W. Chen, and G. Li, "Elastic and Electric Damping Effects on Piezoelectric Cantilever Energy Harvesting," *Ferroelectrics*, vol. 459, no. 1, pp. 1–13, Jan. 2014. [Online]. Available: <https://doi.org/10.1080/00150193.2013.837735>
- [49] D. J. Inman and S. Priya, *Energy Harvesting Technologies*, 1st ed. New York: Springer, 2009. [Online]. Available: [DOI10.1007/978-0-387-76464-1](https://doi.org/10.1007/978-0-387-76464-1)
- [50] A. J. Lamers, J. A. Gallego Sánchez, and J. L. Herder, "Design of a statically balanced fully compliant grasper," *Mechanism and Machine Theory*, vol. 92, pp. 230–239, Oct. 2015. [Online]. Available: <http://www.sciencedirect.com/science/article/pii/S0094114X15001342>
- [51] Y. Liao and J. Liang, "Maximum power, optimal load, and impedance analysis of piezoelectric vibration energy harvesters," *Smart Mater. Struct.*, vol. 27, no. 7, p.

- 075053, Jul. 2018. [Online]. Available: <http://stacks.iop.org/0964-1726/27/i=7/a=075053?key=crossref.34ae8a89af8860232646e09d3d84e859>
- [52] C. Li, S. Wu, P. C. K. Luk, M. Gu, and Z. Jiao, “Enhanced Bandwidth Nonlinear Resonance Electromagnetic Human Motion Energy Harvester Using Magnetic Springs and Ferrofluid,” *IEEEASME Trans. Mechatron.*, vol. 24, no. 2, pp. 710–717, Apr. 2019.
- [53] A. Munaz, B.-C. Lee, and G.-S. Chung, “A study of an electromagnetic energy harvester using multi-pole magnet,” *Sens. Actuators Phys.*, vol. 201, pp. 134–140, Oct. 2013. [Online]. Available: <http://linkinghub.elsevier.com/retrieve/pii/S0924424713003191>
- [54] A. Nammari, L. Caskey, J. Negrete, and H. Bardaweel, “Fabrication and characterization of non-resonant magneto-mechanical low-frequency vibration energy harvester,” *Mechanical Systems and Signal Processing*, vol. 102, pp. 298–311, Mar. 2018. [Online]. Available: <http://www.sciencedirect.com/science/article/pii/S0888327017305198>
- [55] J. Park and M. A. Halim, “Theoretical modeling and analysis of mechanical impact driven and frequency up-converted piezoelectric energy harvester for low-frequency and wide-bandwidth operation,” *Sensors and Actuators A: Physical*, vol. 208, pp. 56–65, Feb. 2014. [Online]. Available: <http://www.sciencedirect.com/science/article/pii/S0924424713006316>
- [56] P. Pillatsch, E. M. Yeatman, and A. S. Holmes, “A scalable piezoelectric impulse-excited energy harvester for human body excitation,” *Smart Mater. Struct.*, vol. 21, no. 11, p. 115018, Oct. 2012. [Online]. Available: <https://doi.org/10.1088%2F0964-1726%2F21%2F11%2F115018>
- [57] R. Rantz and S. Roundy, “Characterization of Real-world Vibration Sources and Application to Nonlinear Vibration Energy Harvesters,” *Energy Harvest. Syst.*, vol. 4, no. 2, pp. 67–76, Aug. 2019. [Online]. Available: <http://www.degruyter.com/view/j/ehs.2017.4.issue-2/ehs-2016-0021/ehs-2016-0021.xml>
- [58] S. S. Rao, *Vibration of Continuous Systems*. Hoboken, N.J: Wiley, 2007.
- [59] M. Renaud, P. Fiorini, R. van Schaijk, and C. van Hoof, “Harvesting energy from the motion of human limbs: The design and analysis of an impact-based piezoelectric generator,” *Smart Mater. Struct.*, vol. 18, no. 3, p. 035001, Jan. 2009. [Online]. Available: <https://doi.org/10.1088/0964-1726/18/3/035001>
- [60] J. M. Rodriguez-Fortun, J. Orus, J. Alfonso, F. Buil, and J. A. Castellanos, “Hysteresis in Piezoelectric Actuators: Modeling and Compensation,” *IFAC Proceedings Volumes*, vol. 44, no. 1, pp. 5237–5242, Jan. 2011. [Online]. Available: <http://www.sciencedirect.com/science/article/pii/S1474667016444381>
- [61] C. R. Saha, T. O'Donnell, N. Wang, and P. McCloskey, “Electromagnetic generator for harvesting energy from human motion,” *Sensors and Actuators A: Physical*, vol. 147, no. 1, pp. 248–253, Sep. 2008. [Online]. Available: <http://www.sciencedirect.com/science/article/pii/S0924424708001398>

- [62] M. Salauddin, M. A. Halim, and J. Y. Park, "A magnetic-spring-based, low-frequency-vibration energy harvester comprising a dual Halbach array," *Smart Mater. Struct.*, vol. 25, no. 9, p. 095017, 2016. [Online]. Available: <http://stacks.iop.org/0964-1726/25/i=9/a=095017>
- [63] C. M. Saravia, "On the electromechanical coupling in electromagnetic vibration energy harvesters," *Mechanical Systems and Signal Processing*, Jun. 2019. [Online]. Available: <http://www.sciencedirect.com/science/article/pii/S0888327019302006>
- [64] C. M. Saravia, J. M. Ramírez, and C. D. Gatti, "A hybrid numerical-analytical approach for modeling levitation based vibration energy harvesters," *Sensors and Actuators A: Physical*, vol. 257, pp. 20–29, Apr. 2017. [Online]. Available: <http://www.sciencedirect.com/science/article/pii/S0924424716306483>
- [65] J. Smilek, Z. Hadas, J. Vetiska, and S. Beeby, "Rolling mass energy harvester for very low frequency of input vibrations," *Mechanical Systems and Signal Processing*, vol. 125, pp. 215–228, Jun. 2019. [Online]. Available: <http://www.sciencedirect.com/science/article/pii/S0888327018303194>
- [66] N. G. Stephen, "On energy harvesting from ambient vibration," *Journal of Sound and Vibration*, vol. 293, no. 1, pp. 409–425, May 2006. [Online]. Available: <http://www.sciencedirect.com/science/article/pii/S0022460X05006784>
- [67] N. Storey, "Electronics a systems approach." Harlow: Pearson, 2013, pp. 251–253.
- [68] S. Zhu, W.-a. Shen, and Y.-l. Xu, "Linear electromagnetic devices for vibration damping and energy harvesting: Modeling and testing," *Engineering Structures*, vol. 34, pp. 198–212, Jan. 2012. [Online]. Available: <http://www.sciencedirect.com/science/article/pii/S0141029611003944>